Doctoral Dissertation

Study on Semiconductor Lasers of Circular Structures Fabricated by EB Lithography

（電子ビーム描画作製による円形構造半導体レーザに関する研究）

Ashim Kumar Saha

June 2015

Graduate School of Engineering,
Osaka University

Abstract

This dissertation addressed the design, fabrication and characterization of semiconductor lasers having circular geometry. The electron beam (EB) writing system with special pattern generator (SPG), designed for writing arbitrarily curved lines was used to define the circular geometries of the lasers.

Chapter 2 reported the design, fabrication and characterization of circular-grating-coupled surface emitting lasers (CGCSELs) with focusing function. Circular distributed Bragg reflector (DBR) and circular grating coupler (GC) were designed by using the coupled mode theory. Third order DBR was employed for its easier fabrication. DBR was designed for Bragg wavelength of 980 nm close to the gain peak of InGaAs quantum-well was. Distance of the grating surface from the QW active layer, groove depth and duty ratio of the DBR grating were optimized to obtain a large coupling coefficient with minimized total radiation decay factor. First-order chirped GC was designed for focusing the emitted light at a distance of 3.0 mm above the laser surface. Circular gratings were fabricated by EB lithography employing smooth circular scanning of e-beam and two step reactive ion etching (RIE). Single mode lasing was accomplished under pulse operation. Focusing of the surface emitted light was confirmed from the emission patterns.

Chapter 3 discussed the theoretical analysis and design considerations of a novel and simple all-active circular ring / Fabry-Perot (RFP) composite cavity laser. The lasing condition was derived by equating the complex round trip gain between the facet mirrors of the RFP laser to unity. Considering the mode frequencies of the ring and FP cavities, it was shown that the RFP laser can realize quasi single mode lasing with a side-mode suppression ratio (SMSR) higher than that of an ordinary FP laser. It was also discussed that two-wavelength lasing with nearly equal output powers can be accomplished in a RFP laser by controlling the currents injection to the ring and FP sections independently. Design parameters of the RFP laser were estimated by effective index method, finite element method (FEM), and beam propagation method (BPM) simulation.

Chapter 4 reported the fabrication and characterization of a simple all-active RFP composite cavity semiconductor laser. The laser having a ring radius of 400 μm

and an FP cavity length of 950 μm was fabricated using a GaAsP tensile strained single-quantum-well (SQW) in a separate confinement heterostructure (SCH). The RFP laser was fabricated by EB lithography and RIE processes. Lasing was accomplished under continuous wave (CW) operation. Threshold current was 140 mA and an output power of 12 mW was obtained at an injection current of 250 mA. Stable single-longitudinal-mode operation with an SMSR higher than 25 dB was achieved. The shift of the lasing wavelength was explained by considering the temperature coefficient of the bandgap energy of the QW.

Chapter 5 reported the fabrication and demonstration of two-wavelength lasing of a RFP laser fabricated with two electrodes. Two separate p-electrodes were used to control the injection currents to the ring and straight sections independently. The ring radius and the FP cavity length were 395 μm and 1090 μm, respectively. Currents were injected into the ring and straight waveguide sections by using two probes and two independent current sources. Two-wavelength lasing of almost equal power with 3.3~7.5 mW total output power under CW operation was accomplished by keeping the current injected into the FP section at a constant value and fine controlling the current injected into the ring section. Discrete sets of wavelength separations in 1.0~4.3 nm in the 800 nm band were obtained.

For the first time, I fabricated the stitching error free CGCSELs by using the unique technique of EB writing with circular scanning of e-beam. This unique fabrication technique would further accelerate the research on this type of lasers. Single mode lasing of a novel RFP composite cavity laser was accomplished under CW operation at room temperature. Simple fabrication process is one of the key advantages of this laser. I also demonstrated the two-wavelength lasing with almost equal powers from a single RFP laser for the first time. This laser could be promising candidate as a source for THz wave generation by photomixing process.

Table of Contents

Chapter 1

Introduction

1.1 Background

Since the first demonstration of semiconductor laser in 1962 [1], in present days it becomes an integral part of our lives. Laser diodes are used in optical communications, optical memories, laser printers, bar-code readers, measurement technology, medicine, industrial manufacturing and entertainment. In communications they supply the light that propagates in the fiber optical networks that have made the information technology revolution possible. Lasers are probably the only viable solution to the problem of connecting tomorrows high-speed computer boards together via optical interconnects. In medicine they help to diagnose and treat disease, analyze biological samples with high precision and low damage to tissue. In fabrication, lasers cut everything from fabrics to metals and measure various things. In entertainment, lasers supply the light that reads and writes the information on the discs that distribute movies, music, games and more (DVDs, CDs, mini discs, and game discs). The examples are increasingly numerous and ever in new and unexpected fields.

Semiconductor lasers of various geometric structures such as Fabry-Perot (FP), distributed feed-back (DFB), distributed Bragg reflector (DBR) and vertical cavity surface emitting lasers (VCSEL) are already commercially available for many

applications. Lasers of circular geometry received growing interest for their potential as very compact coherent light source [2], high power surface emission, beam shaping function, and monolithically integrated photonic circuits, many potential advantages for applications including laser display, printers, optical interconnects, sensing and THz wave generation.

Although the circular-grating structure is an unusual scheme for edge-emitting lasers, it has potential advantages for the realization of surface emitting lasers. The output beam emitting from a large circular aperture is an important feature which is not present in conventional straight-grating surface-emitting lasers. This feature can be used effectively in two-dimensional planar arrays. The output beam with a circular cross section also allows efficient coupling to the fiber. The idea of using curved-line grating as reflectors and resonators in integrated optics was first proposed by Tien [3]. Kerner *et al.* [4] were the first to investigate the coupling between the guided waves in a circular grating. The quality factor of circular grating resonators was discussed by Zheng and Lacroix [5] through development of coupled mode equations. Wu *et al.* [6], [7] developed a self-consistent coupled-wave theory for circular gratings and discussed the cross coupling between TE and TM waves. The analytical approach of Toda [8] potential for disk-shaped DFB lasers were brought to the attention of some of the research groups in different countries. Erdogan and Hall [9],[10] were the first to analyze the near-threshold behavior of a circularly symmetric first-order DFB laser. This theoretical work further stimulated the interest in these structures. Makino and Wu [11], [12] also reported the threshold gain and threshold current analysis of the first order circular grating DFB and DBR laser.

The first practical demonstration of an optically-pumped surface emitting DFB lasers with circular grating were presented by Wu *et al.* [13]. The 1.283μm double heterostructure GaInAsP/InP laser was tested under pulsed conditions at room temperature. Only a short time later, Erdogan *et al.* [14], [15] reported the observation of a 0.8175μm low divergence circularly symmetric surface emission from an AlGaAs/GaAs quantum well semiconductor laser. The laser was tested under pulsed conditions while mounted on a heat sink held at ~ 77 K. Wu *et al.* [16],

[17] succeeded in presenting the lasing characteristics of the first 1.3μm electrically pumped circular-grating surface-emitting DBR laser at room temperature under pulsed conditions. The reported threshold current and the output power were 170mA and 10mW respectively. High power and low threshold current electrically-pumped circular-grating surface emitting DBR laser was reported by Fallahi *et al.* [18]. The InGaAs/GaAs strained single-quantum-well laser was tested under pulsed conditions with a threshold current below 85mA and output power more than 20mW. They also reported the CW operation of circular-grating DBR laser with the current as low as 26mA at the operating wavelength 0.98μm [19]. A novel circular grating coupled surface emitting laser (CGCSEL) with integrated focusing outcoupler was reported by Kristjansson *et al.* [20]. They also investigated the effect of the errors in the near-field phases on the quality of the focused spot [21], [22]. In recent years, Li *et al.* [23], [24] reported about multimode behavior and static and dynamic modeling of the circular grating DFB laser. Sun *et al*, [25] presented a unified theory for the analysis of circular grating surface emitting DFB, disc type and ring type DBR laser. New applications such as THz radiation [26], [27] and optical switches [28] have also been demonstrated using circular grating structure.

The first circular ring laser was demonstrated by Matsumoto et al. [29] where the ring did not have an output coupler so only scattered emission was observed. After that, various cavity geometries were proposed and demonstrated, such as circular [30], [31], racetrack [32], [33] and triangular [34], [35] cavities. A y-junction output coupler was incorporated with ring shaped laser by Liao and Wang [36], [37]. Krauss *et al.* [30], [38]–[40] reported the comparison between the coupler configurations using y-junction, directional and multi-mode interference couplers. Hohimer *et al.* carried out an extensive research in the field of semiconductor ring laser and reported the single mode operation with high side mode suppression ration (SMSR) [31], [41], [42] effect of the feedback from the cleaved output mirrors on the operation and output power level [43]. Sorel *et al.* [44]–[46] measured and investigated several operating regimes of the ring lasers including bidirectional, alternate oscillations and unidirectionality. Moreover they established a model, which predicted the various operating regimes. Several applications of the SRL such

as ultra-fast all optical memory element [47], toggle flip-flop operation [48], and all optical regeneration[49], were reported in recent years. Multiple wavelength generation using monolithic integration of several semiconductor optical amplifiers (SOAs) and an arrayed waveguide grating (AWG) in a ring configuration [50], [51] also reported.

Single mode lasing of a Fabry-Perot (FP) laser coupled with two square shaped passive ring resonators by MMI couplers was reported [52]. Output power of 30 mW with an SMSR higher than 40 dB was obtained. The most exciting results were accomplished by Wu *et al.* [53]–[57] obtained from half wave coupled rectangular ring-FP lasers. Wavelength switching of 35 channels with 100 GHz spacing (wavelength ranges from 1549.4 nm to 1576.7 nm with SMSR up to 40.5 dB) [57] was demonstrated by changing the injection currents on the two cascaded rings synchronously.

1.2 Technological issues to the writing of circular gratings

An important and difficult part in the fabrication of CGCSEL is the formation of concentric circular gratings. Azimuthal variations in the duty ratio of the gratings in the CGCSEL resonator can strongly affect the reflection coefficient and consequently the lasing behavior [14]. This makes the electron beam (EB) lithography definitions of the gratings very important. The combination of small feature size (<100 nm) over large area (~500 μm) is very challenging, even for state-of-the-art EB lithography.

Several groups of researchers have published important contributions to the solution of this problem [14], [58]. A primary consideration in the problem of writing curved line structures by EB lithography is the question of how best to describe curved features with an X-Y (Cartesian) digital-to-analog converter (DAC) pattern generator. King *et al.* [58] tried to solve this problem by using a fractured polygon representation of curved line segments, as implemented on their JEOL

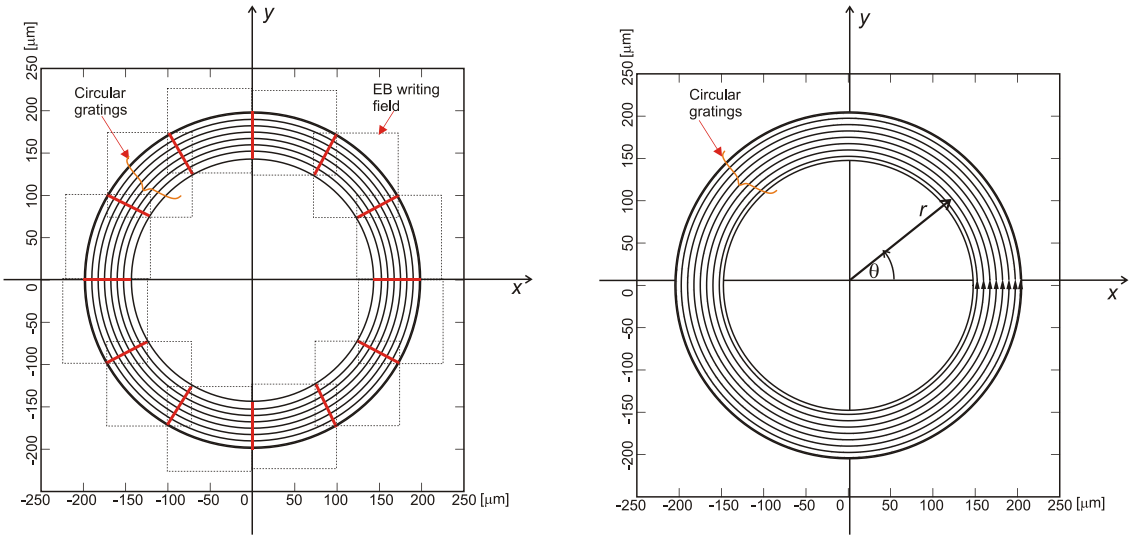

(a) (b)

Figure 1.1 (a) schematic representation of the extent of the writing fields (dotted lines) along with the sectors of the gratings (solid lines) that are written within each writing field. (b) Writing of entire grating patterns employing continuous circular scanning of e-beam in ELS-3700S EB machine.

machine. A best fit of rectangles and triangles were made to the ideal arc segment. This technique, however, leads to two unacceptable difficulties. The fabricated rings had scalloped edges and, hence, local variations in linewidth. On the other hand, very large amount of data generated using this scheme. The disk space required grows with the square of the number of rings generated, and easily becomes unwieldy.

Kristjansson *et al*. [20], [21], [59] defines the circular grating approximated by many small vertical and horizontal lines in a Cartesian reference frame. This means that the density of exposing points along a grating line varied with angle. Hence a complicated dose correction technique must be used to improve the uniformity of the grating linewidth. Another problem associated with the definition of the circular gratings by horizontal or vertical lines was that it required high resolution over a large area. This means that the gratings must be defined by using a high-resolution mode, which for their machine limits the size of each writing field to 80 μm × 80 μm. Hence, to define the entire gratings of a practical CGCSEL, it was necessary to

move the stage that holds the sample many times, as shown in figure 1.1(a). This introduces so called stitching errors. In their machine a laser interferometer was used to control the stage movement accurately, but no matter how carefully this was done there was always a certain degree of stitching errors. Because of the magnetic hysteresis of the beam deflection coil and the lack of scan rotation setting, the grating lines at the boundaries of two adjacent writing fields will never be matched exactly.

To eliminate the difficulties of circular grating fabrication, the electron beam (EB) writing system (Elionix ELS3700S) with special pattern generator (SPG), designed for writing arbitrarily curved lines was used. This curved-line scanning technique enabled the achievement of smooth writing of circular gratings as shown in figure 1.1(b), in comparison with conventional systems using scanning with an approximation of a circle by many short straight lines along X and Y directions and/or stage shift as shown in figure 1.1(a). Details of the circular patterns writing by smooth circular scanning of e-beam are discussed in the Appendix A.1. Since each of the grating circles was written by a single scanning of e-beam without stage shift, the stitching error problem was completely eliminated. This writing technique was also used to write the ring waveguide patterns of the RFP lasers.

1.3 Objective

The first objective is to realize the CGCSEL which can focus the surface emitted laser beam into a spot in the air. I designed the circular distributed Bragg reflector (DBR) and circular grating coupler (GC) by using coupled mode theory. Using the unique feature of the EB writing machine ELS-3700S installed in our laboratory as discussed above, circular gratings with uniform duty ratio can be fabricated. The grating patterns were written simply by continuous circular scanning of e-beam for avoiding stitching error problems. Stitching error free circular grating with uniform duty ratio would produce the azimuthally uniform lasing as well as better wavefront of the converging output laser beam.

The second objective is to design, fabricate and characterize a novel and simple all active circular ring/FP (RFP) composite cavity semiconductor laser. The entire waveguiding structure of this laser can be fabricated by a single etching step that simplifies the fabrication process. Realization of single mode or two wavelength lasing operation without using the complicated grating component and/or without regrowth processes would make this laser very attractive for many applications. I derived the lasing condition of the RFP laser by equating the complex round trip gain, product of the square of the complex transmittance and the reflectivities of the two facet mirrors, to unity. Analysis of the threshold gains of composite cavity mode, pure ring mode and pure FP mode are presented. Selection of composite lasing mode, possibilities of single mode and two-wavelength lasing operation are discussed using the mode frequencies of the ring and FP cavities. Stable single-longitudinal-mode lasing can be accomplished in a RFP laser fabricated with common p-electrode for current injection. Finally, I have fabricated an RFP laser with two separate p-electrodes for controlling the injection currents to the ring and FP sections independently. Two-wavelength lasing of almost equal power under continuous wave operation can be accomplished by keeping the current injection to FP section at a constant value and fine controlling the current injection to the ring section.

1.4 Organization of the thesis

This work dealt with the design, fabrication and characterization of semiconductor lasers having circular geometry. This thesis consists of six chapters and their layout is as follow:

In **chapter 2**, design, fabrication and performances evaluation of InGaAs quantum-well CGCSELs with focusing function are reported. Fabrication processes for obtaining smooth and uniform circular gratings are discussed. Lasing characteristics of the fabricated CGCSELs are measured. Focusing of the surface emitted light is confirmed from the emission patterns on different planes above the laser surface.

In **chapter 3**, working principle, lasing condition and design considerations of a novel RFP composite cavity laser are discussed. Details of the waveguide design, bend loss calculation and tangential coupler design are also presented.

In **chapter 4**, fabrication and demonstration of single mode lasing of a GaAsP RFP composite cavity semiconductor lasers are presented. Single mode lasing is accomplished with an SMSR higher than that of an ordinary FP laser under continuous wave (CW) operation. The shift of the lasing wavelength is explained by considering the temperature coefficient the bandgap energy of the QW.

In **chapter 5**, accomplishment of two-wavelength lasing of a GaAsP RFP laser is reported. Lasing of almost equal powers with total output 3.3~7.5 mW under CW operation are achieved.

In **chapter 6**, the conclusions of this thesis together with a few directions for possible future works related to CGCSEL and RFP composite cavity lasers are presented.

Chapter 2

Circular Grating Coupled Surface Emitting Lasers

2.1 Introduction

Circular-grating-coupled surface emitting lasers (CGCSELs) have many potential advantages for applications, such as laser displays, printers and optical interconnects. Single mode operation [60], output beam with circular symmetry [59], 2-D array formation [61], and beam shaping functions [20]–[22] have already been reported. Possibility of multispot generation by introducing phase shift modulation in the grating coupler [62], [63] would make this device an attractive candidate for many applications. An important and difficult part in the fabrication of CGCSELs is the formation of concentric circular gratings. Most of the earlier CGCSELs used a second-order distributed Bragg reflector (DBR) grating as an element for feedback and out-coupling [18], [59], [60]. In this configuration, the reflectivity for feedback and out-coupling efficiency cannot be optimized separately. CGCSELs having monolithically integrated chirped grating coupler (GC) for out-coupling the guided light and focusing into a spot in air were reported [20]–[22]. The circular gratings were fabricated by repeating electron-beam (EB) writing of many small segments,

and therefore the device involved the problems of wavefront distortions caused by the stitching errors.

This chapter presents the design, fabrication and performances evaluation of an InGaAs quantum-well CGCSEL. Circular distributed Bragg reflector (DBR) and circular grating coupler (GC) are designed by using coupled mode theory. Fabrication processes for obtaining smooth and uniform circular gratings are discussed. Lasing characteristics of the fabricated CGCSEL are measured. Focusing of the surface emitted light is confirmed from the emission patterns on different planes above the laser surface.

2.2 Device design

Schematic diagram of the CGCSEL structure is shown in figure. 2.1. The laser contains two concentric circular gratings surrounding a circular active region. The inner grating is a DBR to provide optical feedback for lasing and the outer grating is

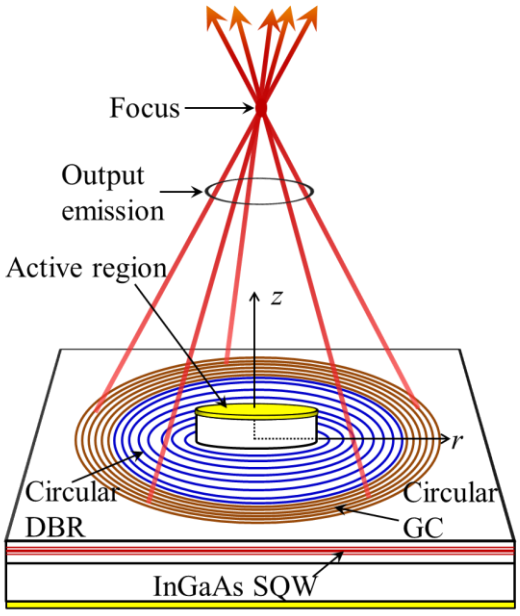

Figure 2.1 Schematic diagram of the CGCSEL with a DBR grating and a focusing grating coupler.

Table 2.1 Material, thickness, and the refractive index of each of the layers of the epitaxial structure used for designing the CGCSEL.

Layer	**Material**	**Thickness [nm]**	**Refractive index at 980nm**
Contact layer	GaAs	200	3.523
Upper buffer layer	$Al_{0.55}Ga_{0.45}As \rightarrow Al_{0.05}Ga_{0.95}As$	50	GRIN
Upper cladding layer	$Al_{0.55}Ga_{0.45}As$	1200	3.189
Upper GRIN layer	$Al_{0.25}Ga_{0.75}As \rightarrow Al_{0.55}Ga_{0.45}As$	150	GRIN
Upper barrier layer	GaAs	10	3.523
Quantum well layer	$Ga_{0.84}In_{0.16}As$	7	3.629
Lower barrier layer	GaAs	10	3.523
Lower GRIN layer	$Al_{0.55}Ga_{0.45}As \rightarrow Al_{0.25}Ga_{0.75}As$	150	GRIN
Lower cladding layer	$Al_{0.55}Ga_{0.45}As$	1200	3.189
Lower buffer layer	$Al_{0.05}Ga_{0.95}As \rightarrow Al_{0.55}Ga_{0.45}As$	50	GRIN
Substrate	GaAs		3.523

a chirped GC which acts as an out-coupling element with focusing function. This configuration is advantageous because the DBR and GC can be optimized independently. When current is injected to the central circular active region, light amplification takes place. The guided waves propagating radially outward couple with inward propagating waves in the DBR grating, and as a result laser oscillation starts. In the GC region, the outward propagating wave transmitted through the DBR is coupled out to the wave converging into a focus in air. The epitaxial structure used to design and fabricate the CGCSEL is a single-quantum-well (SQW) in graded refractive index (GRIN) separate confinement heterostructure (SCH). Details of the

epitaxial structure including the material compositions, layer thicknesses and the refractive indices are shown in the table 2.1. The InGaAs/GaAs quantum-well structure is compressively strained so that the gain for TE mode is larger than that of TM mode. Therefore, the oscillation in TE modes is expected. It is known that, for CGCSELs having circular symmetry, the lasing mode may be expressed as $TE_{\phi m}$ mode [59] with polarization parallel to the azimuthal direction and the electric field amplitude of $\cos(m\phi)$ azimuthal dependence.

2.2.1 Diffraction of light by waveguide gratings

Surface relief gratings are employed in this work. The exact position of the grating plane will be determined later but usually the gratings are fabricated in the cladding layer. Figure 2.2 (a) shows schematically the cross section of a typical waveguide grating structure. Λ is the period of the grating. The grating structure is represented by a grating vector $\boldsymbol{K}$ ($|\boldsymbol{K}| = K = 2\pi/\Lambda$) having a magnitude of $2\pi/\Lambda$ and an orientation along the direction of the period. When an optical wave represented by a wave vector $\boldsymbol{\beta}$ propagates in this structure, spatial harmonic waves represented by wave vectors $\boldsymbol{\beta} - q\boldsymbol{K}$ (q=1, 2, …) are induced. If $\boldsymbol{\beta} - q\boldsymbol{K}$ equals a wave vector of an optical wave that can propagate in the medium, the incident wave couples with this

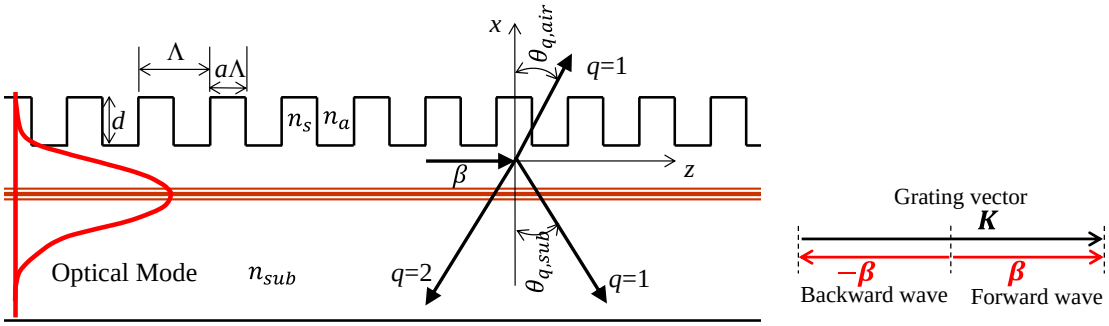

(a) (b)

Figure 2.2 (a) Schematic representations of a waveguide grating and its possible diffraction orders. (b) Wave vector diagram.

wave. This is the Bragg diffraction of q-th order. When

$$\boldsymbol{\beta} - q\boldsymbol{K} = -\boldsymbol{\beta} \tag{2.1}$$

holds, in particular, the incident wave of $\boldsymbol{\beta}$ couples with a backward wave of $-\boldsymbol{\beta}$. This is the Bragg reflection. For guided waves in a waveguide, the magnitude of the wave vector is given by $|\boldsymbol{\beta}| = \beta = 2\pi N_{eff}/\lambda$, where λ is the wavelength and N_{eff} is the effective refractive index. The wave vector diagram for $\boldsymbol{\beta}$ and $\boldsymbol{K}$ is shown in figure 2.2(b), and the Bragg condition given by Eq. (2.1) can be written as

$$\beta = \frac{qK}{2}. \tag{2.2}$$

The above relation, called the phase matching condition, indicates that only an optical wave with a wavelength $\lambda = 2\Lambda N_{eff}/q$ is effectively reflected. Effective reflection for a wave at wavelength λ can be attained by using a grating period

$$\Lambda = q\frac{\lambda}{2N_{eff}}. \tag{2.3}$$

When the grating period satisfies a certain condition (if $\boldsymbol{\beta} - \boldsymbol{qK}$ equals to the z-component of the wave vector of radiation mode into air and/or substrate), coupling between the guided mode and radiation mode may takes place. The angles of the diffracted light relative to the surface normal ($\theta_{q,air}$ and $\theta_{q,sub}$) for q-th order diffraction are determined by [64]

$$\sin\theta_{q,air} = \frac{1}{n_a}\left(N_{eff} - q\frac{\lambda}{\Lambda}\right), \tag{2.4}$$

$$\sin\theta_{q,sub} = \frac{1}{n_{sub}}\left(N_{eff} - q\frac{\lambda}{\Lambda}\right), \tag{2.5}$$

where n_{sub} and n_a are the refractive indices of the substrate and air, respectively. The wave vector diagrams of four different types of gratings showing the grating

vector, the wave vectors of the forward, backward and diffracted waves are illustrated in figure. 2.3.

It can be seen that, for example, if $q = 1$ (first order grating), then $\beta = K/2$. This will provide feedback without any diffraction into the substrate or into air, since for a first order grating the feedback is provided by the first order diffraction and there is no second order diffraction as shown in figure 2.3(a). For a second order grating the feedback is provided by the second order diffraction and there is first order diffraction normal into air and substrate as shown in the figure 2.3(b). A

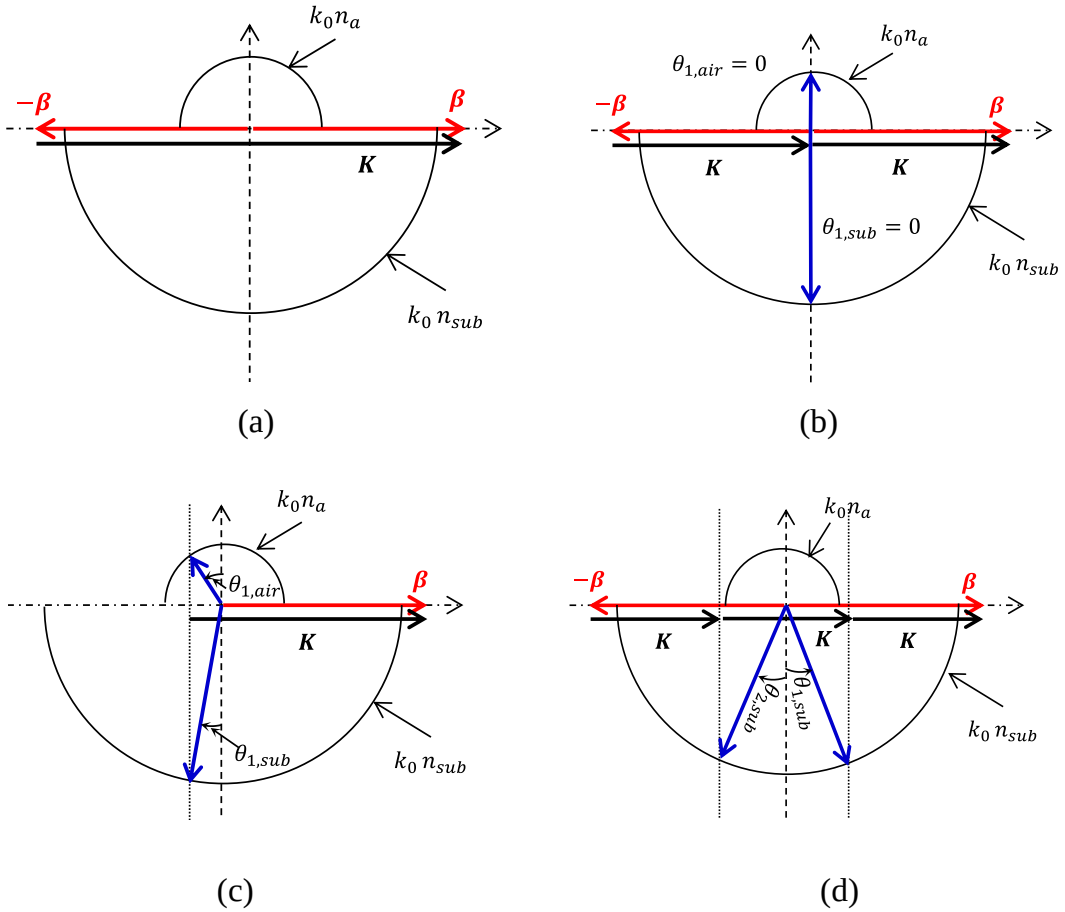

Figure 2.3 Wave vector diagrams for different types of gratings. (a) First order grating, (b) second order grating, (c) negatively detuned second order grating or first order grating coupler and (d) third order grating. $k_0 = 2\pi/\lambda$ is the propagation constant in the free space.

second order grating is therefore both a feedback and out-coupling element. A negatively detuned second order grating has a Λ that is less than the wavelength of the light in the waveguide. Here, second order diffraction is suppressed and first order diffraction radiates off-normal into air and substrate as shown in the figure 2.3(c). Such grating is therefore a pure out-coupling element. In the case of a positively detuned second order grating (Λ that is larger than the wavelength in the waveguide), the first order diffraction has angles on the other side of the surface normal compared to the case shown in figure 2.3(c), but increased detuning in this case will bring on second order diffraction into the substrate and make such an out-coupler inefficient. As q increases to 3, the feedback is provided by the third-order diffraction and lower orders will radiate at different angles into the substrate and into air as shown in figure 2.3(d).

2.2.2 Distributed Bragg reflector design

A DBR is a structure where an index grating of a period corresponding to the Bragg condition is formed in a passive waveguide. DBRs are used in a laser resonator to provide the optical feedback necessary for laser oscillation. It is important to differentiate between a pure feedback element like a first order grating and a radiating feedback element like second-order or third-order gratings. In a higher order grating the radiated power is a loss of the guided mode power that has to be accounted during the design of the DBR. In this work separate grating structures were designed for feedback and out-coupling functions. Although the first order grating is the best choice for DBR design, it is difficult to fabricate the first order grating for its smaller grating period. Fabrication becomes more difficult for the realization of circular grating with uniform duty ratio. A third-order DBR was employed for easier fabrication. The period of the third-order DBR for Bragg wavelength λ of 980 nm close to the gain peak of InGaAs quantum-well was determined as $\Lambda = 3\lambda/2N_{eff} = 457.8$ nm using the effective index of TE_0 mode $N_{eff} = 3.211$. Position of the grating plane from the top contact layer h (ridge height),

groove depth *d*, and duty ratio *a* (ratio of the teeth width to the period) of the DBR grating need to be optimized to obtain large coupling coefficient and minimize the radiation loss. The coupled-mode theory [65] ,[66] describes the coupling between two counter-propagating modes in a waveguide. In a uniform waveguide, there is no coupling and the modes propagate independently of each other. However, in the waveguide with a periodic index variation there will be coupling and power from the incident wave will be transferred to the reflected wave assuming that the Eq. (2.3) is fulfilled. Rectangular cross-sectional shape of the grating is considered for the simplicity of calculation. The *x*-axis and *z*-axis directions are the thickness of the waveguide and the propagation directions, respectively, as shown in figure 2.2. From the coupled mode theory [65], [66], guided mode coupling coefficient κ_q for *q*–th order grating can be represented by the Eq. (2.6) as

$$\kappa_q = \frac{\omega\epsilon_0}{4}\int_{-\infty}^{+\infty} E_y(x)^* \Delta\epsilon_q(x) E_y(x) dx\,, \tag{2.6}$$

with

$$\Delta\epsilon_q(x) = \frac{1}{\Lambda}\int_0^{\Lambda} \Delta\epsilon(x)\exp(-jqKz)\,dz = (n_s^2 - n_a^2)\frac{\sin(qa\pi)}{q\pi}, \tag{2.7}$$

where $\Delta\epsilon_q(x)$ is the Fourier amplitude of the grating structure, Λ is the grating period, *K* is the magnitude of the grating vector, *q* is the grating order, *a* is the duty ratio, $n_s$is the refractive index of the semiconductor layer of the grating and n_a is the refractive index of air. Similarly, radiation loss coefficient α_m can be represented by Eq. (2.8) as

$$\alpha_m = \pi|\kappa_m|^2, \tag{2.8}$$

with

$$\kappa_m = \frac{\omega\epsilon_0}{4}\int_{-\infty}^{+\infty} E_m^*(x)(n_s^2 - n_a^2)\frac{\sin(ma\pi)}{m\pi}E_y(x)dx\ . \qquad (2.9)$$

Here, m=1, 2,…q-1 represents the diffraction order producing the radiation into air and/or substrate, $E_y(x)$ is the normalized electric field distribution of the fundamental guided mode and $E_m(x)$ is the normalized electric field distribution of

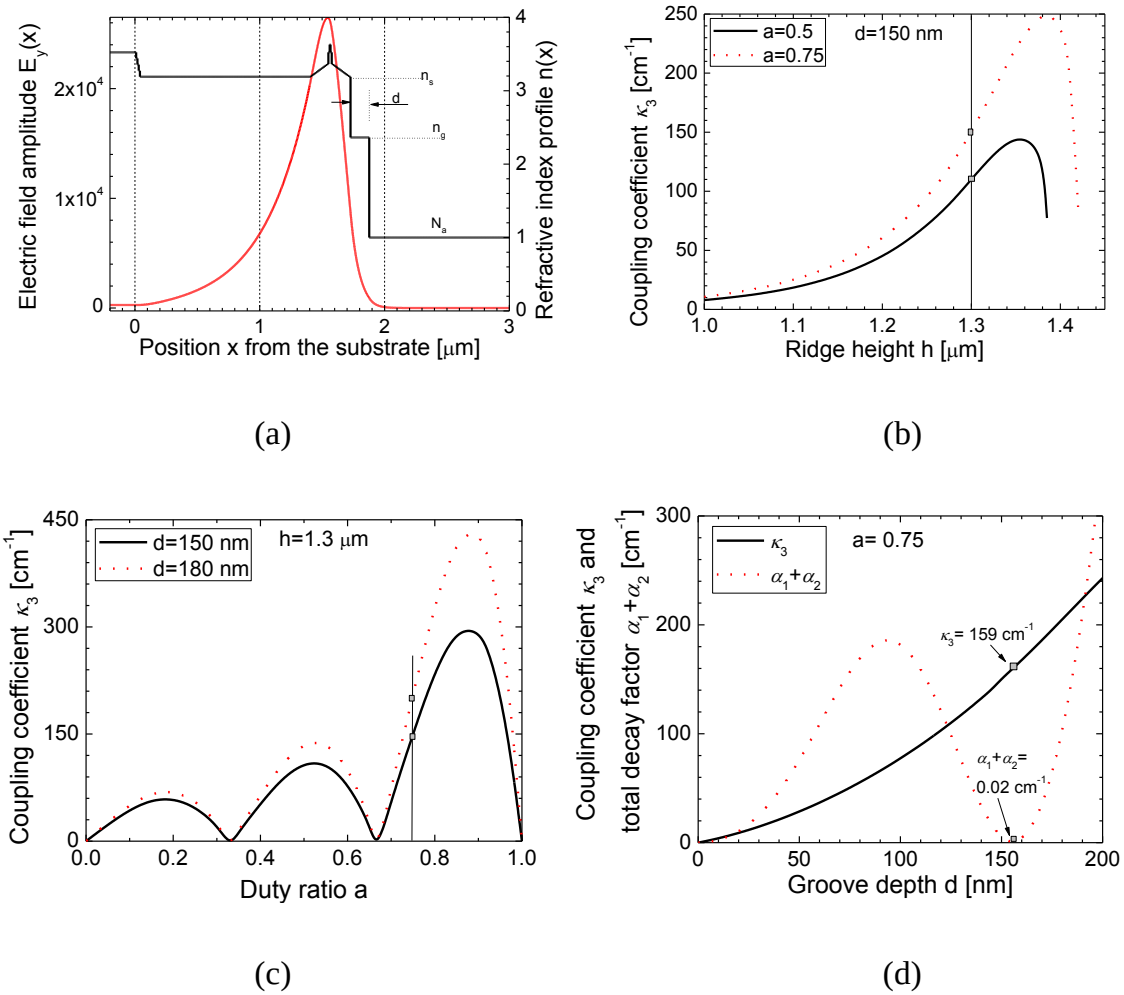

Figure 2.4 (a) Plot of the normalized guided mode profile $E_y(x)$ at the grating region and the refractive index profile. (b) Dependences of κ_3 on the ridge height h calculated for a=0.5 and 0.75. (c) Dependences of κ_3 on the duty ratio a calculated for a=150 and 180 nm. (d) Dependences of κ_3 and $\alpha_1 + \alpha_2$ on the groove depth d.

the radiation mode produced by *m*-th order diffraction. Figure 2.4 (a) shows the amplitude of the $E_y(x)$ in the grating region calculated using the transfer matrix method [115]. Refractive index of the grating layer n_g was approximated as $n_g^2 = an_s^2 + (1-a)n_a^2$.

In the third order DBR grating (q=3), coupling between forward and backward propagating guided modes take place by the third order diffraction, whereas the first and second order diffractions (m=1 and m=2) couple the guided mode with the radiation modes into the substrate. For different values of ridge height h, groove depth d and duty ratio a, I calculated the third-order coupling coefficient κ_3, and factors α_1 and α_2 for radiation decay caused by first and second-order diffractions into the substrate, using the Eqs. (2.6)–(2.8). Figure 2.4(b) shows the dependences of κ_3 on h calculated for two different values of a. The coupling coefficient increases with the increase of h. For h>1.35 μm, κ_3 decreases rapidly so that the value of ridge height was determined as h=1.3 μm. Figure 2.4(c) shows the dependences of κ_3 on a calculated for two different values of d. Although the maximum coupling coefficient can be obtained for a≈0.9; however, the fabrication of circular grating with such a high duty ratio is rather difficult. Considering this in mind, a=0.75 has been selected. Using the values of a=0.75 and h=1.3 μm, the calculated dependences of coupling coefficient κ_3 and total decay factor $\alpha_1+\alpha_2$ on d were shown in the figure 2.4(d). It was found that at d = 155 nm, κ_3 of 159 cm^{-1} can be obtained with minimized $\alpha_1+\alpha_2$ of 0.02 cm^{-1}.

Power reflectivity R and power transmissivity T of a DBR can be calculated by the Eqs. (2.10) and (2.11) as [66]

$$R = \frac{|\kappa \sinh(j\gamma L_{DBR})|^2}{\left|\gamma\cosh(j\gamma L_{DBR}) - \left(j\frac{\alpha_{DBR}}{2} + \Delta\right)\sinh(j\gamma L_{DBR})\right|^2}, \tag{2.10}$$

$$T = \frac{|\gamma|^2}{\left|\gamma\cosh(j\gamma L_{DBR}) - \left(j\frac{\alpha_{DBR}}{2} + \Delta\right)\sinh(j\gamma L_{DBR})\right|^2}, \tag{2.11}$$

$$\begin{cases} \gamma = j\sqrt{\left(\frac{\alpha_{DBR}}{2} - j\Delta\right)^2 + \kappa^2}, \\ 2\Delta = 2\beta - qK, \\ \alpha_{DBR} = \alpha_{abs} + \alpha_1 + \alpha_2. \end{cases} \tag{2.12}$$

Here, β is the propagation constant of the guided mode, K is the magnitude of the grating vector, L_{DBR} is the interaction length of the DBR, 2Δ represents the deviation from the Bragg condition, α_{DBR} is the passive loss factor of the DBR region, α_{abs} is the absorption loss coefficient, and α_1+α_2 is the total radiation loss coefficient. Assuming an absorption loss in the passive grating region α_{abs} = 40 cm^{-1} [67] with the calculated values of coupling coefficient κ_3 =159 cm^{-1} and total radiation loss coefficient α_1+α_2= 0.02 cm^{-1}, the calculated dependences of the reflectivity R and the transmissivity T of a third order DBR (q=3) on L_{DBR} at the Bragg wavelength ($\Delta = 0$) are shown in the figure 2.5. It is obvious that the higher the reflectivity is

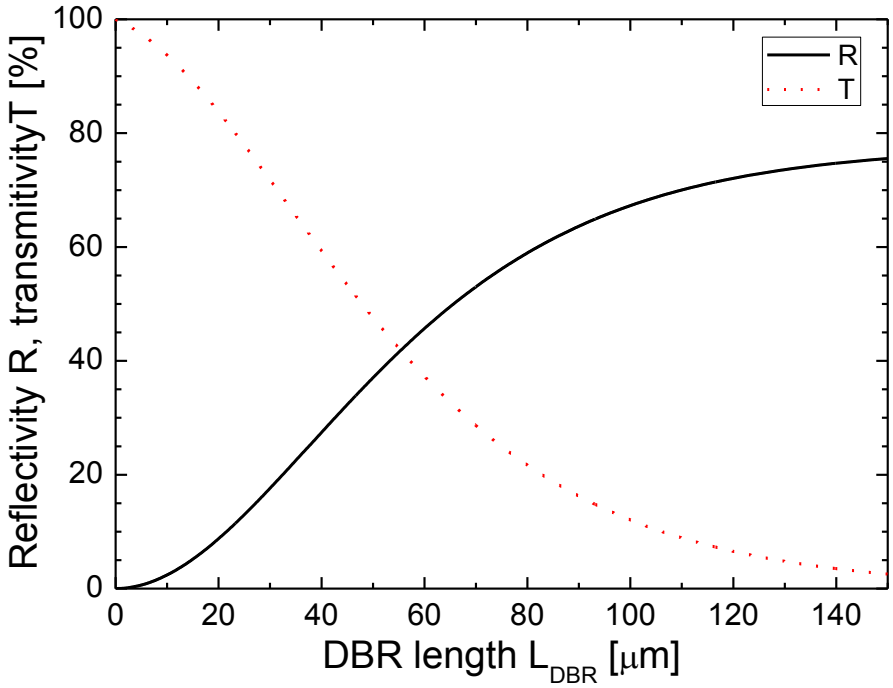

Figure 2.5 Dependence of R and T on the DBR length L_{DBR} at the Bragg wavelength.

the lower the lasing threshold will be. However, the output power will be reduced because of the reduced *T*. Hence the DBR length must be decided carefully depending on the requirement. Since the accomplishment of lasing of the CGCSEL is my first goal, I considered a DBR which will provde 50-60% power reflectivity. I have selected the DBR length as 80 μm so that calculated values were *R*=58% and *T*=21%.

2.2.3 Grating coupler design

In the grating coupler (GC), coupling between the guided mode and radiation modes takes place so that the power from waveguide radiates into the air and/or substrate. The GC used in the CGCSEL has two main functions. Firstly, it out-couples the laser light from the guided region and makes the laser surface emitting. Secondly, it helps to focus that surface emitted light at a single point above the laser plane. Schematic view of such a GC is shown in figure 2.6(a). To focus the surface emitted light at a distance *f* above the laser surface, the radial variation of grating period $\Lambda(r)$ of the GC can be derived from the wave vector diagram for the first-order diffracted wave into air as [65]

$$N_{eff}k_0 + n_a k_0 \sin\theta(r) = K(r),$$

$$N_{eff}\frac{2\pi}{\lambda} + \frac{2\pi}{\lambda}\sin\theta(r) = \frac{2\pi}{\Lambda(r)},$$

$$\Lambda(r) = \frac{\lambda}{\sin\theta(r) + N_{eff}},$$

$$\Lambda(r) = \frac{\lambda}{\frac{r}{\sqrt{r^2 + f^2}} + N_{eff}}. \qquad (2.13)$$

For a CGCSEL having an active region diameter of 240 μm and L_{DBR} = 80 μm, the GC length was selected as L_{GC} = 45 μm to fit the total device size within the EB

writing field size of 500 μm × 500 μm. For focusing the emitted laser light at f = 3.0 mm, the periods of the chirped GC were calculated by using the Eq. (2.13). The period varies from 299.3 nm for r = 200 μm to 297.9 nm for r = 245 μm.

The wave vector diagram of the first order GC is shown in the figure 2.6(b). First order diffraction in the designed GC produces the air and substrate radiation modes. Propagation vectors of the air and substrate radiation modes are k_{air} and k_{sub}, respectively. The radiation decay factors α_{air} (into air) and α_{sub} (into substrate) can be calculated by using the Eq. (2.8) with m=1. For the calculation of α_{air}, the coupling coefficient between air-mode and guided-mode was used. Similarly, to calculate α_{air}, the coupling coefficient between substrate-mode and guided-mode was used. α_{air} and α_{sub} are the most important fundamental parameters to describe the characteristics of a GC because the power distribution ratio into air is P_{air} =

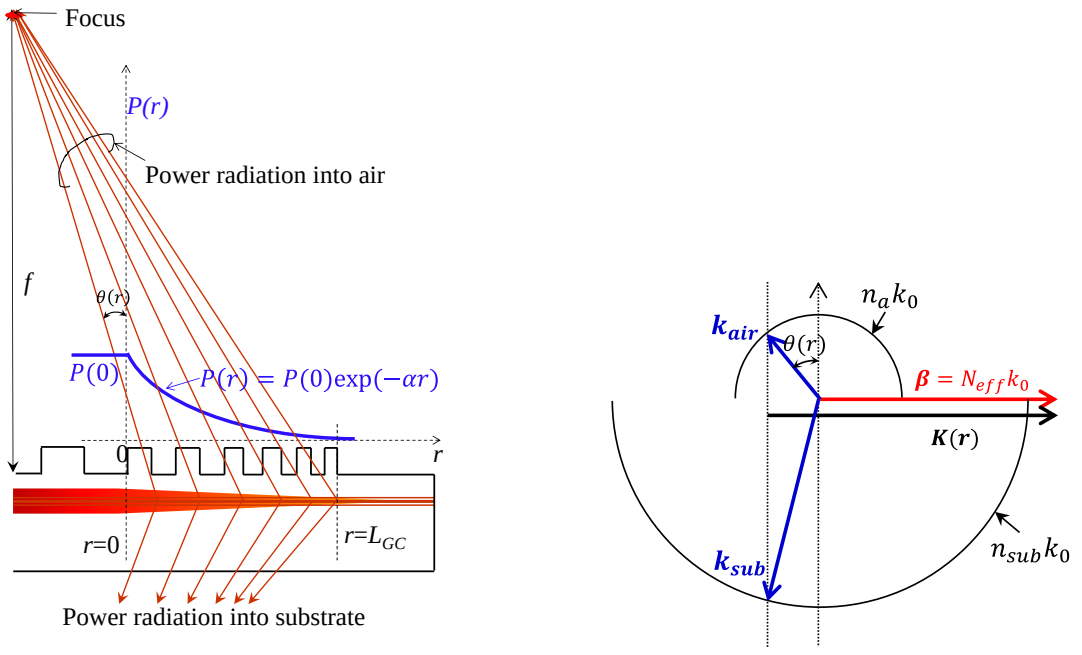

(a) (b)

Figure 2.6 (a) Schematic of the focusing grating coupler used in the CGCSEL. (b) Wave vector diagram of the GC showing the first-order diffracted wave into air and substrate. $\theta(r)$ is the exit angle of the emitted light from the grating coupler.

$\alpha_{air}/(\alpha_{air}+\alpha_{sub}+\alpha_{abs})$. This means that α_{air} higher than α_{sub} gives higher power output than the power radiates into substrate. Coupling efficiency into air η_{air} of the GC can be calculated by using [68]

$$\eta_{air} = P_{air}[1 - \exp\{-(\alpha_{air} + \alpha_{sub} + \alpha_{abs})L_{GC}\}]. \quad (2.14)$$

Values of α_{air} and α_{sub} are calculated by using the Eq. (2.8) for different a with h=1.3

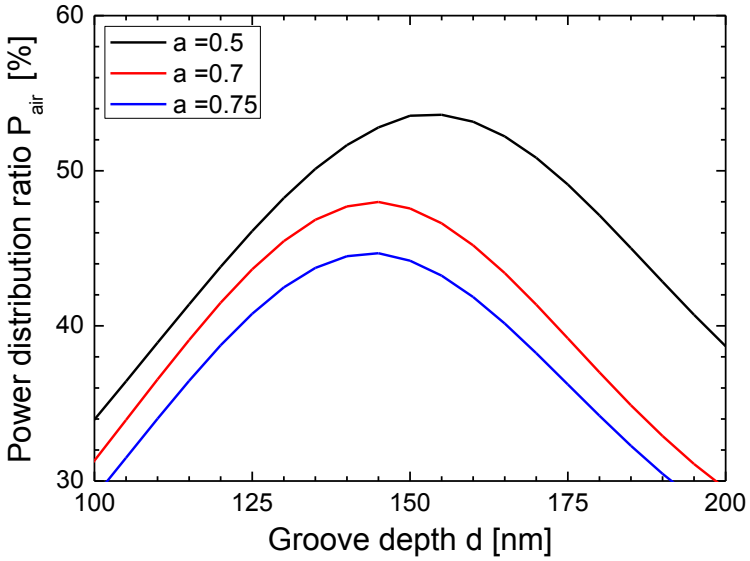

(a)

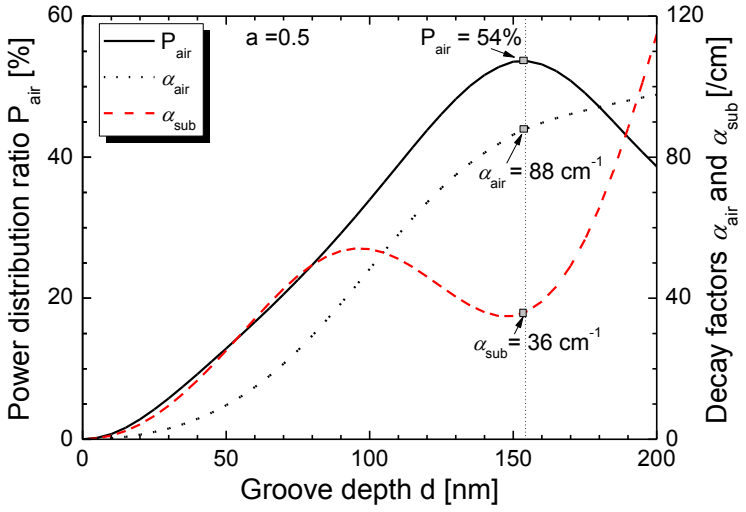

(b)

Figure 2.7 (a) Dependence of P_{air} on groove depth d for three different values of a. (b) Dependence of P_{air}, α_{air} and α_{sub} on groove depth d calculated for a=0.5.

μm. Figure 2.7(a) shows the dependence of P_{air} on the groove depth d of GC calculated by assuming α_{abs} = 40 cm^{-1}. It can be seen that the maximum of P_{air} increases with the increase of a. The maximum of P_{air} can be obtained at d=143, 144 and 155 nm for a= 0.75, 0.7 and 0.5, respectively. Figure 2.7(b) shows the dependence of P_{air}, α_{air} and α_{sub} on the groove depth d calculated for a=0.5. It was found that the highest P_{air} of 54% can be obtained at d = 155 nm. At this value of d, α_{air} = 88 cm^{-1} and α_{sub} = 36 cm^{-1} were obtained. Using the Eq. (2.14) with L_{GC} = 45 μm, the coupling efficiency into air η_{air} of the GC was calculated as 28%.

2.3 Fabrication of CGCSEL

2.3.1 Overview of the fabrication process

The designed CGCSEL was fabricated by using an InGaAs single quantum-well graded index (GRIN) separate confinement heterostructure (SCH) epitaxial structure as listed in the table 2.1. Fabrication process can be divided into three parts such as: (1) Ridge structure formation at the active region, (2) circular DBR and GC fabrication and (3) p-side and n-side electrode formation. Details of these fabrication processes are explained in the following sections.

2.3.2 Formation of circular active region

Circular disk shaped structure for active regions were fabricated by EB lithography and reactive ion etching (RIE). Schematic representation of the fabrication steps are shown in figure 2.8 (a). At first, the ZEP-520A EB resist has been spin coated at 2500 rpm for 90 sec to get the resist thickness of about 0.5μm. The sample was baked at 200 ºC for 3 min for hardening of the resist. Then the patterns of the circular active regions were defined by EB lithography employing circular scanning mode with a writing field size of 500μm × 500μm. Details of the EB writing

conditions are given in the table 2.2(a). After finishing the EB writing, sample was developed by ZED-N50. For the formation of circular disk of 1.3 μm height, some hard mask must be used to etch the semiconductor materials and in this case SrF_2 has been chosen. SrF_2 masks of 250 nm thicknesses were formed by vacuum evaporation and lift-off process. Figure 2.8(b) shows the optical microscopic images of the SrF_2 hard masks. The contact and upper cladding layers outside the circular active region were removed by reactive ion etching (RIE) using CH_4/H_2 and CF_4/H_2 gases alternatively. CF_4/H_2 gas was used to reduce the amount of contaminated

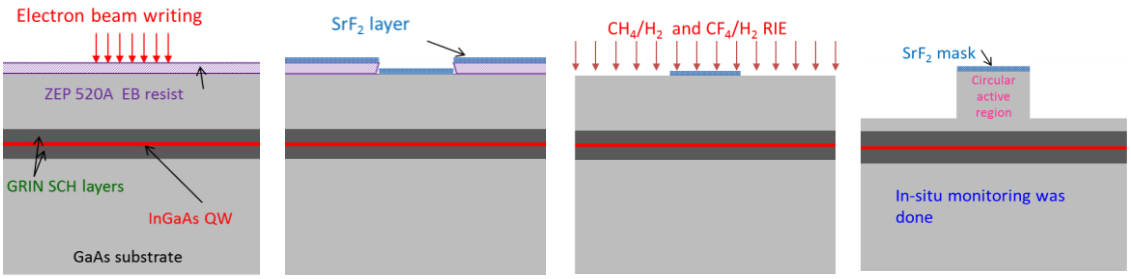

(a)

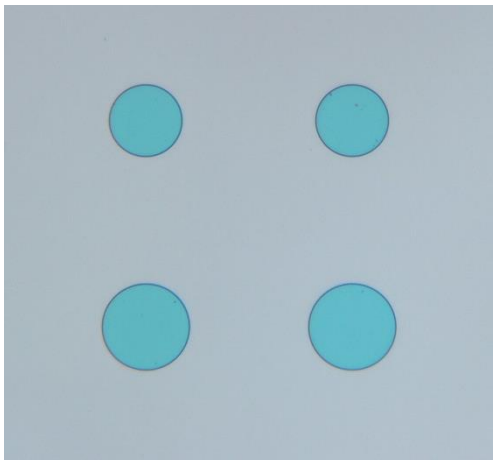

(b)

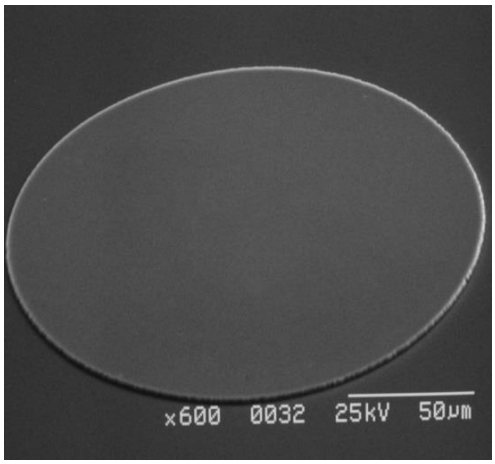

(c)

Figure 2.8 (a) Schematic of the circular active region formation. (b) Optical microscopic image of the SrF_2 masks. (c) SEM image of the disk like active region formed by RIE.

polymer deposited on the top of the SrF_2 mask during the RIE process using CH_4/H_2 gas. The RIE conditions and time are listed in table 2.2 (b) and (c). In-situ monitoring was done by using a laser probe for accurate control of the etching depth. After finishing the RIE, remaining polymer was removed by O_2 plasma ashing. Finally, the SrF_2 masks were removed from the top of the active region by immersing the sample into 5% HCl. Figure 2.8(c) shows an SEM image of the disk like active region formed by RIE.

Table 2.2 Various conditions for ridge structure formation process.

(a) EB drawing of active region pattern.

Resist	ZEP520A-11cp
Spin-coating conditions	2500 rpm, 90 sec
Acceleration voltage	30 kV
Magnification	200
Beam current	0.3 nA
e-beam scanning speed	100×0.05μs/dot
Scanning unit	SPG mode

(b) RIE conditions during ridge structure formation.

Type of gas	CH_4/H_2	CF_4/H_2
Mixing ratio	1:10	9:1
Flow	20 sccm	7 sccm
Gas pressure	0.03 Torr	
RF power	50 W	

(c) Required time of RIE using CH_4/H_2 and CF_4/H_2 gases alternately.

Gas	Time (min)														
CH_4/H_2	30		15		15		15		15		15		15		18
CF_4/H_2		2		1.5		2		1.5		2		1.5		2	

2.3.3 Circular DBR and GC fabrication

Circular DBR and grating coupler for CGCSEL have been fabricated by using EB writing and two-step RIE with SiO_2 mask layer. Schematic representation of the step by step fabrication process of DBR and grating coupler are shown in figure 2.9 (a). Since the grating pattern on the EB resist ZEP 520A changes during RIE due to the reaction with H_2, ZEP520A cannot be used as a mask for the formation of grating structure with fine grooves by RIE using CH_4/H_2. So that a thin SiO_2 hard mask layer has been used as an intermediate layer between the semiconductor and the EB resist layer.

To fabricate the circular DBR and GC, at first a 15 nm thick SiO_2 layer was deposited by plasma-enhanced chemical vapor deposition (PECVD) process. In-situ monitoring was done for achieving the desired film thickness. SiO_2 deposition conditions are given in table 2.3.

The EB writing system (Elionix ELS3700S) with special pattern generator (SPG), designed for writing arbitrarily curved lines was used to write the grating patterns. Writing of circular pattern by using ELS3700S is described in the Appendix A.1. The SPG consists of two sets of data registers, 16-bit digital to analog converters (DACs) and address counters for X and Y scanning, and a presettable clock generator for assigning the scanning speed. The X and Y data for a circle of a diameter were prepared by the computer and sent to the registers, and

Table 2.3 Conditions of SiO_2 deposition by PECVD.

Type of gas	TEOS	O_2
Flow	2 sccm	200 sccm
Gas pressure	0.75 Torr	
Temperature	350 ºC	
RF power	100 W	
Deposition time	41 sec	

Table 2.4 Various conditions of the 2-step RIE process.

(a) CF_4/H_2 RIE for pattern transfer from resist to SiO_2.

Type of gas	CF_4/H_2 (9:1)
Flow	5 sccm
Gas pressure	0.03 Torr
RF power	50 W
Time	60 seconds

(b) Removal of resist using O_2 plasma ashing.

Type of gas	O_2
Flow	40 sccm
Gas pressure	0.2 Torr
RF power	20 W
Time	28 minutes

(c) CH_4/H_2 RIE for pattern transfer from SiO_2 to semiconductor.

Type of gas	CH_4/H_2 (1:5)
Flow	20 sccm
Gas pressure	0.03 Torr
RF power	50 W
Time	17 minutes

(d) Removal of polymer using O_2 plasma ashing.

Type of gas	O_2
Flow	40 sccm
Gas pressure	0.2 Torr
RF power	20 W
Time	90 minutes

(e) CF_4/H_2 RIE for removing SiO_2 layer.

Type of gas	CF_4/H_2 (9:1)
Flow	14 sccm
Gas pressure	0.1 Torr
RF power	50 W
Time	90 seconds

then constant-speed circular-line EB scanning was performed under control by the SPG. This sequence was repeated with increased diameters to write the entire DBR and GC patterns. This curved-line scanning system enabled achievement of smooth writing, in comparison with conventional systems using scanning with approximation of a circle by many short straight lines along X and Y direction and/or stage shift. The EB acceleration voltage was 30 kV, beam current was 40 pA and beam diameter (full width at half maximum) was 40 nm. The DBR and GC patterns were written with different scanning speeds to have the gratings with designed duty ratios. After development, the patterns were transferred from the resist

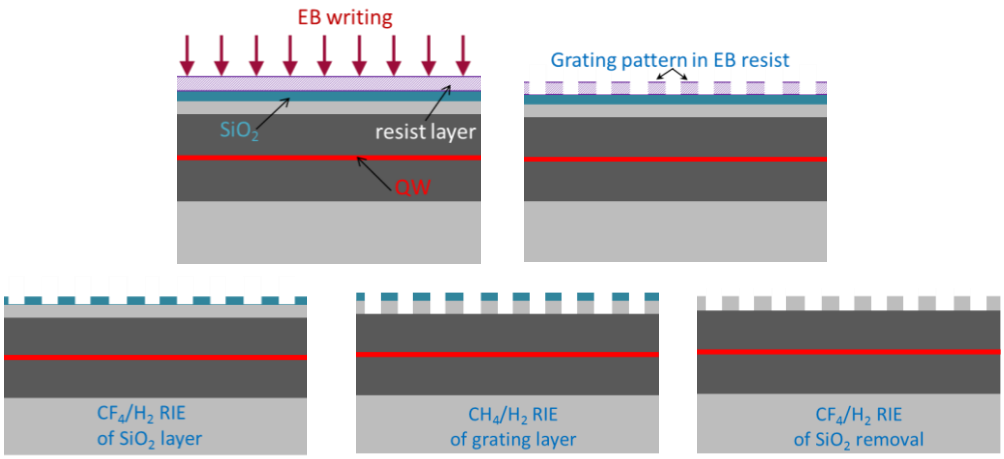

(a)

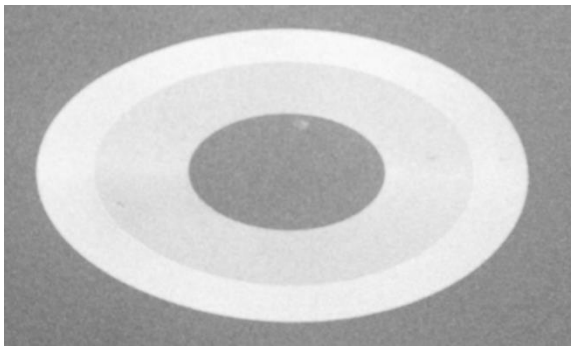

(b)

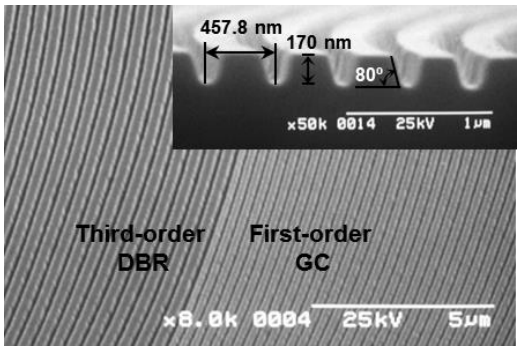

(c)

Figure 2.9 (a) Schematic of the DBR and GC fabrication process. SEM images of the (b) perspective view of the full circular gratings (c) part of the DBR and GC. Inset image shows the cross section of the DBR grating.

to the SiO_2 layer by RIE using CF_4-H_2 gas, and then transferred into the semiconductor layer by second RIE using CH_4-H_2 gas. Details of the grating fabrication by two-step RIE process are shown in the table 2.4.

An SEM micrograph of the fabricated device is shown in figure 2.9(b). As a result of circular scanning, stitching-error-free circular gratings were fabricated. Magnified view of the circular DBR and the chirped GC is shown in figure 2.9(c). The DBR and GC gratings of almost uniform duty ratios of a = 0.75 and 0.6, respectively, were obtained. Inset is the cross sectional view of the DBR. The groove depth d was approximately 170 nm, and the angle of the etched side wall was around 80º. Calculation showed that κ_3 and reflectivity of DBR with 80º side wall were ~1.2 times and ~1.1 times of those (κ_3 = 159 cm^{-1}, 58%) for vertical side wall. This deviation would not cause significant influence to the device performance.

2.3.4 Contact metallization

For depositing the p-side electrodes, 800 nm thick ZEP-520A resist masks were prepared by EB lithography. By using vacuum deposition technique and lift-off

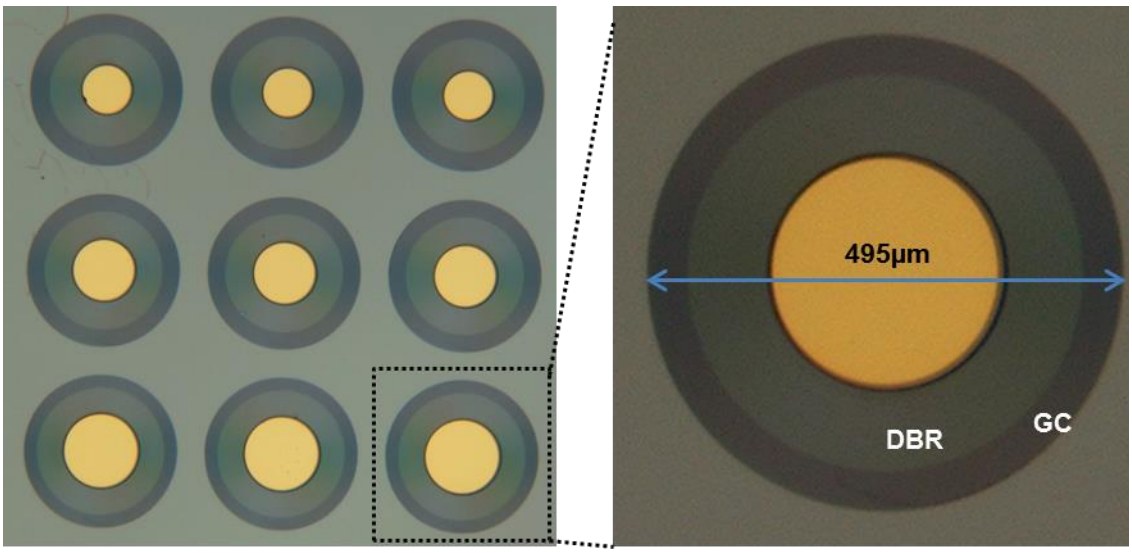

Figure 2.10 Optical microscopic images of a group of CGCSEL fabricated with different device parameters.

Table 2.5 List of device parameters of the CGCSELs.

Active diameter *D* [μm]	160, 200, 240
DBR length L_{DBR} [μm]	100, 90, 80
GC length L_{GC} [μm]	65, 58, 45
Ridge height *h* [μm]	1.3
Groove depth *d* [nm]	155
DBR periods Λ [nm] (12 different periods)	447.3 to 468.7
Focal length *f* [mm]	3.0

process, 300 nm thick Cr/Au pad electrodes were formed on the top of the active disk. After reducing the thickness of the substrate to 120 μm, AuGe/Au n-electrode was evaporated on the backside. Figure 2.10 show the optical microscopic images of a group of fabricated CGCSELs. I have fabricated several groups of CGCSELs with 3 different device parameters (*D*, L_{DBR} and L_{GC}) and 12 different DBR periods as listed in table 2.5. As a result of circular scanning, stitching-error-free circular gratings were fabricated. Finally, the CGCSELs were mounted with an AlN sub-mount on a Cu heat sink for experimental measurements.

2.4 Characterization

2.4.1 Experimental setup for optical measurement

The fabricated CGCSELs were tested under pulse operation. Figure 2.11 (a) shows the way of placing the current probe on the CGCSEL. Output laser light was detected by a fast response photodetector connected with an oscilloscope as shown in figure 2.11(b). Optical setup to collect the emitted laser light for measuring the output power is shown in figure 2.11(c).

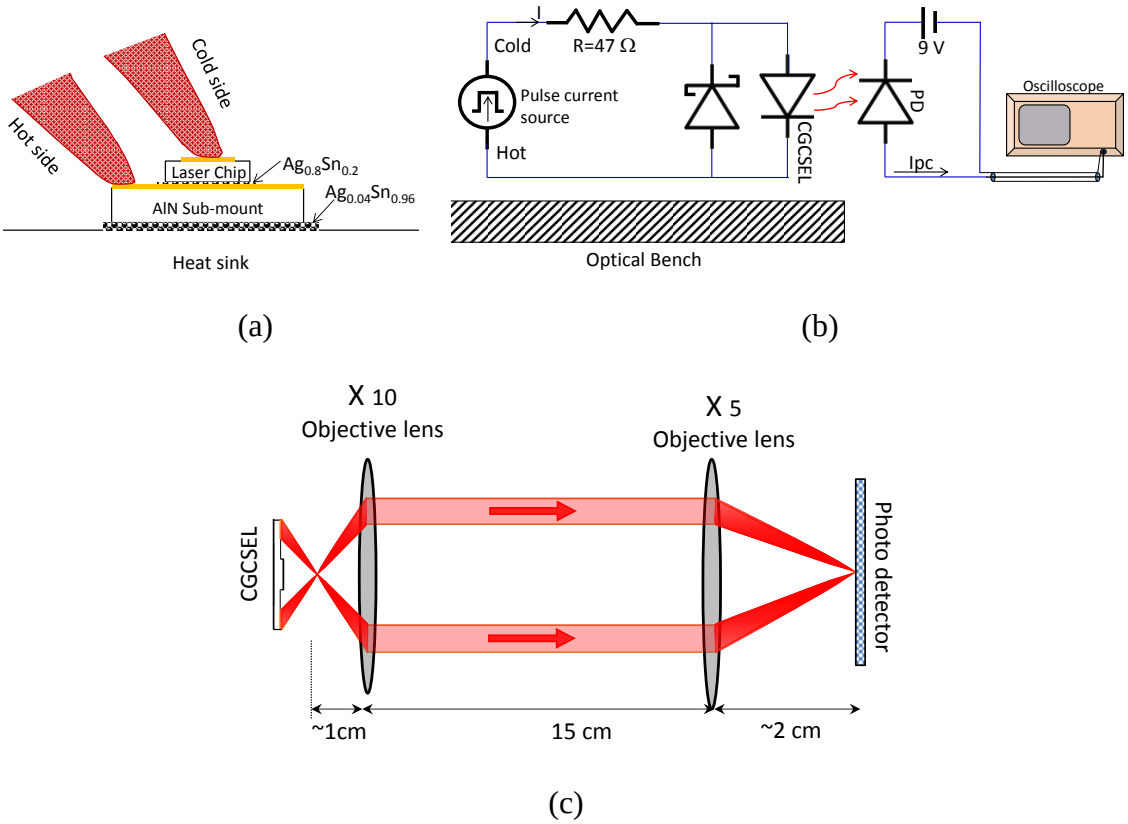

Figure 2.11 (a) The way of placing the current probe on the CGCSEL. (b) Connection diagram to derive the CGCSEL and output power measurement system. (c) Optical setup to collect the emitted light for power measurement.

2.4.2 P-I characteristics

The fabricated CGCSELs were tested under pulse driving with a current pulse of 100 μs width and 20 ms period. The peak output power was calculated from the photo detector response measured by the oscilloscope. Figure 2.12 shows the measured *P-I* characteristic of three different CGCSELs. Among them the best performance was obtained for the CGCSEL having an active region diameter of 240μm, DBR length of 80μm and GC length of 45μm as shown by the red curve in figure 2.12. Threshold current was around 80 mA (177 A/cm^2), and the peak power of the surface-emitted output beam was 275 μW at 150 mA. Nonlinearity in the P-I curve for current higher than 110 mA may be due to mode hopping. The reasons for the low output power would be the deviation of the DBR groove depth of the fabricated device from the designed value and the passive waveguide loss larger than the assumed value.

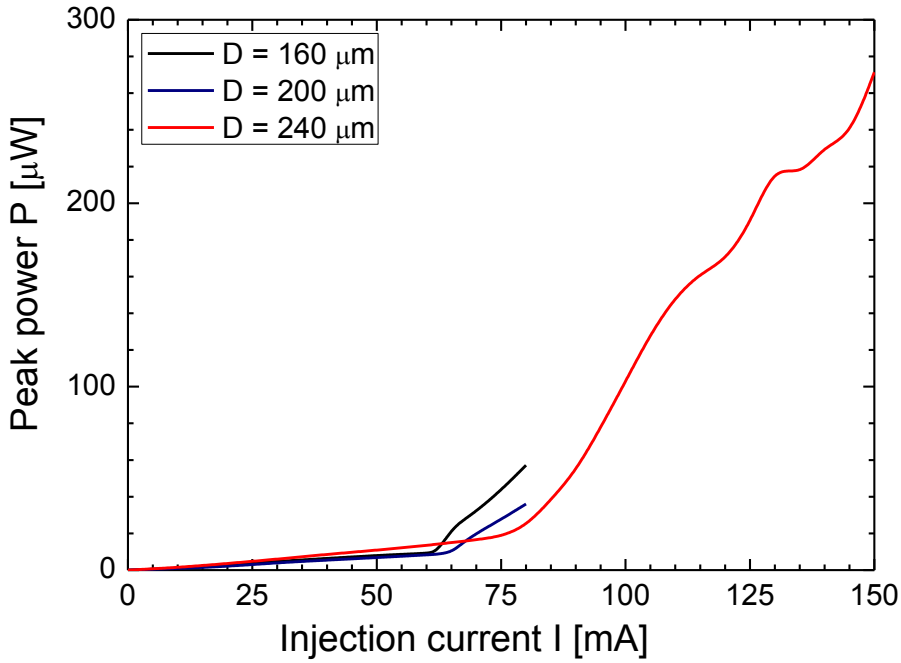

Figure 2.12 P-I characteristic of the CGCSELs measured under pulse deriving at 23ºC.

2.4.3 Lasing spectrum

Lasing spectrum was measured by using an optical spectrum analyzer (Anritsu MS9710B). Figure 2.13 shows the lasing spectra of a group of fabricated CGCSELs obtained at injection currents about 20mA above the threshold currents of the corresponding lasers under pulse operation. The DBR grating periods Λ of each of the lasers are also indicated in the figure. All of the lasers show the single mode lasing, however the lasing peak wavelengths were approximately 2.5 nm higher than the designed Bragg wavelengths. These deviations were due to the difference between theoretically estimated effective refractive indices and their actual values.

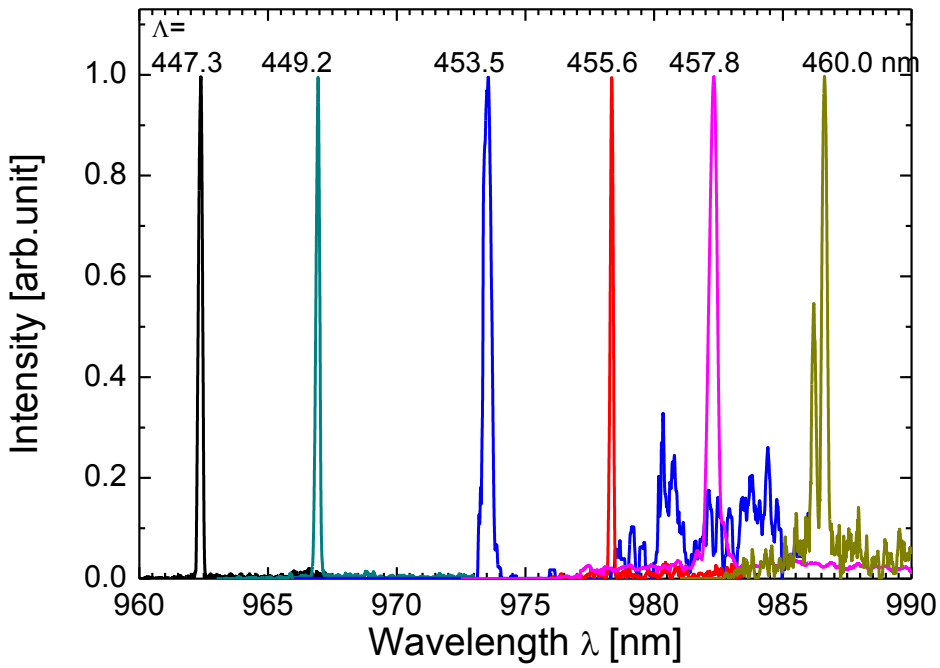

Figure 2.13 Lasing spectra of a group of CGCSELs. Periods Λ of the DBR grating of each of the lasers are shown at their corresponding spectrum.

2.4.4 Focusing function

Focusing of the surface emitted laser beam of the CGCSEL having an active region diameter of 240μm, DBR length of 80μm and GC length of 45μm was confirmed by measuring the emission patterns at different distances from the laser surface. Figure 2.14(a) shows the images of emission patterns at an injection current of 140 mA. The dark region on the upper side in the near-field pattern (z=0) is the shadow of the current injection probe. Bright ring-like shape observed around the circular active region is the scattered light from the side wall of the circular mesa. The brightest region in the outer part of the CGCSEL is the coherent light emitted from the GC and converging towards the focal plane. The near-field pattern was not azimuthally uniform but exhibited an intensity variation comparable to a $\cos^2\phi$ dependence corresponding to lasing in $TE_{\phi 1}$ mode. Focusing of the surface emitted light was confirmed from the emission patterns on different planes above the laser surface. The pattern at a distance around 3 mm (close to the designed focal length f = 3.0 mm) exhibited the smallest spot size. The observed focus spot was a nearly circular

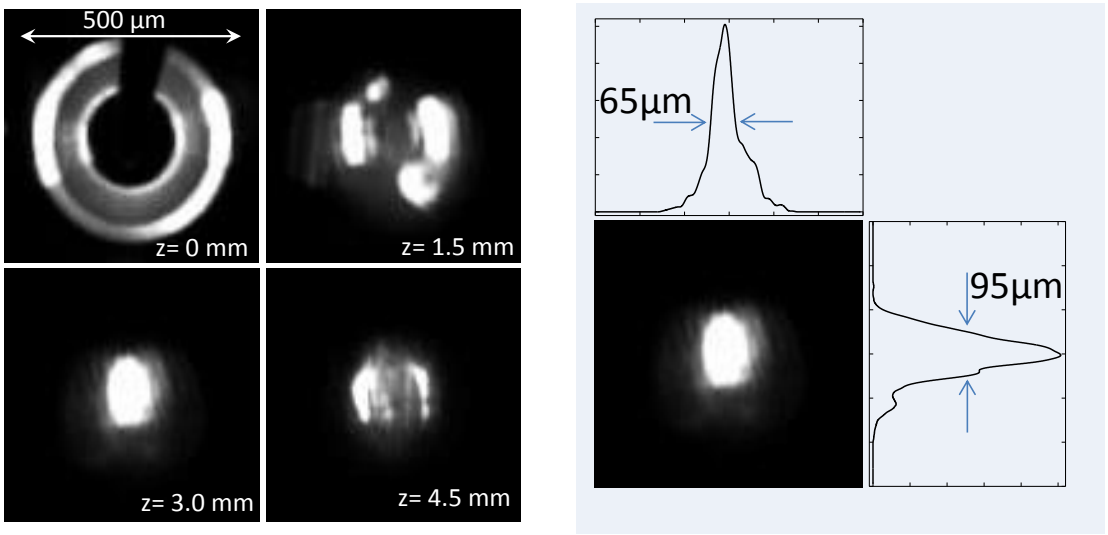

(a) (b)

Figure 2.14 Emission patterns at different distances z from the laser surface at an injection current of 140 mA.

pattern different from doughnut-like or multi-lobe pattern expected for $TE_{\phi 0}$ or $TE_{\phi 1}$ lasing [22]. Figure 2.14 (b) shows the intensity distributions of the focused spot. The full width at half maximum (FWHM) of the focused spot was measured as around 80 μm. This value is comparable with 57 μm calculated from $0.88f\lambda/W$ with f = 3.0 mm and $W = L_{GC}$ = 45 μm, which is an approximate expression of the FWHM focus width of a linear line-focusing element of focal length f and aperture width W.

2.5 Summary

InGaAs QW circular-grating-coupled surface emitting lasers (CGCSELs) using a circular DBR and a circular chirped grating coupler with focusing function, fabricated by EB lithography employing circular scanning, have been demonstrated. Stitching error free smooth circular gratings were fabricated with uniform duty ratio. Single-mode-lasing of the CGCSEL was accomplished under pulse driving. The focusing function of the fabricated GC was confirmed. The output power can be enhanced by adopting first-order DBR grating, reducing the absorption loss in the grating region by area selective QW disordering, and reducing the mismatch between guided modes in active and DBR regions by inserting a transient region.

Chapter 3

Theoretical Analysis and Design of Ring/Fabry-Perot Composite Cavity Lasers

3.1 Introduction

Micro-ring-resonators have demonstrated great promise as fundamental building blocks for a variety of applications in photonics. They can be implemented for such diverse applications such as sensors[69], [70], optical channel dropping filters [71], optical add/drop (de)multiplexers [72], switches [73], routers [74], and logic gates [75]. In addition, when gain is added into the resonators, wavelength selective amplification, oscillation, and lasing become possible [76], [77]. In this chapter, the design considerations and the operating principle of a novel RFP composite cavity laser will be presented. Derivation of lasing condition of composite mode is presented. Selection of the composite cavity mode was discussed by using the mode frequencies of the ring and FP resonators. Possibilities of single mode and two-wavelength lasing operation of RFP lasers are discussed. Details of the waveguide

design, bend loss calculation and tangential coupler design are also presented. Characteristics of the tangential coupler and the bend loss coefficient of the ring waveguide were calculated by the beam propagation method (BPM) simulation.

3.2 Working principle of RFP composite cavity lasers

Figure 3.1(a) shows the schematic of the proposed device geometry consisting of an active circular ring resonator coupled to the middle of an active straight channel waveguide. The ring radius is R, length of the straight waveguide is L, amplitude reflectivities of the two cleaved facets are r_A and r_B, C (C') is the amplitude transmission factor for an input wave at the ring (straight) to the ring (straight) waveguide, and S (S') is the amplitude coupling factor for an input wave at the ring (straight) to the straight (ring) waveguide. Due to the presence of cleaved facets, the FP cavity together with the ring cavity forms a composite cavity. Amplification of optical waves takes place in this laser, when it is excited by carrier injection into the active region with a current across the p-n junction. If the amplification gain becomes sufficiently high, as a result of successive amplification of optical wave

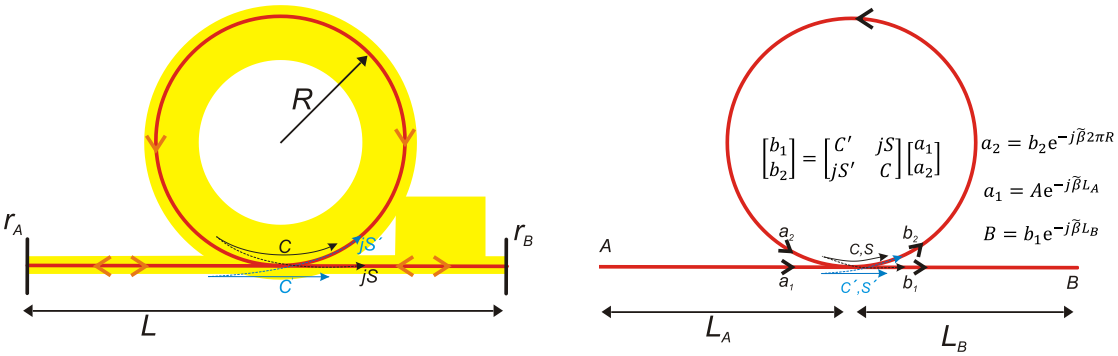

(a) (b)

Figure 3.1 (a) Schematic of the ring / Fabry-Perot composite cavity laser. (b) General description of a ring resonator coupled with a straight waveguide showing the relations between the field amplitudes at different positions.

travelling back and forth through the ring cavity with feedback by the reflection at the facet mirrors, optical energy is accumulated and laser oscillation occurs.

3.3 Analysis of lasing threshold of composite modes

Employing the well-known resonance conditions of each of the cavities, the mode frequency $f_{Rm}$and the mode spacing Δf_R of the ring cavity can be written as

$$\begin{cases} f_{Rm} = \dfrac{c}{2\pi R n_{Re}} m \\ \Delta f_R = \dfrac{c}{2\pi R n_{Reg}} \end{cases}, \tag{3.1}$$

where c is the velocity of light in free space, n_{Re} is the effective refractive index of the ring waveguide, n_{Reg} is the effective group refractive index, and m is the mode number of the ring cavity. Similarly the mode frequency $f_{Fm'}$ and the mode spacing Δf_F of the FP cavity can be written as

$$\begin{cases} f_{Fm'} = \dfrac{c}{2L n_{Fe}} m' \\ \Delta f_F = \dfrac{c}{2L n_{Feg}} \end{cases}, \tag{3.2}$$

where n_{Fe} is the effective refractive index of the straight waveguide, n_{Feg} is the effective group refractive index, and m' is the mode number of the FP cavity. To simplify the following analysis let us assume that $n_{Re} = n_{Fe} = n_e$, and $n_{Reg} = n_{Feg} = n_{eg}$.

Laser oscillation, in general, is no more than maintaining a constant power of a coherent optical wave propagating back and forth in the resonator. Therefore, the oscillation condition is the condition required for the complex amplitude of the wave after a round trip between the mirrors to equal the initial complex amplitude. The tangential coupler suffers from radiation loss because of the mismatch between the guided mode profiles of the ring and straight waveguides. So that the relation between the coupler parameters are $|C|^2+|S|^2<1$ and $|C'|^2+|S'|^2<1$. An expression for

the complex transmittance $\tilde{t}_s$ of the straight waveguide coupled with a ring waveguide can be derived from the relation between the input and output waves as shown in the figure 3.1(b). The complex mode amplitudes at the input and output ports of the straight waveguide are *A* and *B*, respectively. L_A and L_B are the distances between the coupling point to the input port and output port, respectively. Total length of the straight waveguide is $L=L_A+L_B$. Field amplitudes at the input and output ports of the tangential coupler are a_1, a_2, b_1 and b_2. Using the scattering matrix analysis, relation between the field amplitudes are shown in the figure 3.1(b). The expression of the complex transmittance can be written as

$$\tilde{t}_s = \frac{B}{A} = \frac{C' - \eta \mathrm{e}^{-j\tilde{\beta}2\pi R}}{1 - C\mathrm{e}^{-j\tilde{\beta}2\pi R}} \mathrm{e}^{-j\tilde{\beta}L}. \tag{3.3}$$

Here, $\tilde{\beta} = \beta + jg/2$ is the complex propagation constant, $\beta = \frac{\omega}{c} n_e$ is the real part of the propagation constant for a wave of frequency ω, g is the intensity gain factor and $\eta = CC' + SS'$ is a complex quantity depends on the coupler parameters. The lasing condition of the RFP laser can be derived by equating the complex round trip gain, product of the square of the complex transmittance and the reflectivities of the two facet mirrors, to unity.

$$r_A r_B \left(\frac{C' - \eta \mathrm{e}^{-j\tilde{\beta}2\pi R}}{1 - C\mathrm{e}^{-j\tilde{\beta}2\pi R}} \right)^2 \mathrm{e}^{-j2\tilde{\beta}L} = 1,$$

or

$$r_A r_B \left(\frac{-C' + \eta G_R \mathrm{e}^{-j\beta 2\pi R}}{1 - C G_R \mathrm{e}^{-j\beta 2\pi R}} \right)^2 G_L \mathrm{e}^{-j\beta 2L} = 1, \tag{3.4}$$

with $G_R = e^{g\pi R}$ and $G_L = e^{gL}$.

Assume that a composite mode frequency ω is close to the m-th ring mode frequency ω_{Rm} as shown in figure 3.2. Putting $\beta = n_e\frac{\omega}{c} = \beta_{Rm} + \delta\beta = \beta_{Rm} + \frac{n_{eg}}{c}\delta\omega$ and $\beta_{Rm}2\pi R = n_e\frac{\omega_{Rm}}{c}2\pi R = 2\pi m$ into Eq. (3.4), the phase condition can be written as

$$2\arg\left\{\frac{-C' + \eta G_R \mathrm{e}^{-j\delta\beta 2\pi R}}{1 - CG_R \mathrm{e}^{-j\delta\beta 2\pi R}}\right\} - 2(\beta_{Rm} + \delta\beta)L = -2M\pi. \qquad (3.5)$$

Here, M is the composite mode number. Amplitude condition can be written as

$$r_A r_B \frac{(\eta G_R - C')^2 + 4C'\eta G_R \sin^2(\delta\beta\pi R)}{(1 - CG_R)^2 + 4CG_R \sin^2(\delta\beta\pi R)} G_L = 1. \qquad (3.6)$$

The laser oscillation takes place only for the optical waves satisfying both conditions. We consider a case where, the only composite mode can lase, but the ring mode and FP mode do not lase. Ring mode cannot reach the lasing threshold if there is no reflection from the facet mirrors and $G_R C < 1$. Similarly, the FP mode cannot lase if there is no feedback from the ring resonator and $r_A r_B C'^2 G_L < 1$. Lasing condition of the composite mode

Case I: We assume that an m'-th FP mode frequency $\omega_{Fm'}$ coincides with an m-th ring mode frequency ω_{Rm}, i.e., $\omega_{Fm'} = \omega_{Rm}$. Then for a frequency $\omega = \omega_{Rm} = \omega_{Fm'}$ we have $\delta\omega = \omega - \omega_{Rm} = 0$, $\delta\beta = 0$ and $2\beta_{Rm}L = 2\beta_{Fm'}L = 2\pi m'$.

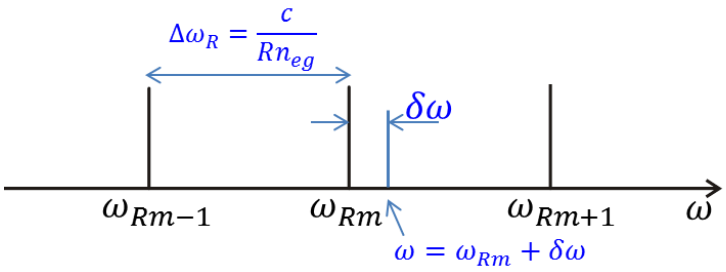

Figure 3.2 Schematic of the ring mode frequencies and a composite mode frequency.

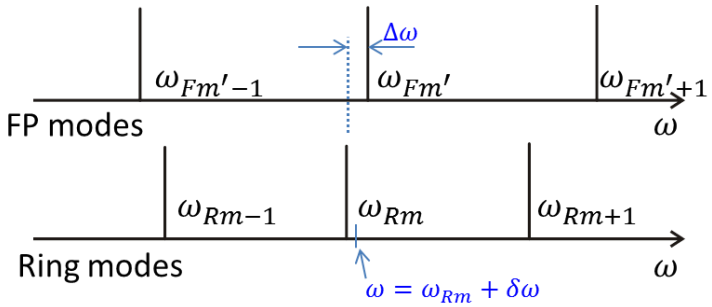

Figure 3.3 Schematic of the ring and FP mode frequencies for the case II.

Therefore, the left hand side of the Eq. (3.5) becomes

$$2\arg\left\{\frac{\eta G_R - C'}{1 - C G_R}\right\} - 2\pi m' = -2\pi(m' + q). \tag{3.7}$$

Here, q=0 or 1 depends on the first term of the left hand side of Eq. (3.7). This means that the phase condition is satisfied by $\omega = \omega_{Rm} = \omega_{FPm'}$. Hence, ω is the composite cavity mode. Using the Eq. (3.4), amplitude condition for this composite mode can be written as

$$r_A r_B \left(\frac{\eta \mathrm{e}^{g\pi R} - C'}{1 - C\mathrm{e}^{g\pi R}}\right)^2 \mathrm{e}^{gL} = 1. \tag{3.8}$$

Left hand side of Eq. (3.8) increases with the gain g and becomes unity for g=g_{th}, i.e., the lasing threshold. The threshold gain cannot be given analytically but can be obtained by graphic method or numerical calculation.

Case II: When an m'-th FP mode $\omega_{Fm'}$ is close to an m-th ring mode ω_{Rm} but is not coincide with ω_{Rm} i.e., $\Delta\omega = \omega_{Fm'} - \omega_{Rm} \neq 0$ but $|\Delta\omega| \ll \Delta\omega_F, \Delta\omega_R$.Then for a frequency $\omega = \omega_{Rm} + \delta\omega$,we have $\delta\beta = \frac{n_{eg}}{c}\delta\omega$, $\beta_{Rm} 2\pi R = 2\pi m$, $\beta_{Fm'} - \beta_{Rm} = \frac{n_{eg}}{c}(\omega_{Fm'} - \omega_{Rm}) = \frac{n_{eg}}{c}\Delta\omega = \Delta\beta$ and $\mathrm{e}^{-j\beta 2\pi R} = \mathrm{e}^{-j\delta\beta 2\pi R}$. Therefore the phase condition given by the Eq. (3.5) becomes

$$2\arg\left\{\frac{-C'+\eta G_R e^{-j\delta\beta 2\pi R}}{1-CG_R e^{-j\delta\beta 2\pi R}}\right\}-2(\delta\beta-\Delta\beta)L=-2(M-m')\pi. \qquad (3.9)$$

For $C<G_R<\frac{1}{C}$, $|\delta\beta 2\pi R|\ll 1$ and $M=m'$, we have

$$2\arg\left\{\frac{-C'+\eta G_R(1-j\delta\beta 2\pi R)}{1-CG_R(1-j\delta\beta 2\pi R)}\right\}-2(\delta\beta-\Delta\beta)L=0,$$

$$\delta\beta=\frac{\Delta\beta}{1+\dfrac{G_R SS' 2\pi R}{(\eta G_R-C')(1-CG_R)L}}. \qquad (3.10)$$

Denominator of the right hand side of Eq. (3.10) is greater than unity if $\eta G_R > C'$, then we have $0<\frac{\delta\beta}{\Delta\beta}<1$ and $0<\frac{\delta\omega}{\Delta\omega}<1$, this means that the composite cavity mode frequency ω is between the FP mode and ring mode i.e., $\omega_{Rm}<\omega<\omega_{Fm'}$ or $\omega_{Fm'}<\omega<\omega_{Rm}$. The amplitude condition of Eq. (3.6) can be written as

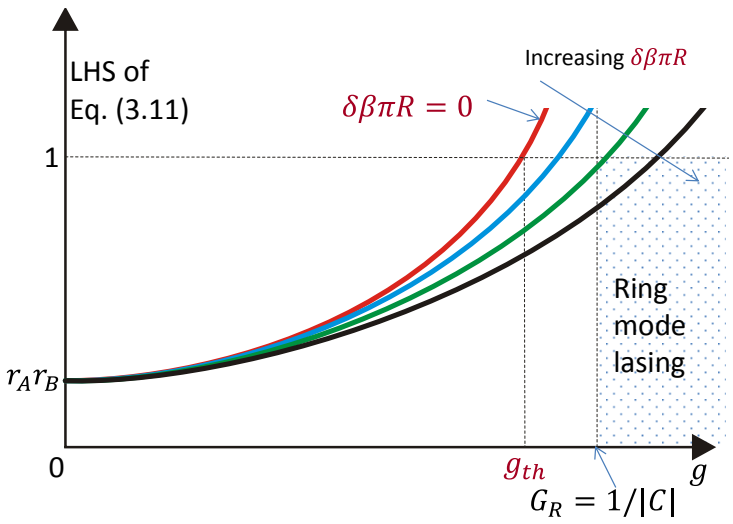

Figure 3.4 Plot of the left hand side of eq. (3.11) vs. intensity gain factor g for different $\delta\beta\pi R$ assuming $|C|=|C'|$.

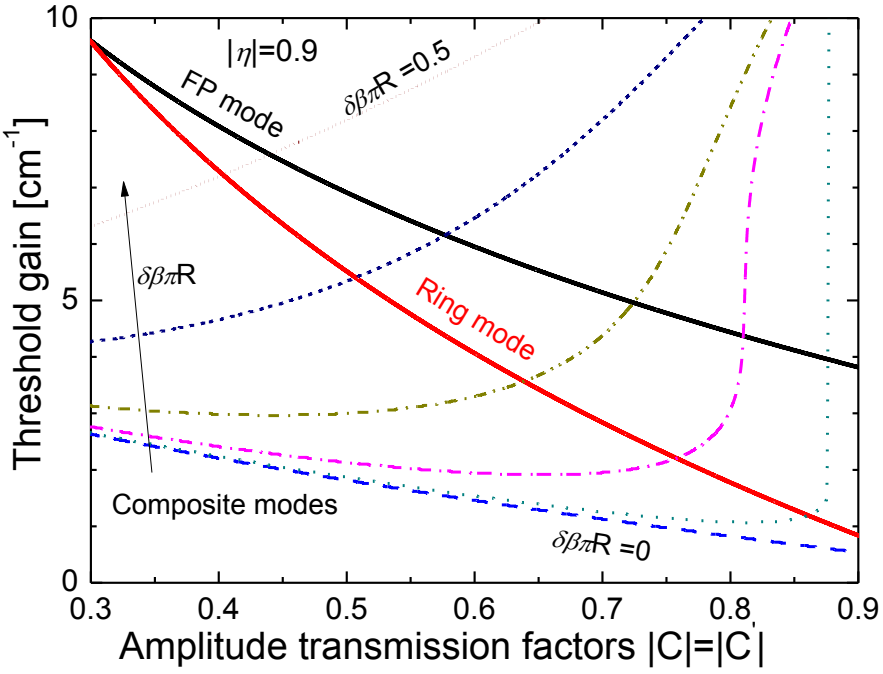

Figure 3.5 Plot of threshold gains of a pure FP mode, pure ring mode and different composite modes vs. the coupler parameters. In these calculations, $|C| = |C'|$, $|\eta|$=0.9, r_A=r_B=0.538, R=400 μm and L=950 μm were used.

$$r_A r_B \frac{(\eta e^{g\pi R} - C')^2 + 4C'\eta e^{g\pi R} \sin^2(\delta\beta\pi R)}{(1 - Ce^{g\pi R})^2 + 4Ce^{g\pi R} \sin^2(\delta\beta\pi R)} e^{gL} = 1. \qquad (3.11)$$

Figure 3.4 shows the plot of the left hand side of Eq. (3.11) vs. the intensity gain factor g for different $\delta\beta\pi R$. Graphs show that the threshold gain g_{th} is minimum for $\delta\beta\pi R = 0$ and increases with the increase of $\delta\beta\pi R$. If ring-FP mode separation $\Delta\omega$ is not small enough then $\delta\beta\pi R$ may be large and the composite mode does not lase. Instead the ring mode may lase.

A comparison between threshold gains for composite modes with different $\delta\beta\pi R$ are shown in figure 3.5. Values of g_{th} for composite modes were calculated numerically using the Eq. (3.11) and the threshold gain for pure FP and ring modes were calculated by using the relations $G_R C = 1$ and $r_A r_B C'^2 G_L = 1$, respectively. Other parameters used in the calculations were 30% power reflectivities for the

cleaved facets, R=400 μm and L=950 μm. Calculation shows that the threshold gain of composite cavity modes are smaller than that of pure FP and ring modes.

3.4 Selection of lasing modes

To explain the single mode lasing, let us consider a ring/FP composite cavity laser as shown in figure 3.6 (a). Schematic representations of the FP, ring, and composite cavity modes of a device of $2R<L<\pi R$ and $\Delta f_F>\Delta f_R$ are shown in figure 3.6(b). At first we assume that an m-th ring mode frequency f_{Rm} coincides with an m'-th FP mode frequency $f_{Fm'}$. Then, the frequency separation between the ($m'+k$)-th FP mode and the ($m+k$)-th ring mode is

$$f_{Fm'+k} - f_{Rm+k} = k(\Delta f_F - \Delta f_R) = k\frac{c}{n_{eg}}\left(\frac{1}{2L} - \frac{1}{2\pi R}\right). \tag{3.12}$$

The separation $|f_{Fm'+k} - f_{Rm+k}|$ increases with k (k =1,2,….) as shown by the red dotted horizontal arrows in figure 3.6(b). The frequency separation between the ($m'+k$-1)-th FP mode and the ($m+k$)-th ring mode is

$$f_{Fm'+k-1} - f_{Rm+k} = (k-1)\Delta f_F - k\Delta f_R\,. \tag{3.13}$$

However, the separation $|f_{Fm'+k-1} - f_{Rm+k}|$ decreases with k (shown by the blue dotted horizontal arrows) and becomes minimum at

$$k = \left[\frac{\Delta f_F}{\Delta f_F - \Delta f_R}\right]_{\text{int}} = \frac{\Delta f_F}{\Delta f_F - \Delta f_R} + \varepsilon\,, \tag{3.14}$$

where $[\ \ ]_{\text{int}}$ denotes the rounding into an integer and $|\varepsilon|<1/2$ is the rounding error. The minimum $|f_{Fm'+k-1} - f_{Rm+k}| = |[\Delta f_F/(\Delta f_F - \Delta f_R)]_{\text{int}}(\Delta f_F - \Delta f_R) - \Delta f_F|$ is smaller than $(\Delta f_F - \Delta f_R)/2$, and the minimum is also smaller than $|f_{Fm'+1} - f_{Rm+1}|$ and $|f_{Fm'+2} - f_{Rm+2}|$. Similarly, even if f_{Rm} does not coincide exactly with $f_{Fm'}$ but is close to it so that $|f_{Fm'} - f_{Rm}| < (\Delta f_F - \Delta f_R)/2$, there exist a mode

pair $f_{Fm'+k-1}$ and f_{Rm+k} with the minimum separation $|f_{Fm'+k-1} - f_{Rm+k}| < (\Delta f_F - \Delta f_R)/2$. This means that ring /FP mode pairs of minimum separation are arranged nearly periodically with an approximate period given by $(k-1)\Delta f_F \approx k\Delta f_R \approx \Delta f_F \Delta f_R/(\Delta f_F - \Delta f_R)$.

According to the analysis of the lasing condition of composite mode

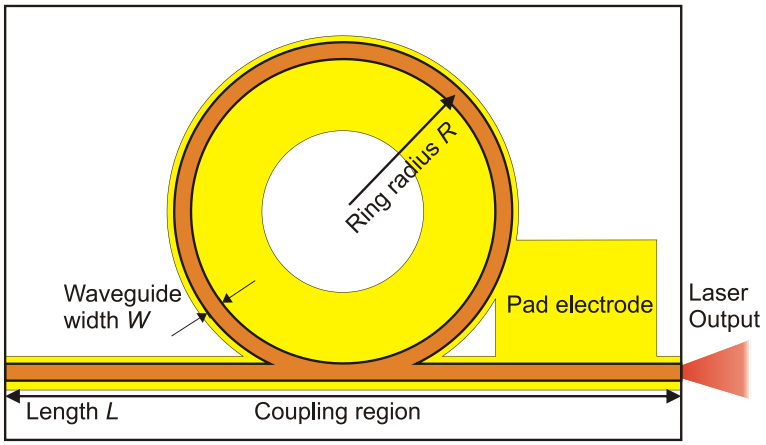

(a)

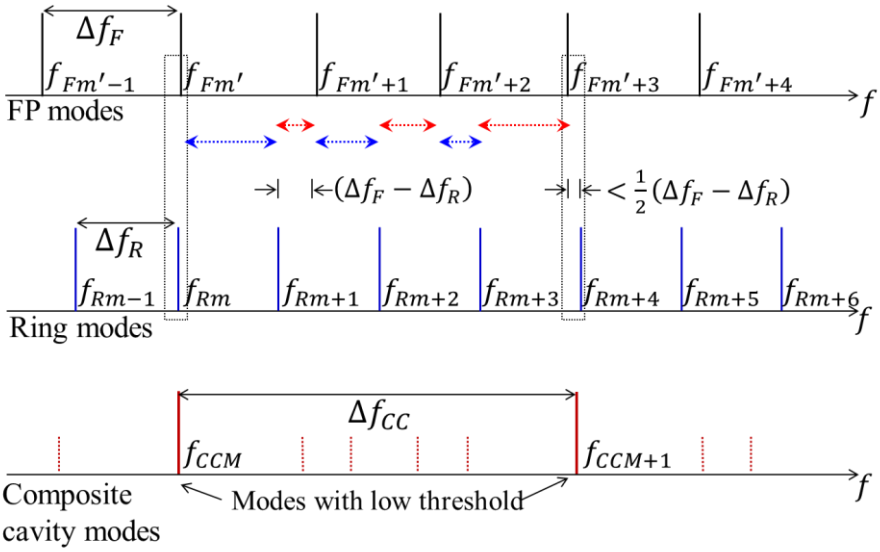

(b)

Figure 3.6 (a) Schematic of a ring / Fabry-Perot composite cavity laser with common electrode for current injection. (b) Schematic diagram illustrating the relationships between the cavity modes of FP, ring, and composite cavities.

presented in the previous section shows that, if $f_{Rm} = f_{Fm'}$, the composite cavity mode is at this frequency and the laser lases above a threshold gain, and if $f_{Rm} \neq f_{Fm'}$ but $f_{Rm} \approx f_{Fm'}$, the laser can lase at a frequency between f_{Rm} and $f_{Fm'}$ above a threshold gain somewhat higher than that for $f_{Rm} = f_{Fm'}$. Therefore, the composite cavity modes with low threshold gain are separated by an approximate period Δf_{CC} as shown in the lower part of figure 3.6(b).

$$\Delta f_{CC} \approx \frac{\Delta f_F \Delta f_R}{\Delta f_F - \Delta f_R} = \frac{c}{2n_{eg}(\pi R - L)} \tag{3.15}$$

Therefore, the RFP laser can realize quasi single mode lasing at one of these mode frequencies, closest to the gain peak, with a side-mode suppression ratio (SMSR) higher than that of an ordinary FP laser.

3.5 Two-wavelength lasing and wavelength tuning mechanism

Two-wavelength lasing of a single RFP laser would be possible if the injection currents to the ring and FP section are controlled independently. Figure 3.7 shows

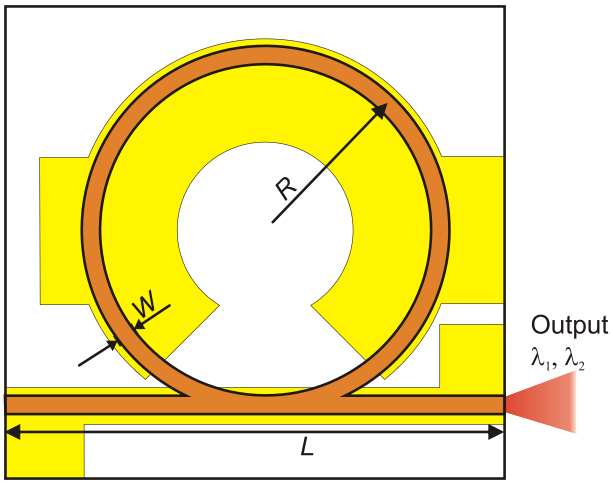

Figure 3.7 Schematic of a ring / Fabry-Perot composite cavity laser with two separate p-electrodes.

the schematic of the RFP laser geometry with two separate p-electrodes to control the injection currents to the ring section (I_R) and straight section (I_F) independently. The mode frequencies and mode spacings of the ring and FP cavities can be expressed by the Eqs. (3.1) and (3.2). The FP and ring cavity mode frequencies of an RFP laser of $2R<L<\pi R$ ($\Delta f_F>\Delta f_R$ for $n_{Reg}\approx n_{Feg}$) are shown schematically in figure 3.8(a) and (b). It can be easily shown that the ring/FP mode pairs of minimum separation are arranged nearly periodically with an approximate period of

$$\Delta f_{CC} \approx \frac{\Delta f_F \Delta f_R}{\Delta f_F - \Delta f_R} = \frac{c}{2(\pi R n_{Reg} - L n_{Feg})}. \tag{3.16}$$

The FP cavity with the cleaved facets and the ring cavity coupled to each other form a composite resonator. At first we assume that the m-th ring mode f_{Rm} coincides with the m'-th FP mode $f_{Fm'}$ ($f_{Rm}= f_{Fm'}$), then the position of the adjacent ring/FP

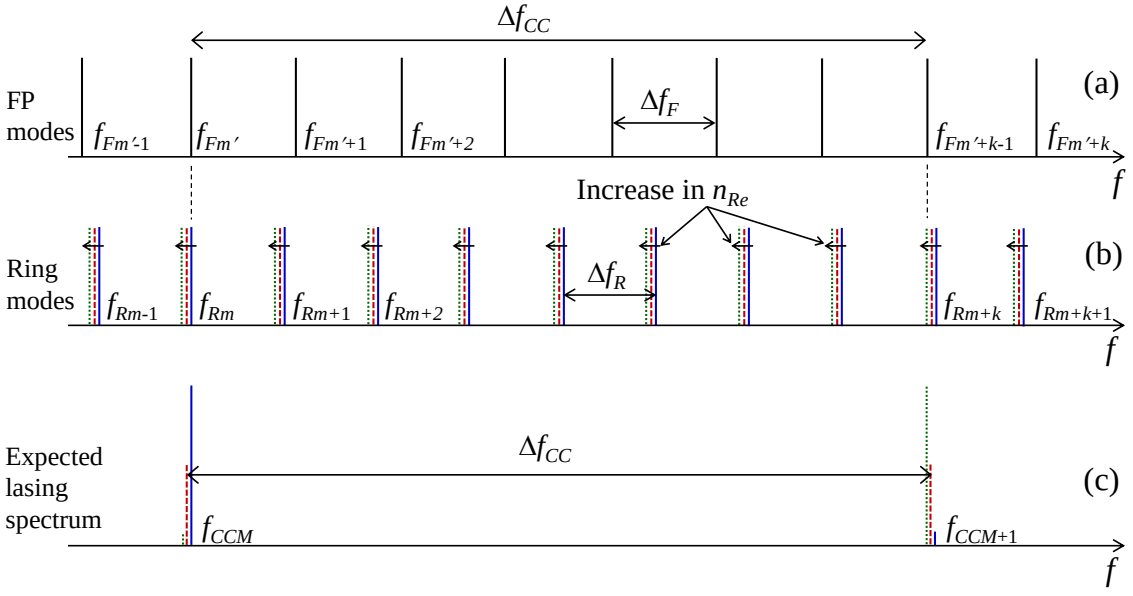

Figure 3.8 Schematic diagram illustrating the relationships between the cavity mode frequencies. (a) FP cavity modes. (b) Ring cavity modes. Blue solid lines are for the starting value of n_{Re}. Red dashed and green dotted lines are for the n_{Re} with increase of I_R. (c) Expected lasing spectra of the RFP laser for three different values of I_R.

mode pair of minimum separation is around $f_{Rm}+\Delta f_{CC.}$ We also assume that the separation between the ring and FP modes around $f_{Rm}+\Delta f_{CC}$ is positive ($f_{Rm+k} > f_{Fm'+k-1}$) as shown by the blue solid vertical lines in figure 3.8(b). When I_R is increased with keeping I_F at a fixed value, n_{Re} increases due to the temperature rise in the active region, and f_{Rm} shifts to lower frequency with slight shrinkage of Δf_R as shown by the red dashed lines in figure 3.8(b). The separation $f_{Fm'}-f_{Rm}$ increases and the separation $f_{Rm+k}-f_{Fm'+k-1}$ decreases continuously, and these separations can be made equal. Further increase of I_R causes the coincidence between the ring and FP modes at $f_{Rm}+\Delta f_{CC}$ ($f_{Rm+k} = f_{Fm'+k-1}$) and the separation $f_{Fm'}-f_{Rm}$ increases more as shown by the green dotted lines in figure 3.8(b). Similar vernier effect can be obtained more generally including cases starting with $f_{Rm} \neq f_{Fm'}$ and/or $f_{Rm+k} < f_{Fm'+k-1}$, only if the shift of f_{Rm} up to Δf_F is available. Similar vernier effect can be obtained also by keeping I_R constant and changing I_F.

Analysis of lasing condition, given by complex round trip gain between facet mirrors of the RFP laser equated to unity, shows that the close ring/FP mode pairs gives rise to the composite cavity modes of low threshold gain arranged with a period Δf_{CC}. For a given constant value of gain in the FP (ring) cavity below the pure FP (ring) lasing threshold, the threshold of the gain in the ring (FP) cavity for the composite mode lasing is lower for smaller frequency separation between the pair of ring and FP modes from which the composite mode originates.

It is known, through the rate equation analysis of multimode steady-state lasing using a given spontaneous emission coupling coefficient, that the output powers of each mode are inversely proportional to the difference between the threshold gain G_{th} (gain required for oscillation without spontaneous emission coupling) and the effective gain G_e (gain actually realized by current injection) of each mode [66]. This means that the smaller $G_{th}-G_e$ is, the larger the mode output power is. From these considerations it is expected that simultaneous lasing of two composite modes (two wavelengths) with nearly equal output powers can be accomplished in the RFP laser by fine controlling the injection currents I_R and I_F so

as to find in the effective gain bandwidth such condition that the frequency separation between a pair of ring and FP modes close to each other is approximately equal to the separation between another pair, and therefore the values of (threshold gain – effective gain) of the composite modes originating from these pairs are approximately equal to each other. This two wavelength lasing is shown by the red dashed vertical lines in figure 3.8(c). The frequency separation between the two lasing composite modes is close to integer multiple of Δf_{CC}, since similar vernier effect can be obtained also with mode pair around $f_{Rm}+j\Delta f_{CC}$ ($j=\pm1, \pm2,\ldots$). In order to confirm this possibility, we actually fabricated the RFP laser and examined the performances by experimental measurements presented in chapter 5.

3.6 Design of RFP lasers

RFP laser can be fabricated on any direct bandgap semiconductor material system. A deciding factor on the device performance however mainly comes from the

Table 3.1 Material, thickness, and the refractive index of each of the layers of the epitaxial structure used for designing the RFP lasers.

Layer	**Material**	**Thickness [μm]**	**Refractive index at 800nm**
Contact layer	GaAs	0.2	3.675
Upper buffer layer	$Ga_{0.51}In_{0.49}P$	0.05	3.227
Upper cladding layer	$(Al_{0.55}Ga_{0.45})In_{0.49}P$	1	3.145
Upper guided layer	$Ga_{0.51}In_{0.49}P$	0.5	3.227
Quantum well layer	$GaAs_{0.86}P_{0.14}$	0.013	3.56
Lower guided layer	$Ga_{0.51}In_{0.49}P$	0.5	3.227
Lower cladding layer	$(Al_{0.55}Ga_{0.45})In_{0.49}P$	1	3.145
Lower buffer layer	GaAs	0.5	3.675
Substrate	GaAs	~625	3.675

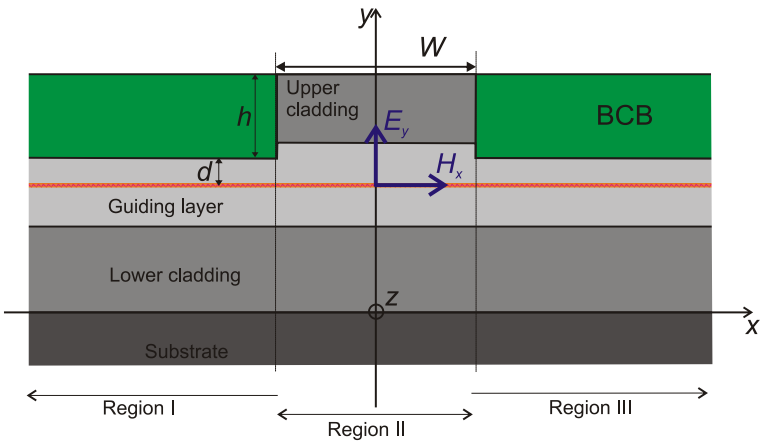

(a)

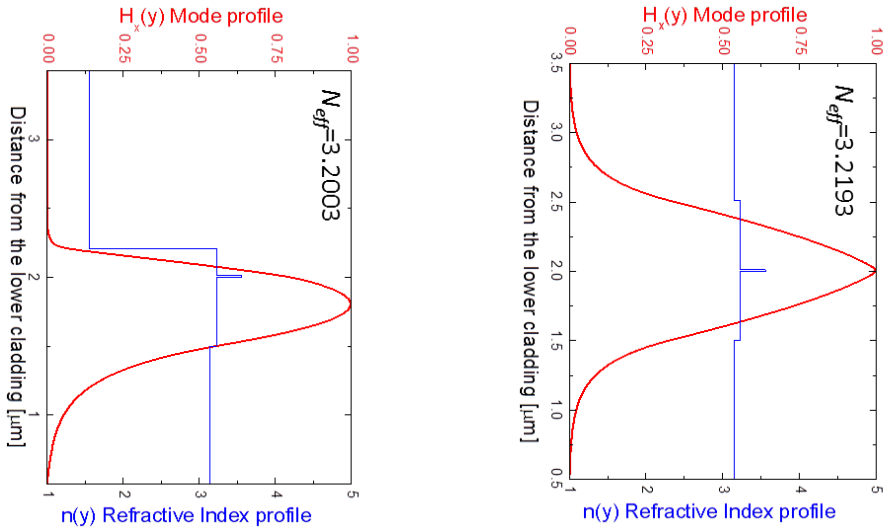

(b)

Figure 3.9 (a) Schematic of cross sectional view of the ridge waveguide. (b) TM guided mode profile of the core (region II) and cladding (region I and III) sections.

successful merging of available technologies and powerful design. I designed the RFP laser using a $GaAs_{0.86}P_{0.14}$ tensile strained single-quantum-well (SQW) in a separate confinement heterostructure (SCH) with $Ga_{0.51}In_{0.49}P$ guiding layers. Specification of the epitaxial structure is listed in table 3.1.

3.6.1 Waveguide design

Design of the waveguide structure for RFP laser is very critical because the straight and ring waveguides should have the same width and ridge height for fabrication simplicity. I employed shallow etched ridge structure for both of the straight and ring waveguides. In such a waveguide the effective refractive index difference of the etched and non-etched areas confines the light horizontally, while the vertical confinement comes from the core-cladding refractive index difference. Due to the weak horizontal confinement the optical mode suffers from the bending losses while propagating through the ring waveguide. On the other hand, the shallow etch is advantageous for keeping the sidewall recombination minimal because the active layer is not exposed to the sidewalls of the ridge waveguide. Furthermore, as the etching does not penetrate into the core, the sidewall roughness induced scattering loss is much smaller than deep etched waveguide. Low bending losses and single transverse mode propagation are the main requirements of the RFP laser geometry.

To determine the waveguide width, at first the 3D structure of the ridge type structure was simplified into 2D structure by using the effective index method [66]. Since the tensile strained GaAsP QW material has higher TM mode gain so that the TM mode lasing is expected. The major field components of the guided mode in the ridge type waveguide are H_x and E_y. Schematic view of the cross-section of a ridge waveguide is shown in figure 3.9(a). Direction of wave propagation is along the z axis. This structure can be converted into an equivalent planar waveguide by using the effective index method [66]. The refractive indices of the cladding and core regions of the converted equivalent planar waveguide are the effective refractive indices of the imaginary planar waveguides with refractive index distribution $n(y)$ along y direction in the region I and II, respectively. Let $H_x(y)$ be the magnetic field amplitude of a TM guided mode in the imaginary planar waveguide, then satisfies the wave equation for a planar guide:

$$\frac{d^2H_x}{dy^2} + k_0^2\{n^2(y) - N_{eff}^2\}H_x = 0, \qquad (3.17)$$

where N_{eff} is the effective refractive index for the planar guide. The $H_x(y)$ mode profiles were computed by using finite element method (FEM) simulation for the

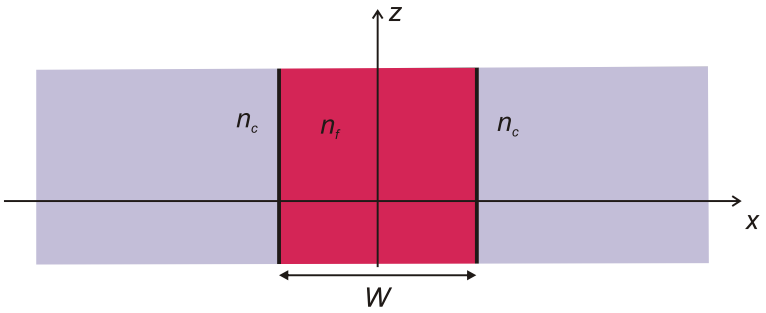

(a)

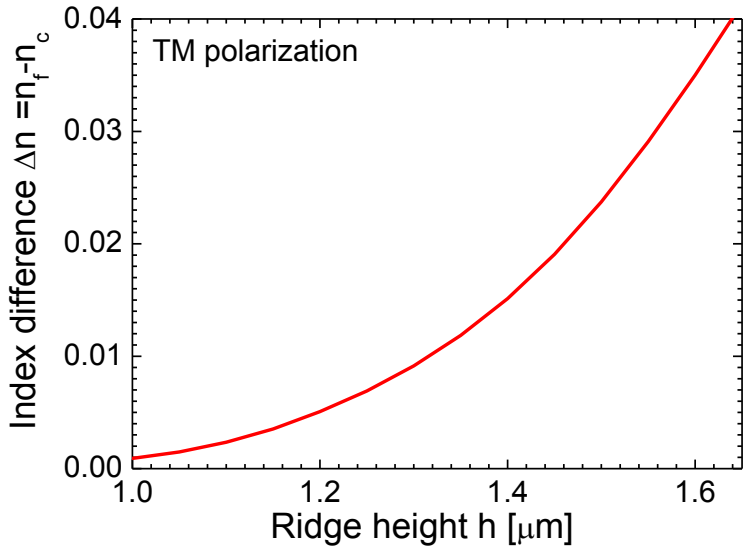

(b)

Figure 3.10 (a) Equivalent 2D waveguide converted by the effective index method. (b) Dependence of core-cladding refractive index difference $\Delta n = n_f - n_c$ on the ridge height *h*.

multilayer planar waveguide. The computed $H_x(y)$ mode profiles, refractive index distribution $n(y)$ and effective refractive indices of the imaginary planar waveguide at the regions I and II are shown in figure 3.9(b). Calculations were done for h=1.45μm and wavelength of 800 nm. The schematic of the equivalent 2D waveguide is shown in figure 3.10(a). Guide layer thickness of the converted 2D waveguide is same as the width of the ridge waveguide. The cladding (n_c) and core (n_f) refractive indices are the effective refractive indices for region I and II, respectively. Dependence of core-cladding refractive index difference $\Delta n = n_f - n_c$ on the ridge height h is shown in the figure 3.10(b). Graph shows that Δn increases

with the increase of ridge height. The normalized frequency V_{cm} [66] corresponding to the cutoff of the m-th mode is $V_{cm} = m\pi$. Using the values of n_f and n_c, maximum width of a single mode waveguide can be calculated by the following inequality

$$W < \frac{\lambda}{2} \frac{1}{\sqrt{n_f^2 - n_c^2}}. \tag{3.18}$$

3.6.2 Calculation of bend loss

To calculate the bend loss factor of a ring waveguide of radius *R*, at first the 3D waveguide of ridge type structure was simplified into 2D structure by using the effective index method. For a waveguide of 3μm width and 1.45μm ridge height, n_f=3.2193 and n_c=3.2003 were calculated by finite element method simulation. Effective refractive indices were calculated for planar waveguide fundamental mode of TM polarization. Figure 3.11(a) shows the schematic of a part of the ring waveguide. Part of the curved waveguide was converted into an equivalent straight waveguide by conformal transformation method as described in Appendix A.3. Equivalent straight waveguide converted by conformal transformation is indicated by pink color. Refractive index profile $n(x)$ at Z=0 position before and after the conformal mapping are shown in figure 3.11(b) by black and red lines, respectively. Fundamental guided mode of TE polarization for the step index waveguide was calculated as shown in figure 3.11(b) by black line. Using this mode profile as an input wave, the mode profile of the equivalent straight waveguide was calculated by BPM. The mode profile of the input wave transforms into the mode profile of that waveguide during the propagation through it. Figure 3.11(c) show the amplitudes of the guided mode at different propagation distances and the mode profile at the output port is the mode profile of the equivalent straight waveguide. This mode profile is shown in figure 3.11(b) by red line. To calculate losses inherent in bent waveguide, the calculated bend mode profile was lunched and propagated through

the converted straight waveguide. The power in the waveguide was monitored with respect to the initial launched mode power. BPM simulation results are shown in figure 3.11(d) and (e). Contour plot of the bend mode propagation through the waveguide shows that there is a continuous loss of power by the radiating tail of the bend mode. It can be seen from the refractive index distribution of the equivalent

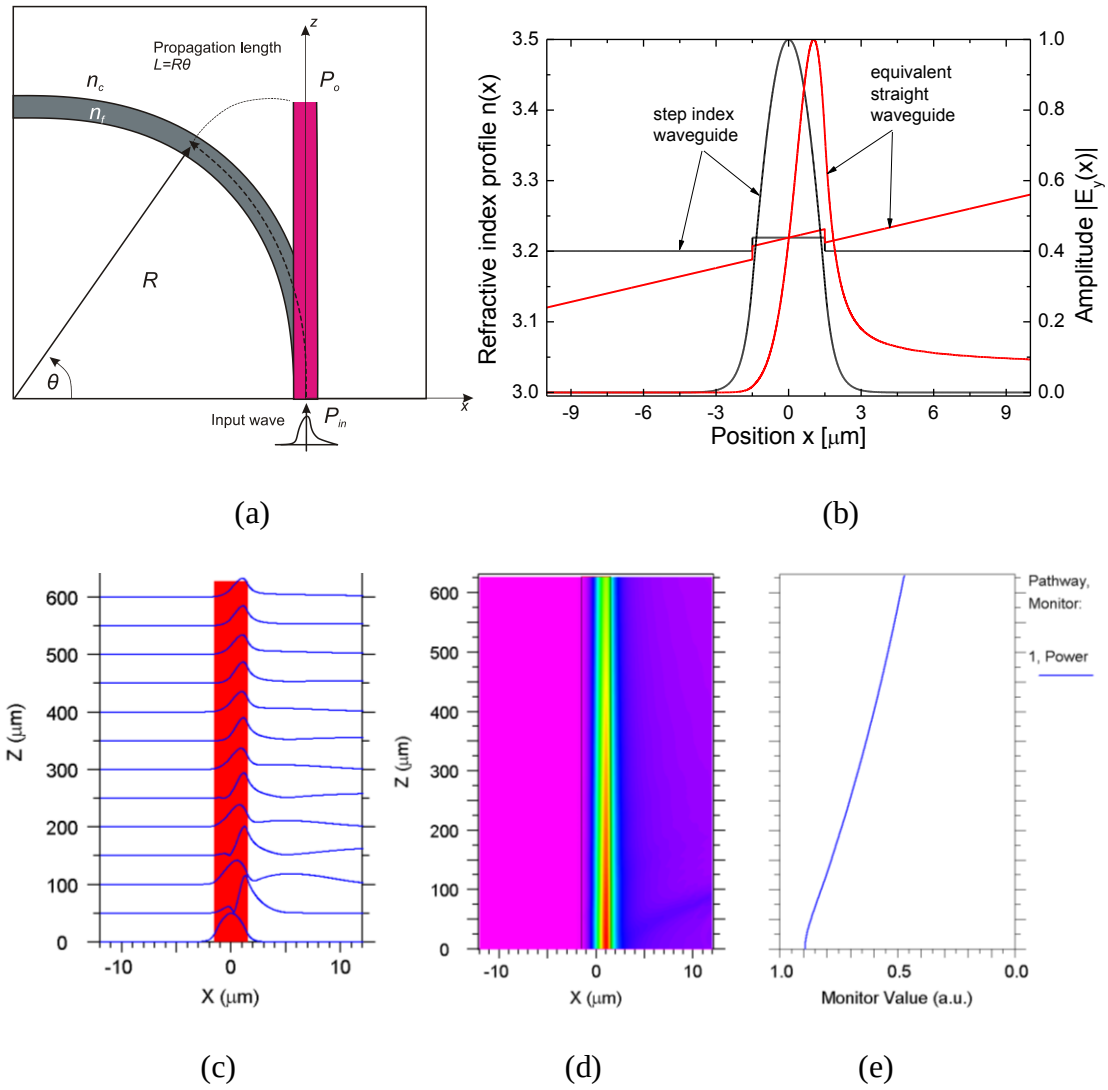

Figure 3.11 (a) Schematic of part of ring waveguide. Equivalent straight waveguide converted by conformal transformation is indicated by pink color. (b) TE polarization guided mode profile of at Z=0 position before and after the conformal mapping (c) Simulation result for calculating the guided mode profile of the equivalent straight waveguide. (d) Contour plot of the bend mode propagation through the waveguide. (e) Power of the guided mode remains in the waveguide during propagation of the wave. Exponential decay of the graph indicates the loss of guided mode power due to the waveguide bending.

straight waveguide that the cladding layer index at the right side becomes higher than the effective refractive index of the guided mode. As a result, the oscillating nature of the mode field in that region causes the power loss. Power monitor graph shows the guided mode power remained in the waveguide during propagation of the wave. Exponential decay of the graph indicates the loss of guided mode power due to the waveguide bending. In theory, power in the curved waveguide decreases exponentially at a rate that represents the bending loss. Neglecting other loss factors, relation between lunched power (P_{in}) and the monitored power (P_o) after the propagation length of $L=R\theta$ can be written as

$$P_o = P_{in} \exp(-\alpha_b L), \tag{3.19}$$

$$\alpha_b = \frac{\ln\left(\frac{P_{in}}{P_0}\right)}{L}. \tag{3.20}$$

Simulation was done with the above mentioned parameters with R=400 μm and θ=90°. From the simulation result shown in figure 3.11(e) it can be seen that the power at the input is P_{in}=0.89 and at the output is P_o=0.47. Using the Eq. (3.20), bend loss factor $\alpha_b = 10.2$ cm^{-1} was calculated. Similar calculations were done repeatedly for obtaining the dependence of α_b on R. Figure 3.12 shows the dependences of α_b on R calculated for h=1.45, 1.5 and 1.55 μm. Bend loss factor decreases with the increase of R and also with the increase of ridge height.

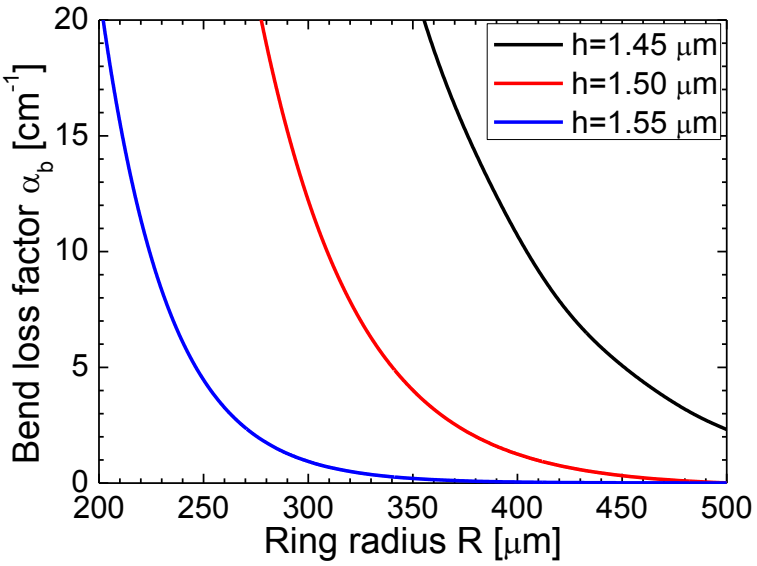

Figure 3.12 Dependence of bend loss factor α_b on the ring radius calculated for three different ridge heights.

3.6.3 Coupler design

An important part of RFP laser is the output coupler. The most important factors on deciding the appropriate coupler configuration are coupling efficiency, back reflection to the cavity and fabrication tolerance. The available coupling techniques can be classified as follows: Y-junction couplers, MMI couplers, evanescent field or directional couplers. Several ring lasers can be found in the literature using one of the three techniques. In this work I used a tangential coupler to couple the ring with straight waveguide. The tangential coupler is formed by superposition of the ring waveguide on the straight channel so that it can be considered as a combination of back to back connected asymmetric Y-junction power combiner and splitter. Schematic of the tangential coupler is shown in figure 3.13. When the guided modes of the ring and straight waveguides approaching to the junction are in same phase and equal amplitude, they excite only the fundamental mode at the branching point. The excited fundamental lateral mode is transformed to the fundamental mode of the single mode waveguide at the middle of the tangential coupler. As the guided mode from the middle of the coupler region propagates towards the branching point at the

other end, power is divided unequally into the two output waveguides. This coupler has the most compact geometry as compared to MMI coupler or directional coupler and easy to fabricate since it does not require narrow gap between waveguides.

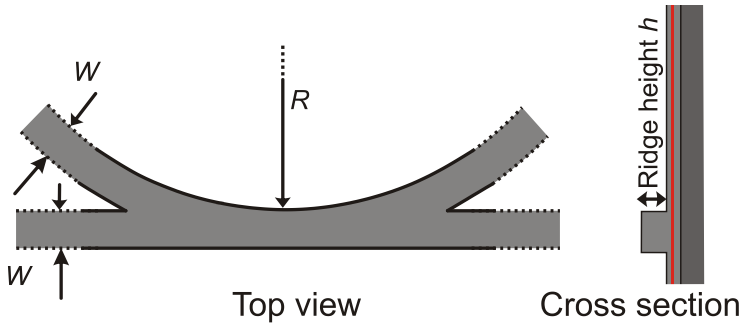

Figure 3.13 Schematic of the top view of the tangential coupler and cross sectional view of the ridge waveguide.

Characteristics of the tangential coupler were determined by 2-dimensional BPM simulation. Launching the fundamental TE guided mode of unity power at the input port of the straight or ring waveguide, partial powers were monitored into the waveguides. Figure 3.14 show the field intensity distributions and the partial powers in the waveguides at every position along the propagation direction for 4 different cases. Figure 3.14 (a) show the simulation results for a device with parameters of W=3.0 μm, R=400 μm, h=1.45 μm. When the input wave of unity power is at the straight waveguide, pathway monitors show that the powers at the output ports of the ring and straight waveguides are 0.05 and 0.83, respectively. This means that the power efficiency of coupling to the ring is $|S'|^2$ =0.05 and the power efficiencies of transmission through the straight guide is $|C'|^2$ =0.83. Similarly, when the input wave is at the ring waveguide, the power coupling efficiency from the ring to the straight waveguide is $|S|^2$ =0.16 and the power transmitted through the coupler to the output port is $|C|^2$ =0.80. Similar calculations are done also for a device with parameters of W=3.0 μm, R=395 μm and h=1.55 μm. Results are shown in the

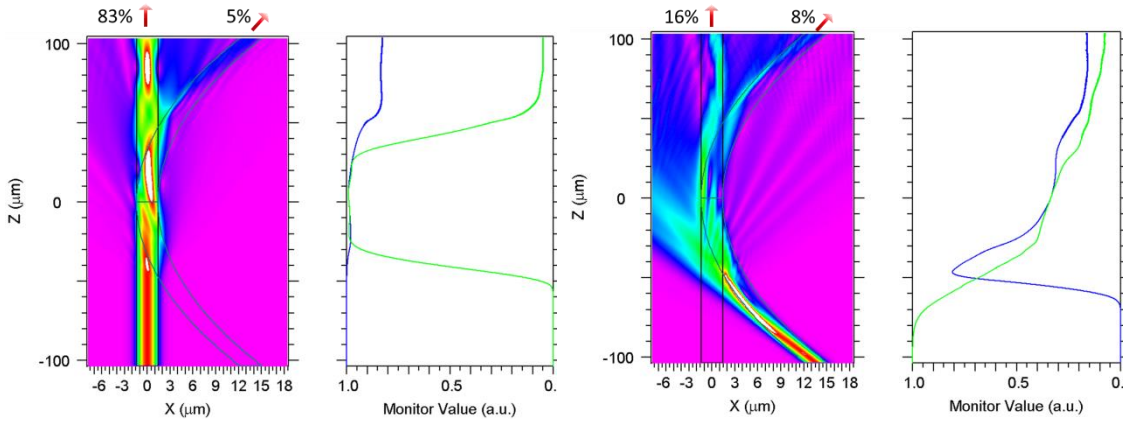

(a)

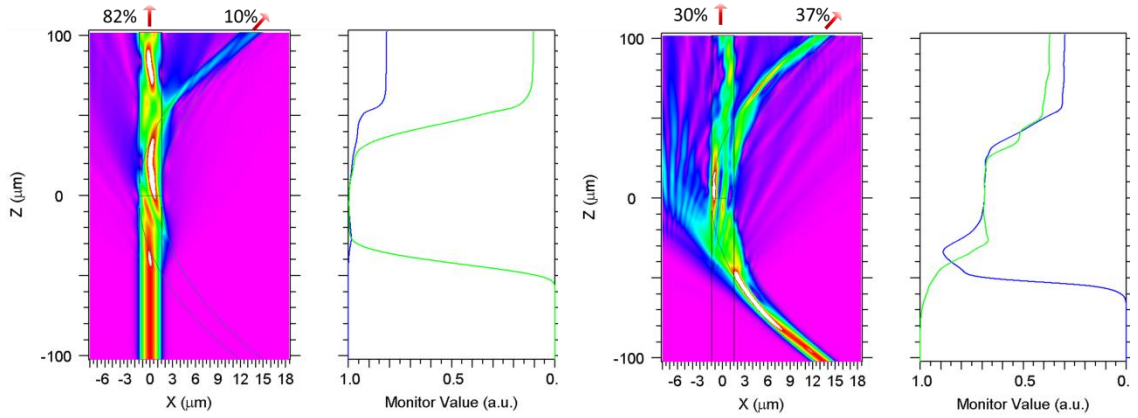

(b)

Figure 3.14 Two-dimensional BPM simulation results of the tangential coupler for two different design parameters (a) *W*=3.0 μm, *R*=400 μm, *h*=1.45 μm used in single mode RFP laser and (b) *W*=3.0 μm, *R*=395 μm, *h*=1.55 μm used in two-wavelength RFP laser.

figure 3.14(b). Calculated parameters of this tangential coupler are $|S'|^2 = 0.10$, $|C'|^2 = 0.82$, $|S|^2 = 0.30$ and $|C|^2 = 0.37$.

3.7 Summary

Working principle of a novel RFP composite cavity laser was explained. Lasing conditions of the composite cavity mode was derived. Selection of the composite

cavity mode was discussed by using the mode frequencies of the ring and FP resonators. Possibilities of single mode and two-wavelength lasing operation of RFP lasers were discussed. Details of the waveguide design, bend loss calculation and tangential coupler design were presented.

Chapter 4

Single-Mode RFP Composite Cavity Lasers

4.1 Introduction

Single-longitudinal-mode semiconductor lasers are very attractive light sources for many applications including fiber optic communication [78], sensing [79], and THz wave generation [80]. Distributed feedback (DFB) and distributed Bragg reflector (DBR) lasers are well established devices as single mode lasers but they require complicated fabrication processes such as regrowth and grating fabrication. Low-cost devices with simple fabrication process are still required in many applications. Several techniques were employed to realize simple single mode lasers. By etching a few shallow slots on the ridge of a Fabry-Perot (FP) laser, constructive interference of the cavity can be utilized to manipulate the lasing condition and suppress unwanted FP side modes [81], [82]. Several composite cavity structures were studied theoretically and experimentally including cleaved coupled cavity, V-coupled cavity and multi-section lasers [83]–[86]. They required deeply etched

mirrors with narrow gaps and vertical side walls. Ring-resonator-based lasers were also reported. Some of them require integration of active and passive sections as well as deep etching [87]. Ring lasers with simple fabrication process were also reported but they exhibited directional instability [88], [89]. Generally, a microring laser is expected to operate in multiple longitudinal modes and two propagating directions [46]. Unidirectional operation in nearly single-mode microring lasers has already been demonstrated. Control of the lasing direction was accomplished either with external optical injection [90] or special designs using selective electrical pumping [91]. Most recently a square ring / FP composite cavity laser, where deeply etched total internal reflector mirrors and a multimode interference (MMI) coupler were used to form a ring cavity and couple it with the FP cavity, was reported [56], but the fabrication process was complex.

In this chapter, the fabrication and experimental results of a simple circular ring / FP (RFP) composite cavity semiconductor laser are presented. RFP laser was fabricated by EB lithography and RIE processes. P-I characteristics, lasing spectrum and near-field pattern were measured under continuous wave (CW) operation. Temperature dependence of the lasing wavelength was also measured by changing the operating temperature using a thermo-electric temperature controller.

4.2 Design parameters

Figure 4.1 shows the schematic of the proposed device geometry consisting of an active circular ring resonator coupled to the middle of an active straight channel waveguide by a tangential coupler. Ridge type single-mode waveguides with the same width are used for both of the ring and straight waveguides. The tangential coupler is formed by arranging so that the two edges of the straight channel are tangents of the inner and outer edges of the ring waveguide. Coupling between ring and straight waveguide occurs by the overlap between their guided modes at the coupler region. This coupler has a compact geometry as compared with directional coupler [92], [93], and is easy to fabricate since it does not require narrow gap

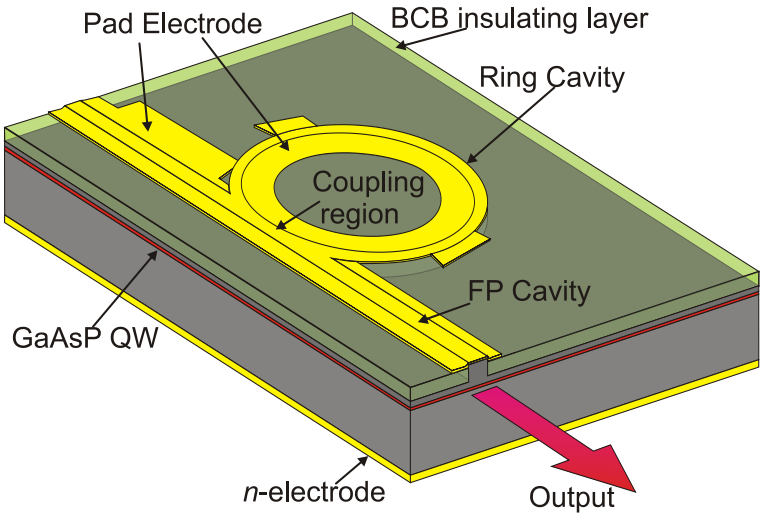

Figure 4.1 Schematic of the single mode ring / Fabry-Perot composite cavity laser.

between waveguides. Although the coupler suffers from radiation loss, it can be compensated by the laser gain.

I designed a ridge channel waveguide using a $GaAs_{0.86}P_{0.14}$ tensile strained single-quantum-well (SQW) in a separate confinement heterostructure (SCH) with $Ga_{0.51}In_{0.49}P$ guiding layers. The gain for the TM mode is larger than that for the TE mode; therefore, TM mode lasing near the gain peak wavelength of ~800 nm is expected. The ridge width and height were determined as 3.0 μm and 1.45 μm, respectively. The ring waveguide suffers from radiation loss due to the waveguide bend. Dependence of bend loss on the ring radius was calculated by the beam propagation method (BPM). The ring radius was determined as R=400 μm, and the bend loss factor calculated for a TM fundamental mode was 10.2 cm^{-1}, which can be compensated by the gain available at the active ring waveguide. Figure 4.2 shows the specifications of the tangential coupler structure designed for this RFP laser. The coupler length of 98 μm is shorter than the lengths of 500 μm and 300 μm for the directional coupler used in previous works [92], [93]. Analysis of the tangential coupler based on the 2-dimensional BPM simulation showed that, for an input wave

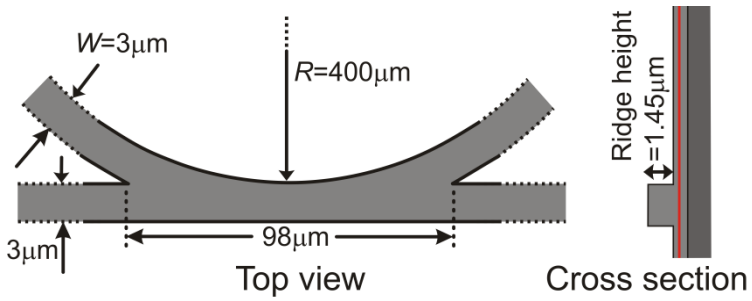

Figure 4.2 Specifications of the fabricated tangential coupler structure.

from the straight (ring) guide, the power efficiencies of coupling to the ring (straight) guide and transmission through the straight (ring) guide are 5% and 83% (16% and 8%), respectively. The FP cavity length was selected as L=950 μm to satisfy $2R<L<\pi R$. According to the analysis presented in the section 3.4, the value of k=4 was calculated by using the Eqs. (3.1), (3.2) and (3.14). Separation between the composite cavity modes with low threshold gain is $\Delta f_{CC} \approx 4\Delta f_R \approx 3\Delta f_F$.

4.3 Fabrication of single-mode RFP lasers

4.3.1 Overview of the fabrication process

The designed RFP laser was fabricated by using a $GaAs_{0.86}P_{0.14}$ SQW epitaxial structure. Details of the epitaxial structure were given in the table 3.1. Fabrication process can be divided into three parts such as: (1) ridge structure formation, (2) planarization by BCB layer and (3) p-side and n-side electrode formation. Details of these fabrication processes are explained in the following sections.

4.3.2 Formation of ridge waveguide structure

The ring and straight waveguides were fabricated by electron beam (EB) lithography and reactive ion etching (RIE). Schematic representation of the fabrication steps are shown in figure 4.3. At first, a 0.5 μm thick ZEP-520A EB resist layer has been spin coated. The EB writing system (Elionix ELS3700S) with a special pattern generator, designed for writing arbitrarily curved lines, was used. The ring waveguide patterns were written by multiple circular scanning with radial steps of 50 nm. The EB acceleration voltage was 30 kV, the beam current was 0.3 nA, writing field size was 1 mm × 1 mm, and the beam diameter (full width at half maximum) was 100 nm. Patterns of the entire ring and the straight waveguides were written in the same field size. After development, 125 nm thick SrF_2 hard masks were formed by vacuum evaporation and lift-off process. Patterns were then transferred to the semiconductor layer by RIE using CH_4-H_2 and CF_4-H_2 gas alternatively. CF_4/H_2 gas was used to reduce the amount of contaminated polymer deposited on the top of the SrF_2 mask

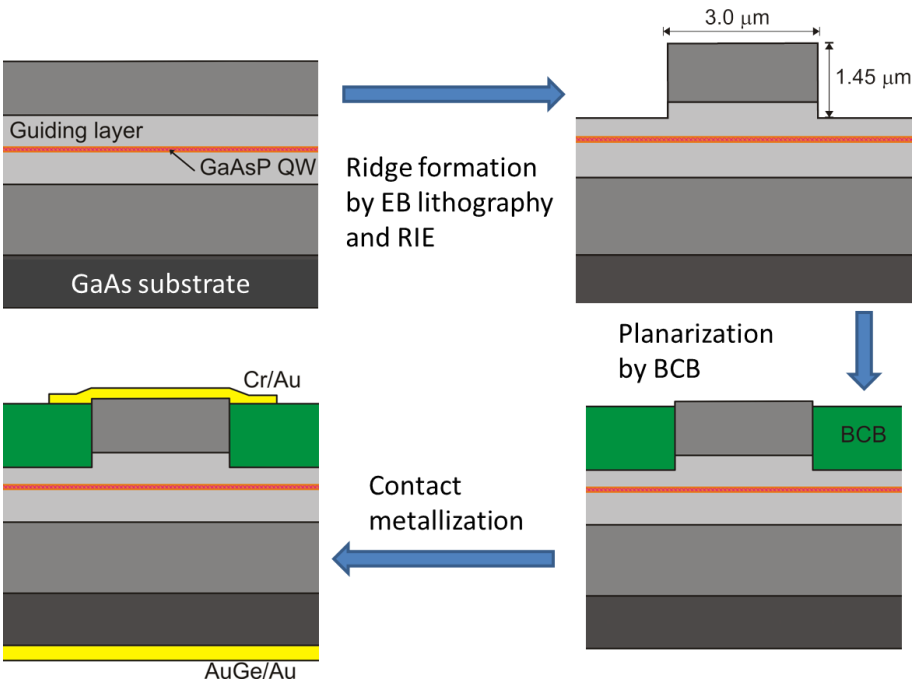

Figure 4.3 Schematic of the RFP laser fabrication process.

during the RIE using CH_4/H_2 gas. The RIE conditions and etching time are shown in table 4.1 (a) and (b), respectively. In situ monitoring was done by using a laser probe to have an etching depth of 1.45 μm. After finishing the RIE, remaining polymer was removed by O_2 plasma ashing. Finally, the SrF_2 masks were removed from the top of the active region by immersing the sample into 5% HCl. The scanning electron microscopic (SEM) images of part of the ring and straight waveguides near the coupler region are shown in figure 4.4. Fabricated waveguides have smooth and almost vertical side walls.

Table 4.1 Various conditions for ridge structure formation process.

(a) RIE conditions during ridge structure formation.

Type of gas	CH_4/H_2	CF_4/H_2
Mixing ratio	1:10	9:1
Flow	20 sccm	7 sccm
Gas pressure	0.03 Torr	
RF power	50 W	

(b) Required time of RIE using CH_4/H_2 and CF_4/H_2 gases alternately.

Gas	Time (min)						
CH_4/H_2	30		30		25		13
CF_4/H_2		1.5		1.5		1.5	

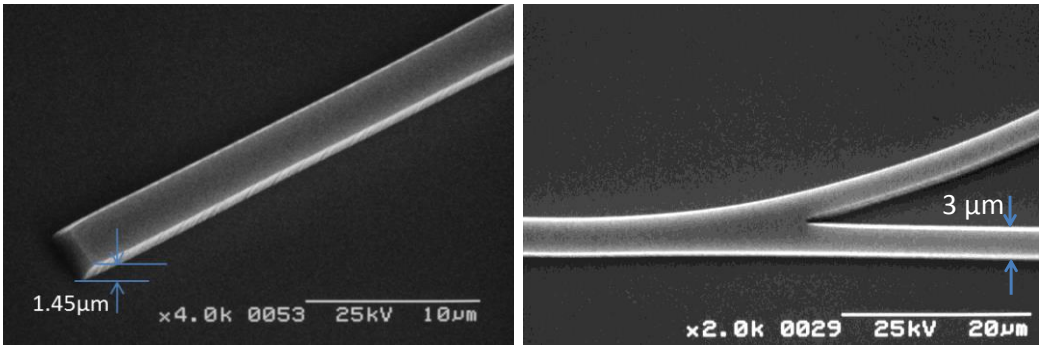

Figure 4.4 SEM images of the fabricated waveguides.

4.3.3 Planarization by BCB layer

Benzocyclobutene (BCB) was used to planarize the entire sample. It also works as an insulating layer for pad electrodes. BCB was spin coated and cured at 250 °C to planarize the entire sample. The top of the ridge structure was opened by reducing the BCB thickness by RIE using CF_4/O_2 gas. The RIE time is very critical because of

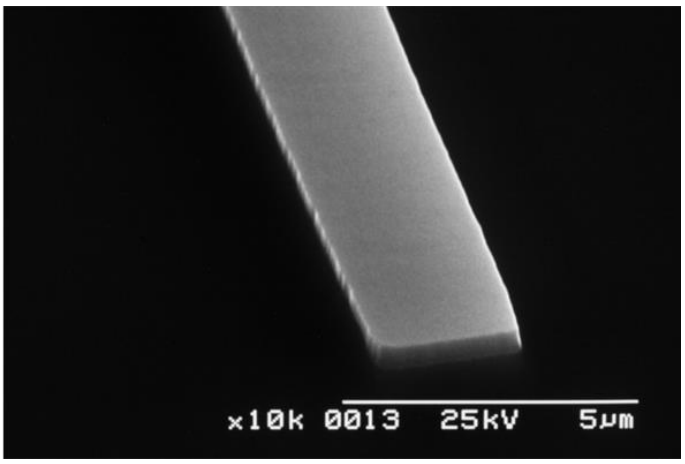

(a)

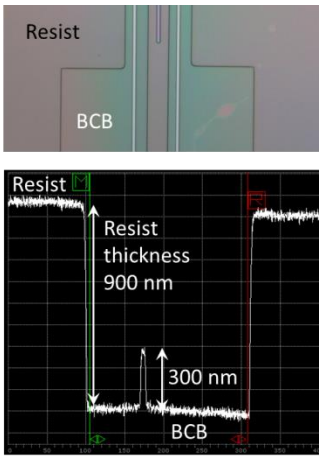

(b)

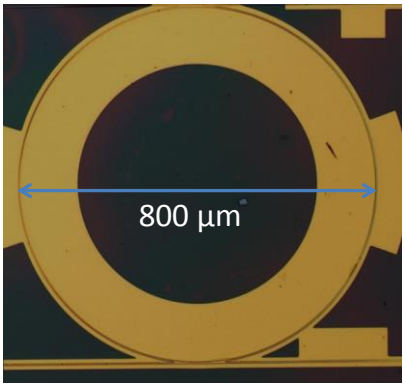

(c)

Figure 4.5 (a) Shows an SEM image of the ridge waveguide buried into BCB layer. (b) Optical microscopic image of the resist mask for electrode formation. Surface profile of the resist mask measured by DEKTAK surface profiler shows the resist thickness and the ridge height above the BCB layer. (c) Optical microscopic image of the fabricated device.

the high etch rate. Time was estimated from the BCB layer thickness determined by using a dummy sample prepared under same condition as the RFP laser chip. Figure 4.5 (a) shows an SEM image of the ridge waveguide buried into BCB layer.

4.3.4 Contact metallization

For the formation of p-side electrodes, at first the ZEP-520A resist mask patterns were prepared by using EB lithography. Figure 4.5 (b) shows an optical microscopic image of the resist mask prepared for electrode formation. Surface profile of the resist mask obtained by DEKTAK surface profiler shows that the resist thickness was 900nm and the ridge height above the BCB layer was 300 nm. By using vacuum deposition technique and lift-off process, 600 nm thick Cr/Au p-electrodes were formed. After reducing the thickness of the substrate to 120 μm, AuGe/Au n-electrode was evaporated on the backside. Figure 4.5(c) shows the optical microscopic image of the fabricated RFP laser. Finally, the wafer was cleaved to form the facet mirrors and the laser was mounted on a Cu heat sink.

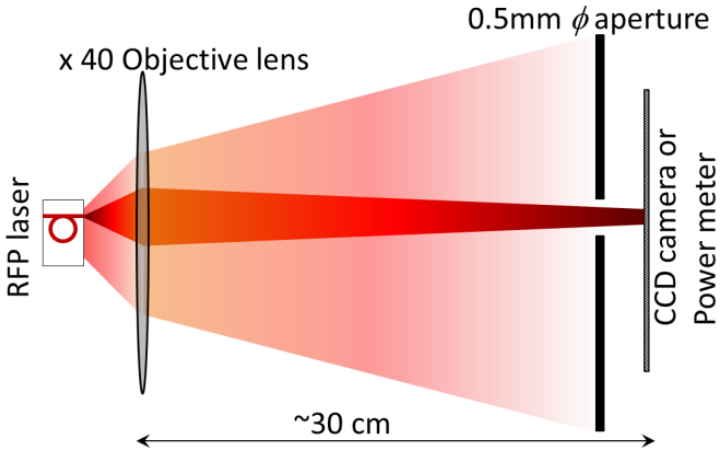

Figure 4.6 Optical setup for measuring the laser light from the output waveguide only.

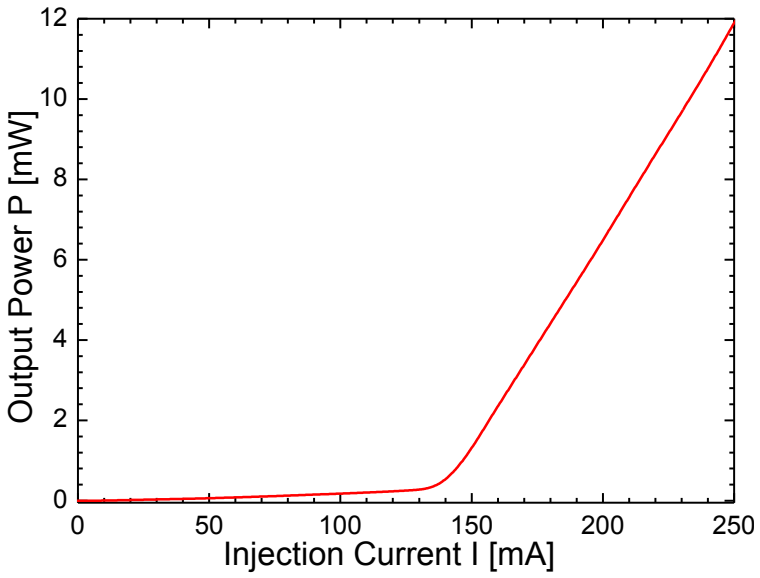

Figure 4.7 P-I characteristics of the RFP laser under CW operation.

4.4 Characterization

4.4.1 P-I characteristics

The laser was then tested under continuous wave operation by controlling the temperature with a thermo-electric cooler at 20 °C. Current was injected to both of the ring and straight waveguides by a single probe placed on the pad electrode inside the ring waveguide. Output power from the straight waveguide facet was measured by placing a circular aperture in front of the power meter head as shown in figure 4.6. This optical arrangement will block the light radiating around the ring waveguide. Figure 4.7 shows the P-I characteristics of the fabricated RFP laser. The threshold current was 140 mA, and an output power of 12 mW was obtained at an injection current of 250 mA.

4.4.2 Lasing spectrum

Lasing spectrum was measured by using an optical spectrum analyzer (Anritsu MS9710B) with a resolution of 0.07nm. Figure 4.8 shows the lasing spectra of the laser obtained at different injection currents. Near the threshold level (~150 mA) the laser showed multimode emission similar to a conventional FP laser. Mode spacing was approximately 0.09 nm. This value is comparable with the ring mode spacing of $|\Delta\lambda_R| = |(\lambda^2/c)\Delta f_R|$ =0.08 nm and the FP mode spacing of $|\Delta\lambda_F| = |(\lambda^2/c)\Delta f_F|$=0.10 nm, calculated by using the effective refractive index n_e =3.22 as an approximation of group effective refractive index n_{eg} into the Eqs. (3.1) and (3.2). For injection currents higher than 180 mA, the laser exhibited single-mode operation, and gradual shift of lasing wavelength to the right was observed with increasing injection current. When the injection current was increased, the junction temperature increased due to joule heating. Due to temperature increase, the effective bandgap energy of the QW material decreased, as a result the gain peak wavelength shifted

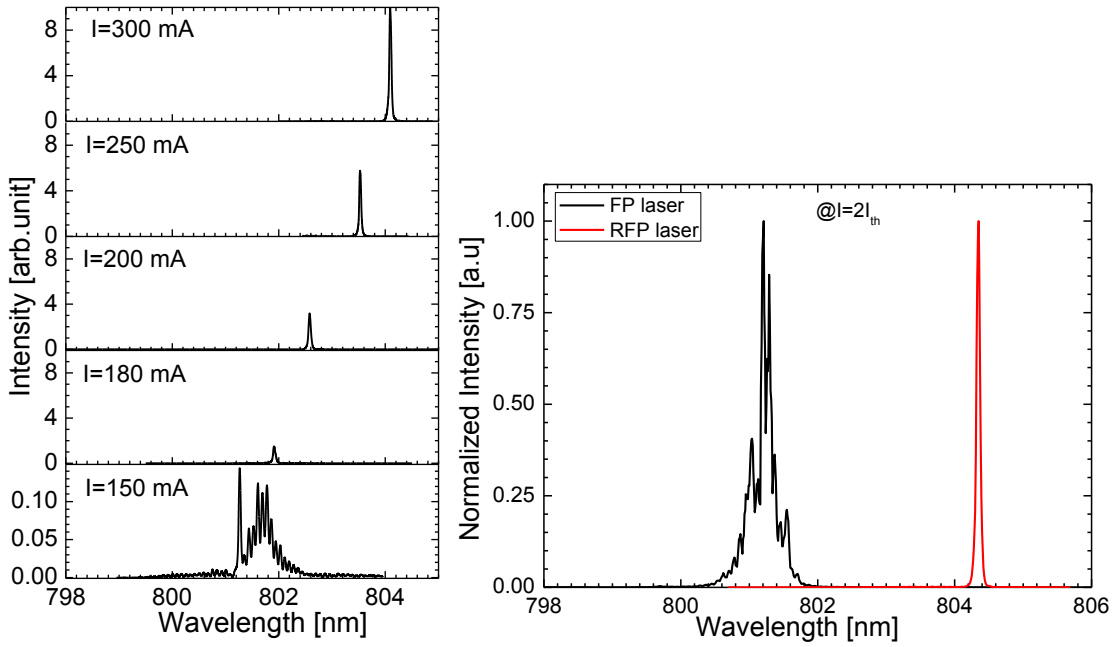

Figure 4.8 (a) Lasing spectra of the RFP laser measured at different injection currents. (b) Lasing spectra of a FP laser (black) and RFP laser (red) measured at I=2I_{th}.

towards the longer wavelength. So that the composite mode at longer wavelength region and close to the gain peak reached its lasing threshold when the injection current increased. As a result the lasing wavelength shifted with the injection current.

Figure 4.8(b) shows the lasing spectra of an ordinary FP laser and the fabricated FRP laser for comparison. Lasing spectrum of the RFP laser clearly

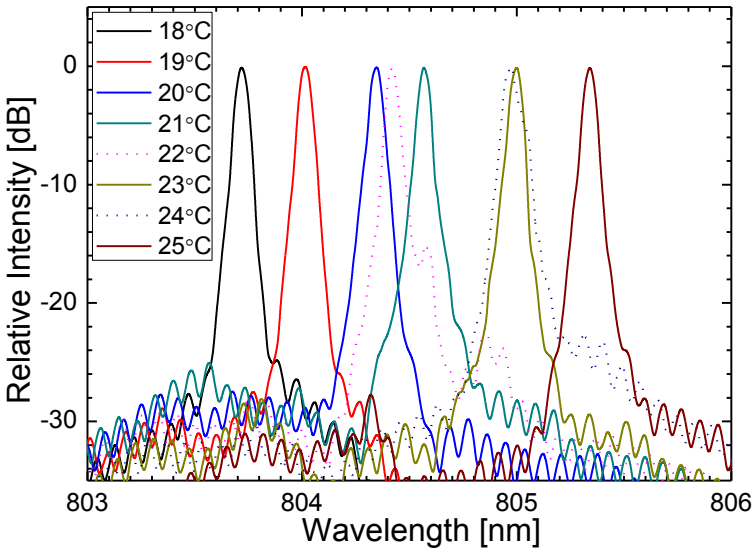

(a)

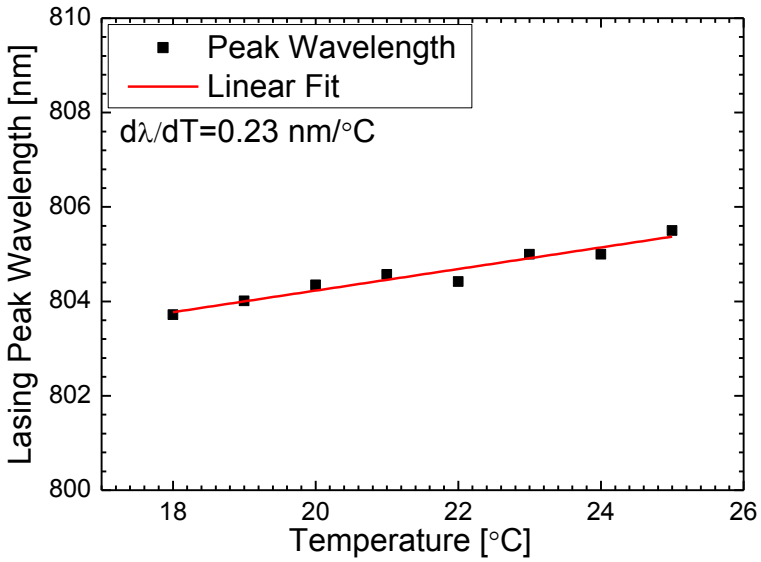

(b)

Figure 4.9 (a) Lasing spectra of the RFP laser measured at different operating temperatures. (b) Temperature dependence of the lasing wavelength of the RFP laser.

shows the single mode operation. Figure 4.9(a) shows the lasing spectra obtained with changing the laser heat sink temperature from 18°C to 25°C with 1°C steps at an injection current of 300 mA. Single-mode operation was accomplished with an SMSR larger than 25 dB. Lasing spectra showed the shift of the peak towards a longer wavelength region. Figure 4.9(b) shows the temperature dependence of the lasing wavelength, and its linear fit gives a slope of 0.23 nm/°C.

The shift of the lasing wavelength could be explained by considering the temperature coefficients of the refractive index of the guiding layer and the bandgap energy of the QW. Schematic illustrations of the RFP modes, the gain curve, and the lasing wavelength shift associated with the temperature change are shown in figure 4.10. At a temperature T_0, lasing occurs at one of the low threshold RFP modes, which is closest to the gain peak. At $T_1 > T_0$, the shift of the RFP cavity modes wavelength is caused by the change of the refractive index. Since the temperature coefficient of the refractive index is same for the ring and FP sections, the temperature coefficient of the RFP cavity mode wavelength is also same as that of the ring mode or FP cavity mode wavelengths. Temperature coefficient of the FP

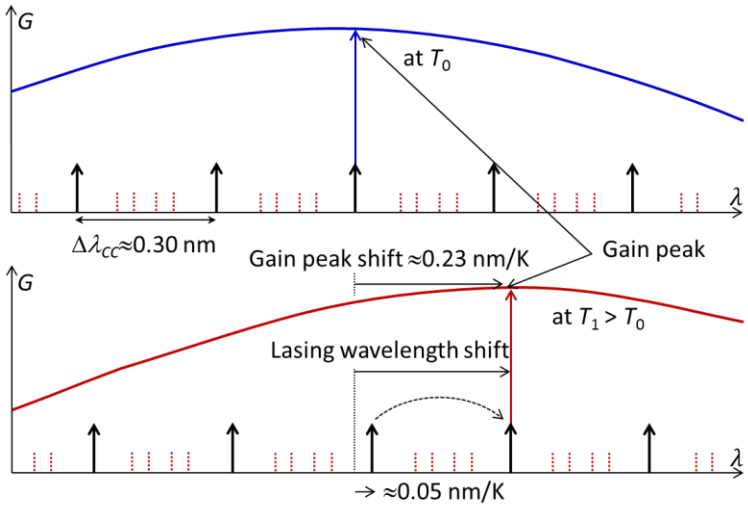

Figure 4.10 Schematic illustrations of the composite modes, gain curve, and lasing wavelength shift due to temperature change.

cavity mode wavelength was derived by differentiating the equation (3.2) with respect to the temperature *T*. Neglecting the thermal expansion of the cavity length, dropping the mode number label (*m'*) and assuming $n_{Fe}=n_e$, the temperature coefficient of the RFP mode wavelength is given by

$$\frac{d\lambda}{dT} = \lambda \frac{1}{n_e}\left(\frac{dn_e}{dT}\right). \tag{4.1}$$

Although the data of dn_e/dT of $Ga_{0.51}In_{0.49}P$ waveguide is not available, a rough estimation can be made by using a relation for the temperature coefficients of the refractive index and the bandgap energy in the long wavelength region

$$\frac{1}{n}\left(\frac{dn}{dT}\right) \sim -\frac{1}{4E_g}\left(\frac{dE_g}{dT}\right), \tag{4.2}$$

based on the Moss's empirical rule [94]. We confirmed the validity of the above approximate relation by using the Kramers-Kronig relation and the analytical expression of frequency dependent absorption coefficient for direct transition semiconductors of bandgap energy E_g. Derivation of the relation between the temperature coefficients of refractive index and bandgap energy is given in the Appendix A.2. The temperature dependence of E_g is expressed in terms of the Varshni formula [94]:

$$E_g(T) = E_g(0) - \frac{\alpha T^2}{\beta + T} \qquad \text{(eV)}, \tag{4.3}$$

where $E_g(0)$ is the bandgap energy at 0 K. Using Eqs. (4.1)–(4.3) with $\alpha = 6.12 \times 10^{-4}$ eV/K [95], $\beta = 204$ K [95], and $E_g = 1.91$ eV [96] at 300 K for $Ga_{0.51}In_{0.49}P$, we obtained $dE_g/dT = -5.12 \times 10^{-4}$ eV/K, $(1/n)(dn/dT) = 6.70 \times 10^{-5}$ /K, and $d\lambda/dT = 0.05$ nm/K. The value of $(1/n)(dn/dT)$ is consistent with 6.51×10^{-5} /K, that was obtained from the temperature dependence of the measured lasing wavelength of a DBR laser [114] fabricated by us using the same epitaxial structure. But, the experimentally obtained temperature coefficient of 0.23 nm/°C for the

lasing wavelength of the RFP laser is different from the value obtained by the above calculation. On the other hand, the gain peak wavelength is approximately given by $\lambda_p(\mu\text{m}) \approx 1.24/E_g(\text{eV})$, and therefore the temperature coefficient can be written as

$$\frac{d\lambda}{dT} \approx -\lambda \frac{1}{E_g}\left(\frac{dE_g}{dT}\right). \tag{4.4}$$

Using Eqs. (4.3) and (4.4) with $\alpha = 5.6 \times 10^{-4}$ eV/K, $\beta = 220$ K, and $E_g = 1.59$ eV [96] at 300 K for the $GaAs_{0.86}P_{0.14}$ QW, we obtained $(1/E_g)(dE_g/dT) = -2.89 \times 10^{-4}$ /K, so that $d\lambda/dT \approx 0.23$ nm/K. Using the Eq. (3.15), an equation for the separation of the low threshold RFP mode wavelengths can be written as $|\Delta\lambda_{CC}| \approx |(\lambda^2/c)\Delta f_{CC}| \approx |\lambda^2/2n_{eg}(\pi R - L)|$. Since the temperature coefficient of the gain peak wavelength is larger than that of the RFP cavity mode wavelength, and $|\Delta\lambda_{CC}| \approx 0.3$ nm is smaller than the gain bandwidth, the lasing wavelength shifts in

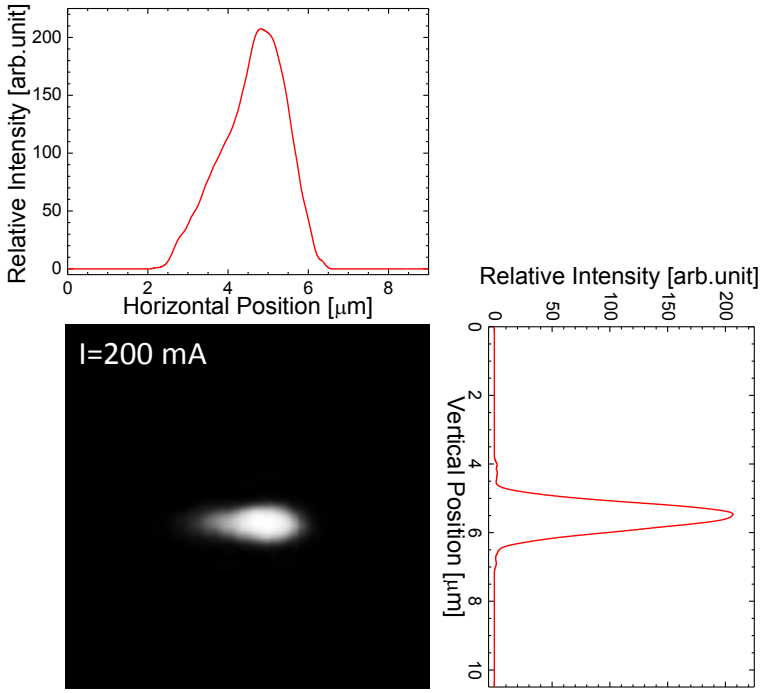

Figure 4.11 Near-field pattern of the RFP laser measured at an injection current of 200 mA. The graphs show the intensity distributions along the horizontal and vertical directions.

steps of $\Delta\lambda_{CC}$ with an average coefficient of 0.23 nm/°C. This value is consistent with the obtained experimental value.

4.4.3 Near field pattern

The near-field pattern (NFP) of the RFP laser was observed by a CCD camera. Figure 4.11 shows the NFP image and its intensity distributions at an injection current of 200 mA. A symmetric intensity distribution along the vertical direction was observed, but there was an asymmetry along the horizontal direction. The possible reason might be that the fabricated waveguide was not exactly of the single-mode but weakly supported the first order mode.

4.5 Summary

I fabricated and characterized a simple all-active circular ring / FP composite cavity semiconductor laser. The laser having a ring radius of 400 μm and an FP cavity length of 950 μm was fabricated. The lasing threshold current was 140 mA and an output power of 12 mW was obtained at an injection current of 250 mA. Stable single-longitudinal-mode lasing with an SMSR higher than 25 dB was accomplished. The temperature coefficient of the lasing wavelength of 0.23 nm/°C was explained by considering the temperature coefficient of the bandgap energy of the QW.

Chapter 5

Two-Wavelength RFP Composite Cavity Lasers

5.1 Introduction

Laser diodes that emit light of multiple wavelengths simultaneously are useful for many applications, such as dual-wavelength interferometry [98], [99], optical switching [100] and terahertz (THz) wave generation [101], [102]. Several techniques have been developed to achieve two-wavelength operation of a diode laser system, and they can be classified into two categories: (1) monolithic two-wavelength diode lasers [80], [103]–[107], and (2) diode laser systems based on external-cavity feedback [108]–[111]. The monolithically integrated devices are attractive for their low cost [104], compact size [104], multi-functionality [112], and stable dual-wavelength operation [105], [106]. Periodic phase-shifted gratings [113] and sampled grating distributed Bragg reflectors (DBRs) [114] have been adopted inside the laser cavity for the realization of multi-wavelength sources. The multi-section distributed feedback (DFB) lasers [106], [107] and two DBR lasers

with integrated Y-junction combiner [80], [105] were also used to achieve dual-wavelength operation [80], [113], [114]. Although these techniques used grating structures, the grating fabrication was rather complicated. Hence, the low cost devices with simple fabrication process are still required. Semiconductor ring lasers require relatively simple fabrication process [56], [88], [89], [91] as compared to the grating incorporated lasers. Devices having various configurations were studied to control the lasing of one of the two counter propagating modes [91] as well as the enhancement of light out coupling from the ring cavity [56].

In this chapter, fabrication and experimental results of a simple circular ring / FP (RFP) composite cavity semiconductor laser for two-wavelength emission is presented. The entire waveguiding structure was fabricated by a single etching step. Two-wavelength lasing of almost equal power under continuous wave operation was accomplished by controlling the currents injection to the FP section and the ring section independently.

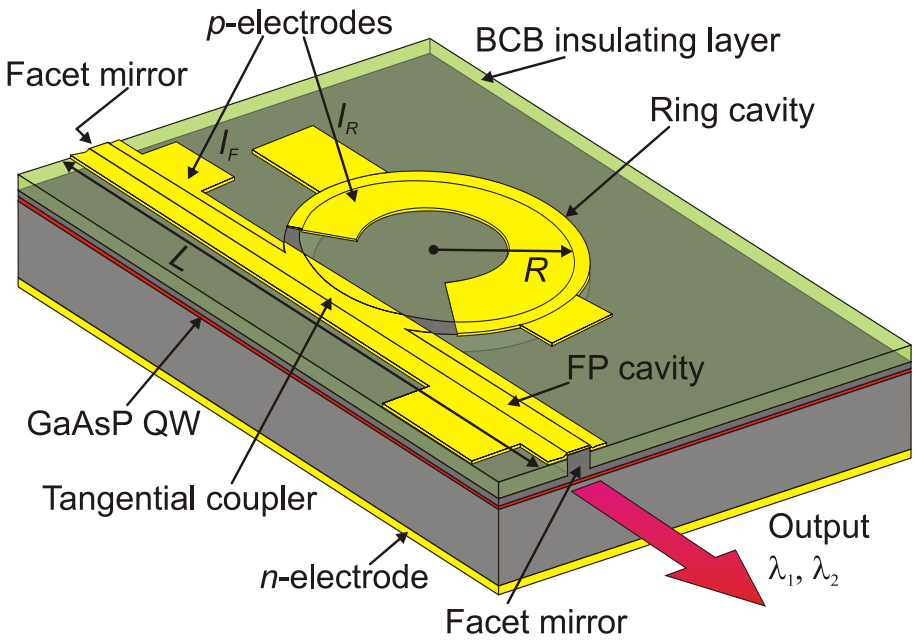

Figure 5.1 Schematic of the ring / Fabry-Perot composite cavity laser with two separate electrodes.

5.2 Design parameters

Figure 5.1 shows the schematic of the RFP laser geometry consisting of an active circular ring resonator coupled to an active straight channel waveguide by a tangential coupler. The ring radius is R and the straight channel length is L. Ridge type single mode waveguides with same width are used for both of the ring and straight waveguides. Two separate p-electrodes are used to control the injection currents to the ring section (I_R) and straight section (I_F) independently. The device is easy to fabricate since it does not require narrow gap between waveguides. We designed a ridge channel waveguide using $GaAs_{0.86}P_{0.14}$ tensile strained single-quantum-well separate confinement heterostructure (SQW-SCH). We expect lasing of TM mode of higher gain at wavelength ~800 nm. The ridge width and height were determined as 3.0 μm and 1.55 μm. The ring radius was determined as R=395 μm. Use of 1.55 μm ridge height gives better lateral confinement of guided mode as compared to previous 1.45 μm ridge height. The bend loss factor calculated for TM fundamental mode was 0.5 cm^{-1}, which can be compensated by the gain available at the active ring waveguide. Analysis of the tangential coupler based on the 2-dimensional BPM simulation showed that, for input wave from the straight (ring) guide, the power efficiencies of coupling to the ring (straight) guide and transmission through the straight (ring) guide are 10% and 82% (30% and 37%), respectively. The FP cavity length was selected as L=1090 μm to satisfy $2R<L<\pi R$. According to the analysis presented in the section 3.4, the value of k=8 was calculated by using the Eqs. (3.1), (3.2) and (3.14). Separation between the composite cavity modes with low threshold gain is $\Delta f_{CC} \approx 7\Delta f_F \approx 8\Delta f_R$. Estimation of the shift of f_{Rm} using the experimentally obtained temperature coefficient $\Delta n_{Re}/\Delta T \approx 2\times10^{-4}$ /°C shows that the shift of f_{Rm} larger than $\Delta f_F \approx$ 38GHz can be obtained with $\Delta T \approx 1.65$°C.

5.3 Fabrication of two-wavelength RFP lasers

The designed RFP laser was fabricated using a $GaAs_{0.86}P_{0.14}$ SQW epitaxial structure same as that used for fabricating the single mode RFP laser discussed in the previous chapter. Details of the epitaxial structure were given in the table 3.1. I fabricated the RFP lasers by EB lithography and RIE using CH_4-H_2 and CF_4-H_2 gases with SrF_2 masks. Fabrication processes were almost similar to that describe in the section 4.3. Only differences were the fabrication of straight section of 1250 μm length, fabrication of two separate electrodes and ridge structures of 1.55 μm heights. To fabricate 1250 μm long straight channel and 395 μm radius ring waveguides, EB writing was done with the field size of 1 mm×1 mm. At first, the ring waveguide and 1000 μm long straight channel waveguide patterns of the RFP laser were written. Then the remaining 250μm straight channel pattern for the same laser was defined after moving the sample stage. Repeating these steps, patterns for all of the lasers were written. Stage positioning accuracy of our EB machine is 0.5μm for X and Y directions, which are acceptable for fabricating this device. The lateral mismatch between the straight sections was minimized by adjusting the scan rotation. Since only one stage shift in vertical direction was required for every laser, 1μm overlap between the waveguides was set to avoid the possibility of gap formation. This overlap between the waveguide is shown in the figure 5.2(a). Due to the two times exposure of e-beam at the overlapped region, width of the waveguide became wider than other parts. This change of waveguide width introduces an additional loss of guided power however the loss was very small (<0.5%) for the fabricated waveguide. SEM images of part of the ring and straight waveguides are shown in the figure 5.2(b) and (c). Fabricated waveguides have smooth and almost vertical side walls. After planarizing the entire sample by benzocyclobutene (BCB) insulation layer, Cr/Au p-electrodes and AuGe/Au n-electrode were evaporated. Figure 5.2(d) shows the microscopic image of the RFP laser. The wafer was cleaved to form the facet mirrors and also to make the straight section length of 1090μm. Finally, the lasers were mounted on a Cu heat sink.

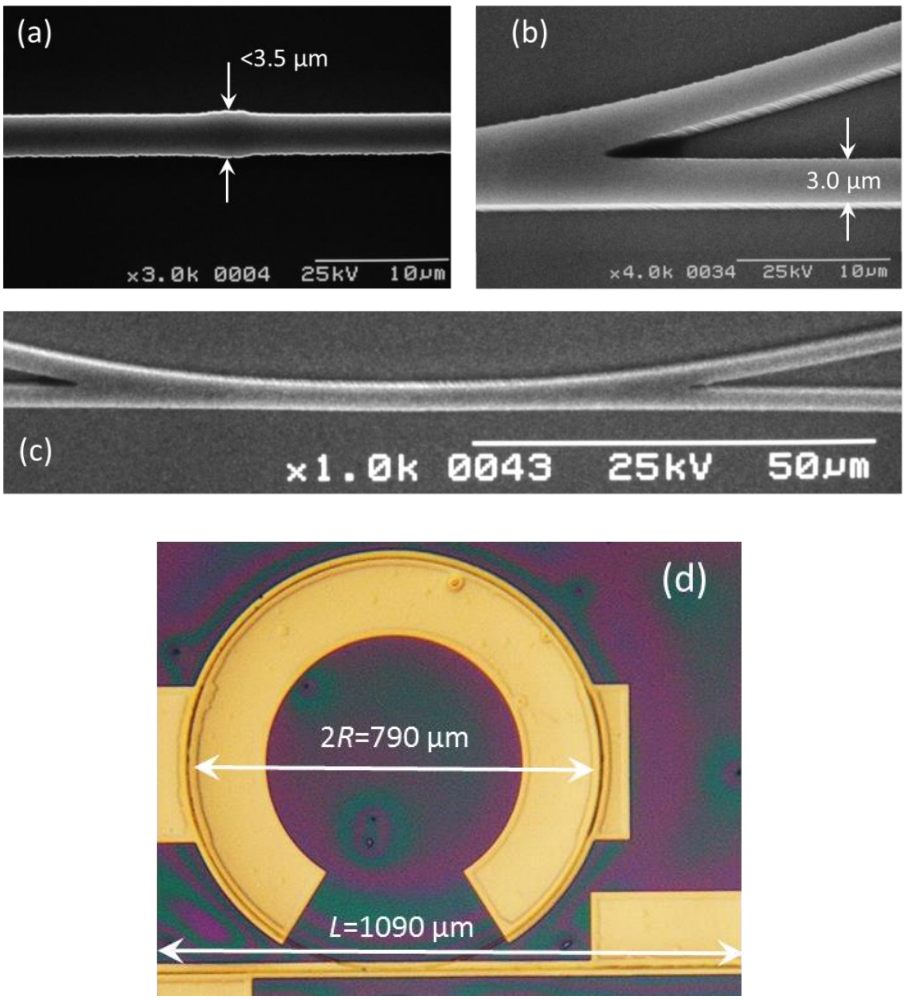

Figure 5.2 (a) SEM image shows the overlapped region on the straight waveguide. (b) and (c) SEM images of the ridge structure around the tangential coupler. (d) Optical microscopic image of the RFP laser.

5.4 Characterization

5.4.1 P-I characteristics

The fabricated RFP laser was then tested under continuous wave operation at 20 °C by using a thermo-electric temperature controller. Currents were injected to the ring and straight waveguide sections by using two probes and two independent current sources. Output power from the straight waveguide facet was measured with a

circular aperture inserted in front of the power meter head to block the radiation from the ring section.

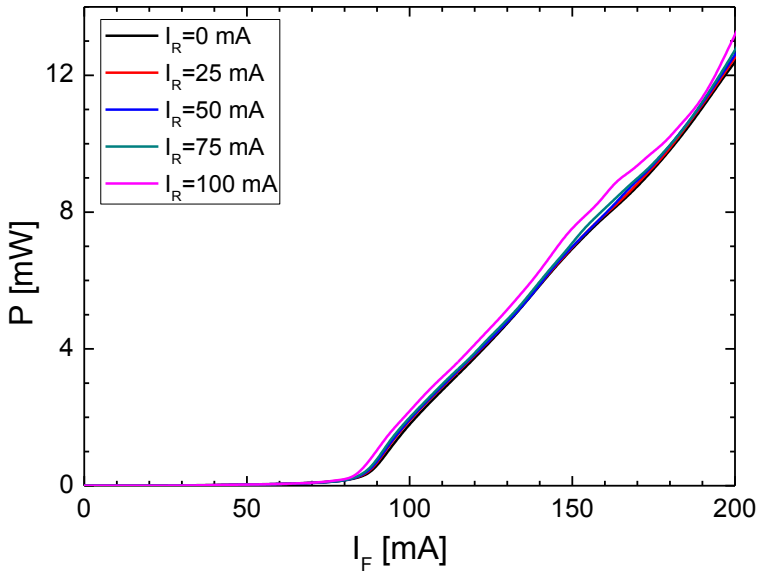

(a)

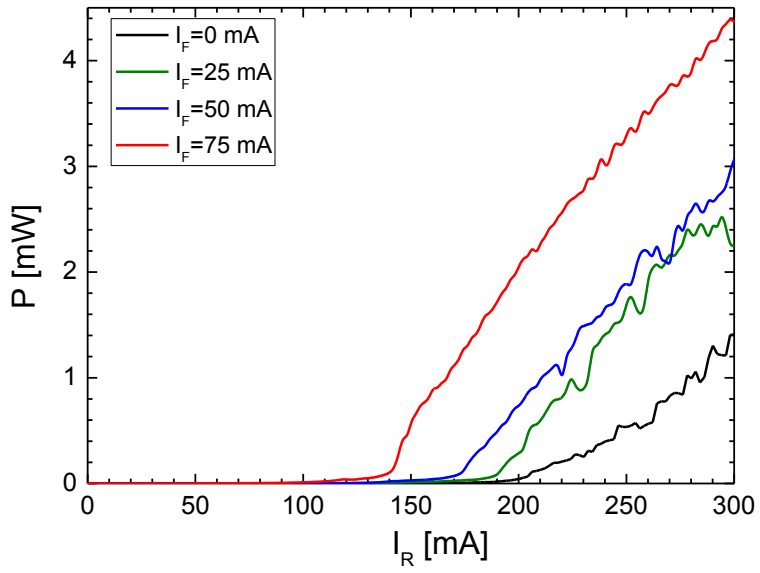

(b)

Figure 5.3 *P-I* characteristics of the RFP laser measured at various fixed injection currents to the (a) ring section and (b) straight section.

Figure 5.3(a) shows the dependence of the output power P on the injection current to the straight section (I_F), obtained for the injection currents to the ring section (I_R) kept at several fixed values. The result shows that the lasing threshold and the output power are not affected significantly by the increase of I_R. Threshold current was I_{Fth}=82 mA, and output power of 13 mW was obtained at I_F=200 mA.

Figure 5.3(b) shows the dependence of the power P on I_R, for I_F at several fixed values. When I_F was increased from 0 mA to 75 mA, the threshold current I_{Rth} decreased from 200 mA to 140 mA and the maximum output power increased from 1.4 mW to 4.4 mW. The reduction of I_{Rth} was due to the reduction of the absorption loss in the part of the ring section close to the coupler region. The increase of the output power was the result of the amplification of the light in the straight waveguide. At present, the exact reason for the irregularities of the P-I_R curves is unknown. However, possible reasons might be interference between the ring and FP modes with the independent injection currents described in the section 3.5, and/or interference between lasing in the fundamental and first-order lateral modes. Although the current spreads from the waveguide with electrodes into the part without electrode, the carrier density is lower there and therefore saturable absorption of light may take place, as the curve for I_F=75 mA in figure 5.3(b) exhibits the evidence of it slightly above the lasing threshold. Such saturable absorption may also be related to the irregularities.

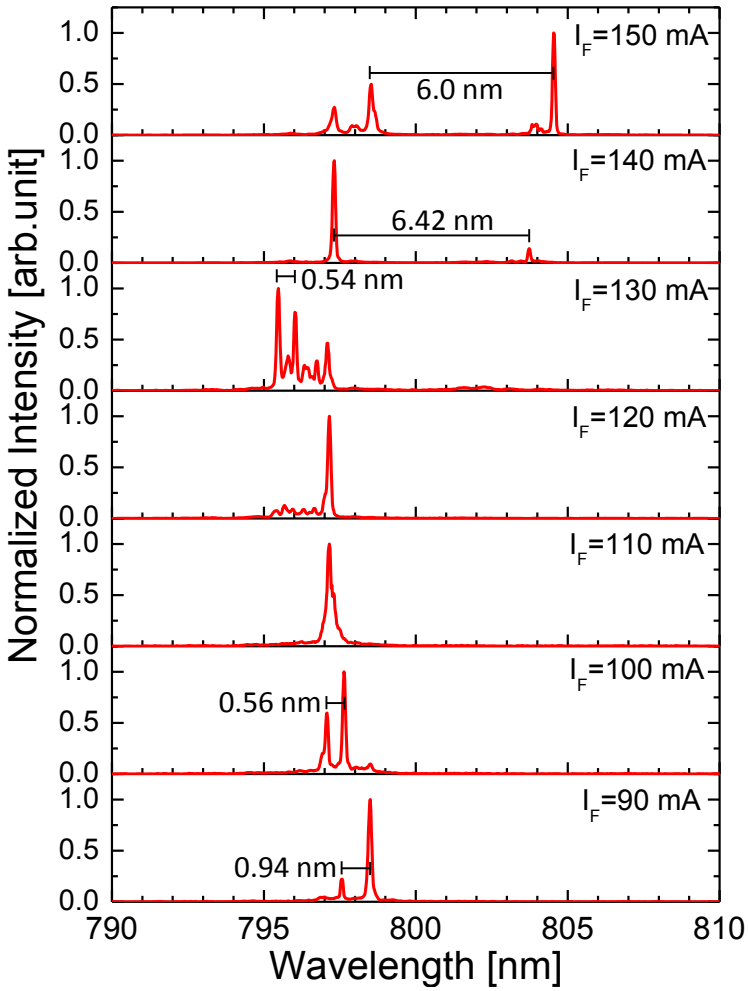

Figure 5.4 Lasing spectra of the RFP laser at different injection currents to the straight section without injection to the ring section.

5.4.2 Lasing spectrum

Lasing spectrum was measured by using an optical spectrum analyzer (Anritsu MS9710B) with a resolution of 0.07 nm. Figure 5.4 shows the lasing spectra obtained for various values of I_F without injection to the ring section. Single or multiple longitudinal mode lasing was observed for different injection currents. The mode spacings for I_F=100 mA and 130 mA were 0.56 nm and 0.54 nm, comparable with $|\Delta\lambda_{CC}|=|(\lambda^2/c)\Delta f_{CC}|\approx 0.59$ nm calculated by using $n_{Reg} = n_{Feg} = 3.624$ for the effective group refractive indices. When I_F was increased from 90 mA to 130 mA,

the lasing wavelength shifted towards the shorter wavelength, although the gain peak shift due to the temperature rise was towards the longer wavelength. For $I_F \geq$ 140 mA, composite modes with wavelength separation around 6 nm lased.

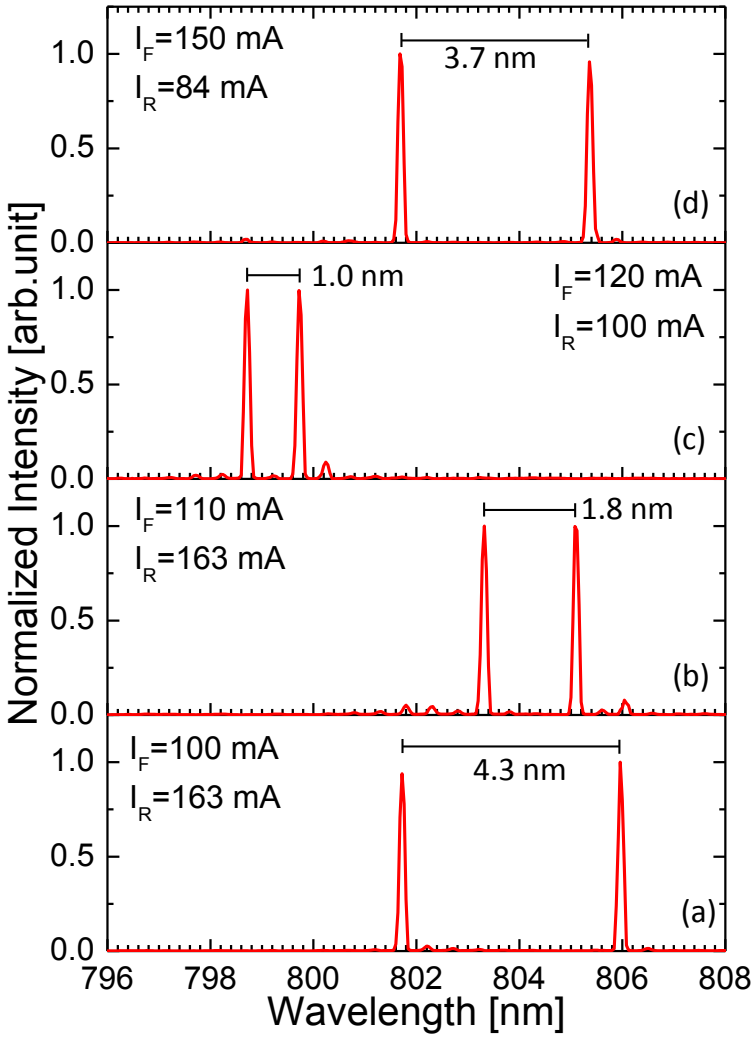

Figure 5.5 Two-wavelength emission spectra of the RFP laser at different combinations of injection currents to the ring and straight sections.

To accomplish two-wavelength lasing, currents were injected to both of the ring and straight waveguides. Keeping I_F at 100 mA higher than the threshold I_{Fth}=82 mA, I_R was increased from 0 mA slowly and carefully observing the lasing spectrum. Initially, multiple peaks of unequal power were observed. With increasing I_R, another peak appeared and grew. Separation between this peak and the main peak of the initial lasing modes was much larger than the initial mode separation of 0.56

nm. Then I_R was fine adjusted so as to have equal intensity for the two lasing wavelengths. Two-wavelength lasing of 4.3 nm separation was obtained at I_F=100 mA and I_R=163 mA as shown in the figure 5.5(a). When I_F was increased to 110 mA with keeping I_R=163 mA, two wavelength lasing of 1.8 nm separation was obtained as shown in figure 5.5(b). Further increase of I_F to 120 mA with I_R=163 mA resulted in disappearance of two-wavelength lasing. When I_R was reduced to 100 mA, two-wavelength lasing with 1.0 nm separation was obtained as shown in figure 5.5(c). When I_F was increased to 150 mA with I_R=100 mA, two wavelength lasing disappeared but readjustment of I_R to 84 mA gave two-wavelength lasing again with 3.7 nm separation as shown in figure 5.5(d). The obtained results are summarized in table 5.1. The wavelength separations are approximately equal to the integer multiple of $|\Delta\lambda_{CC}|$=0.59 nm. As expected by the theoretical considerations described in section 3.5, two-wavelength lasing with discrete sets of separations were accomplished by careful setting of I_F and I_R.

Table 5.1 Summary of driving conditions and obtained two-wavelength lasing performances.

Injection currents I_F, I_R [mA]	Obtained two-wavelength lasing λ_1, λ_2 [nm]	Wavelength separation λ_2-λ_1 [nm]	Total output power [mW]	Power difference [mW]	Beat frequency f_1-f_2 [THz]
100, 163	801.7, 806.0	4.3($\approx 7\Delta\lambda_{CC}$)	3.34	0.11	2.00
110, 163	803.3, 805.1	1.8($\approx 3\Delta\lambda_{CC}$)	4.39	0.0	0.83
120, 100	798.7, 799.7	1.0($\approx 2\Delta\lambda_{CC}$)	4.46	0.0	0.47
150, 84	801.7, 805.4	3.7($\approx 6\Delta\lambda_{CC}$)	7.50	0.16	1.72

5.5 Summary

Fabrication and characterization of a simple all-active circular ring / FP composite cavity GaAsP laser having two separate p-electrodes were presented. Two-wavelength lasing of almost equal power with 3.3~7.5 mW total output power under continuous wave operation was accomplished by keeping the current injection to FP section at a constant value and fine controlling the current injection to the ring section. Discrete sets of wavelength separations in 1.0~4.3 nm in the 800 nm band were obtained. The corresponding beat frequencies in 0.5~2.0 THz are suitable for photomixing generation of THz waves.

Chapter 6

Conclusions

In this dissertation, semiconductor lasers having circular geometry were studied aiming to the applications for beam shaping function and THz wave generation.

In **chapter 2**, I designed and fabricated InGaAs quantum-well circular grating coupled surface emitting lasers (CGCSELs) to focus the emitted laser beam at a spot in air. Third order circular distributed Bragg reflector (DBR) and first order chirped circular grating coupler (GC) were designed by using coupled mode theory. GC was designed for focusing the output beam at 3.0 mm above the laser surface. Stitching error free smooth circular gratings with uniform duty ratio were fabricated by EB lithography and two-step RIE. Single mode lasing was accomplished under pulse operation. Among a group of CGCSELs, the laser having an active region diameter of 240 μm, DBR length of 80 μm, and GC length of 45 μm showed the best performance. Focusing of the surface emitted light at the designed focal plane was confirmed from the emission patterns. The full width at half maximum (FWHM) of the focused spot was measured as around 80 μm.

In **chapter 3**, theoretical analysis and design considerations of novel and simple ring/FP (RFP) composite cavity lasers were presented. The lasing condition was derived by equating the complex round trip gain between the facet mirrors of the RFP laser to unity. Possibilities of single mode and two-wavelength lasing operation were discussed considering the mode frequencies of the ring and FP cavities and vernier effect. Design parameters of the RFP laser were estimated by effective index method, finite element method (FEM) and beam propagation method (BPM) simulation.

In **chapter 4**, fabrication of an RFP composite cavity semiconductor by EB lithography and RIE processes was presented. Single mode lasing with an output power of 12 mW and an SMSR higher than 25 dB was accomplished under continuous wave (CW) operation. Temperature coefficient of lasing wavelength was 0.23 /°C obtained from the measured emission spectra. The shift of the lasing wavelength was explained by considering the temperature coefficient of bandgap energy of the QW material.

In **chapter 5**, accomplishment of two-wavelength lasing of RFP laser with two separate p-electrodes were reported. Lasing of almost equal powers with total output 3.3~7.5 mW under CW operation were accomplished by keeping the current injected into FP section at a constant value and fine controlling the current injected into the ring section. Discrete sets of wavelength separations in 1.0~4.3 nm in the 800 nm band were obtained. The corresponding beat frequencies in 0.5~2.0 THz are suitable for photomixing generation of THz wave.

I have fabricated the CGCSELs by using the unique technique of EB writing employing the smooth circular scanning of e-beam. For the first time, I was able to fabricate the stitching error free circular gratings for such a large size device. This unique fabrication technique would further accelerate the research on this type of lasers. I also demonstrated a novel RFP composite cavity laser, in which ring and FP cavities were coupled to each other by a tangential coupler. Single mode lasing was accomplished under CW operation at room temperature. Simple fabrication process is one of the key advantages of this laser. I also accomplished the two-wavelength lasing with almost equal powers from a single RFP laser for the first time. This device could be a promising candidate for the source of THz wave generation by photomixing process.

There are many avenues for future research arising from this work. Future work involves the following tasks:

1. The output power of the CGCSEL can be enhanced by adopting first-order DBR grating, reducing the absorption loss in the grating region by area selective QW disordering, and reducing mismatch between guided modes in active and DBR regions by inserting a transient region. High power

CGCSEL would be realized by fabricating 2-dimensional array of CGCSELs with a common focus point.

2. Output power of the RFP laser can be enhanced by optimizing the tangential coupler design. The radiation loss of the coupler can be minimized by using single mode waveguides and/or selecting the radius of the ring waveguide carefully.

References

[1] R. N. Hall, G. E. Fenner, J. D. Kingsley, T. J. Soltys, and R. O. Carlson, "Coherent Light Emission From GaAs Junctions," *Phys. Rev. Lett.*, vol. 9, no. 9, pp. 366–368, Nov. 1962.

[2] X. Cai, S. Member, G. Mezosi, M. Sorel, Z. Wang, and Y. Shu, "Output coupling and spectral control in 1550-nm micro-disc lasers using defects on the rim," *IEEE Photonics Technol. Lett.*, vol. 23, no. 21, pp. 1636–1638, Nov. 2011.

[3] P. K. Tien, "Method of forming novel curved-line gratings and their use as reflectors and resonators in integrated optics," *Opt. Lett.*, vol. 1, no. 2, pp. 64–66, Aug. 1977.

[4] S. Kerner and N. Alexopoulos, "On the theory of corrugated optical disk waveguides," in *1978 Antennas and Propagation Society International Symposium*, vol. 16, pp. 315–320, May 1978.

[5] X. H. Zheng and S. Lacroix, "Mode coupling in circular-cylindrical system and its application to fingerprint resonators," *J. Light. Technol.*, vol. 8, no. 10, pp. 1509–1516, Oct. 1990.

[6] C. Wu, T. Makino, J. Glinski, R. Maciejko, and S. I. Najafi, "Self-consistent coupled-wave theory for circular gratings on planar dielectric waveguides," *J. Light. Technol.*, vol. 9, no. 10, pp. 1264–1277, Oct. 1991.

[7] C. Wu, T. Makino, R. Maciejko, S. I. Najafi, and M. Svilans, "Simplified coupled-wave equations for cylindrical waves in circular grating planar waveguides," *J. Light. Technol.*, vol. 10, no. 11, pp. 1575–1589, Nov. 1992.

[8] M. Toda, "Single-mode behavior of a circular grating for potential disk-shaped DFB lasers," *IEEE J. Quantum Electron.*, vol. 26, no. 3, pp. 473–481, Mar. 1990.

[9] T. Erdogan and D. G. Hall, "Circularly symmetric distributed feedback semiconductor laser: an analysis," *J. Appl. Phys.*, vol. 68, no. 4, pp. 1435–1444, Aug. 1990.

[10] T. Erdogan and D. G. Hall, "Circularly symmetric distributed feedback laser: coupled mode treatment of TE vector fields," *IEEE J. Quantum Electron.*, vol. 28, no. 3, pp. 612–623, Mar. 1992.

[11] C. Wu, T. Makino, S. I. Najafi, R. Maciejko, M. Svilans, J. Glinski, and M. Fallahi, "Threshold gain and threshold current analysis of circular grating DFB and DBR lasers," *IEEE J. Quantum Electron.*, vol. 29, no. 10, pp. 2596–2606, Oct. 1993.

[12] T. Makino and C. Wu, “Circular grating DFB and DBR semiconductor lasers: threshold current analysis,” *Opt. Commun.*, vol. 90, no. 4–6, pp. 297–300, Jun. 1992.

[13] C. Wu, M. Svilans, M. Fallahi, T. Makino, J. Glinski, C. Maritan, and C. Blaauw, “Optically pumped surface-emitting DFB GaInAsP/InP lasers with circular grating,” *Electron. Lett.*, vol. 27, no. 20, p. 1819, 1991.

[14] T. Erdogan, O. King, G. W. Wicks, D. G. Hall, C. L. Dennis, and M. J. Rooks, “Spatial modes of a concentric-circle-grating surface-emitting, AlGaAs/GaAs quantum well semiconductor laser,” *Appl. Phys. Lett.*, vol. 60, no. 15, p. 1773, 1992.

[15] T. Erdogan, O. King, G. W. Wicks, D. G. Hall, E. H. Anderson, and M. J. Rooks, “Circularly symmetric operation of a concentric-circle-grating, surface- emitting, AlGaAs/GaAs quantum-well semiconductor laser,” *Appl. Phys. Lett.*, vol. 60, no. 16, p. 1921, 1992.

[16] C. Wu, M. Svilans, T. Makino, J. Glinski, C. Maritan, C. Blaauw, G. Knight, M. Fallahi, I. Templeton, R. Maciejko, and S. I. Najafi, “Room temperature operation of electrically pumped surface-emitting circular grating DBR laser,” *Electron. Lett.*, vol. 28, no. 11, p. 1037, 1992.

[17] C. M. Wu, M. Svilans, M. Fallahi, I. Templeton, T. Makino, J. Glinski, R. Maciejko, S. I. Najafi, C. Blaauw, C. Maritan, and D. G. Knight, “Electrically pumped circular-grating distributed-Bragg-reflector lasers,” *IEEE Photonics Technol. Lett.*, vol. 4, no. 9, pp. 960–963, Sep. 1992.

[18] M. Fallahi, M. Dion, F. Chatenoud, I. M. Templeton, K. A. McGreer, G. Champion, and R. Barber, “Low divergence electrically pumped circular-grating surface-emitting DBR laser on an InGaAs/GaAs structure,” *Electron. Lett.*, vol. 29, no. 16, p. 1412, 1993.

[19] M. Fallahi, F. Chatenoud, M. Dion, I. Templeton, R. Barber, and J. Thompson, “Circular-grating surface-emitting distributed Bragg reflector lasers on an InGaAs-GaAs structure for 0.48-μm applications,” *IEEE J. Sel. Top. Quantum Electron.*, vol. 1, no. 2, pp. 382–386, Jun. 1995.

[20] S. Kristjansson, N. Eriksson, M. Hagberg, K.-J. Killius, and A. Larsson, “Circular grating coupled DBR laser with integrated focusing outcoupler,” *IEEE Photonics Technol. Lett.*, vol. 9, no. 4, pp. 416–418, Apr. 1997.

[21] S. Kristjansson, N. Eriksson, S. J. Sheard, and A. Larsson, “Circular grating-coupled surface-emitter with high-quality focused output beam,” *IEEE Photonics Technol. Lett.*, vol. 11, no. 5, pp. 497–499, May 1999.

[22] S. Kristjansson, N. Eriksson, and A. Larsson, "Optical field analysis of a circular grating-coupled surface-emitting laser with integrated focusing outcoupler," *IEEE J. Quantum Electron.*, vol. 34, no. 5, pp. 834–840, May 1998.

[23] X. F. Li and S. F. Yu, "Multiple-mode behavior of circular-grating-coupled distributed feedback lasers," *J. Light. Technol.*, vol. 26, no. 19, pp. 3345–3354, Oct. 2008.

[24] X. F. Li, S. F. Yu, and S. Member, "Static and dynamic modeling of circular grating-coupled distributed feedback lasers," *IEEE J. Quantum Electron.*, vol. 44, no. 8, pp. 770–776, Aug. 2008.

[25] X. Sun and A. Yariv, "Surface-emitting circular DFB, disk- and ring- Bragg resonator lasers with chirped gratings: a unified theory and comparative study," *Opt. Express*, vol. 16, no. 12, pp. 9155–9164, Jun. 2008.

[26] X. F. Li and S. F. Yu, "Modal characteristics of terahertz surface-emitting distributed-feedback lasers with a second-order concentric-circular metal grating," *J. Appl. Phys.*, vol. 106, no. 5, p. 053103, Sep. 2009.

[27] Xiaofeng Li and Siu Fung Yu, "Diffraction characteristics of concentric circular metal grating operating at terahertz regime," *IEEE J. Quantum Electron.*, vol. 46, no. 6, pp. 898–905, Jun. 2010.

[28] S. Schönenberger, N. Moll, T. Stöferle, R. F. Mahrt, B. J. Offrein, S. Götzinger, V. Sandoghdar, J. Bolten, T. Wahlbrink, T. Plötzing, M. Waldow, and M. Först, "Circular grating resonators as small mode-volume microcavities for switching," *Opt. Express*, vol. 17, no. 8, pp. 5953-5964, Mar. 2009.

[29] N. Matsumoto and K. Kumabe, "AlGaAs–GaAs semiconductor ring laser," *Jpn. J. Appl. Phys.*, vol. 16, no. 8, pp. 1395–1398, Aug. 1977.

[30] T. Krauss, P. J. R. Laybourn, and J. Roberts, "CW operation of semiconductor ring lasers," *Electron. Lett.*, vol. 26, no. 25, p. 2095, Dec. 1990.

[31] J. P. Hohimer, G. A. Vawter, D. C. Craft, and G. R. Hadley, "Interferometric ring diode lasers," *Appl. Phys. Lett.*, vol. 61, no. 12, p. 1375, 1992.

[32] J. P. Hohimer and G. A. Vawter, "Unidirectional semiconductor ring lasers with racetrack cavities," *Appl. Phys. Lett.*, vol. 63, no. 18, p. 2457, 1993.

[33] G. Griffel, J. H. Abeles, R. J. Menna, A. M. Braun, J. C. Connolly, and M. King, "Low-threshold InGaAsP ring lasers fabricated using bi-level dry etching," *IEEE Photonics Technol. Lett.*, vol. 12, no. 2, pp. 146–148, Feb. 2000.

[34] A. Behfar-Rad, J. M. Ballantyne, and S. S. Wong, "AlGaAs/GaAs-based triangular-shaped ring ridge lasers," *Appl. Phys. Lett.*, vol. 60, no. 14, p. 1658, 1992.

[35] C. Ji, M. H. Leary, and J. M. Ballantyne, "Long-wavelength triangular ring laser," *IEEE Photonics Technol. Lett.*, vol. 9, no. 11, pp. 1469–1471, Nov. 1997.

[36] A. S.-H. Liao and S. Wang, "Half-ring (GaAl)As double-heterojunction injection lasers," *Appl. Phys. Lett.*, vol. 36, no. 5, p. 353, 1980.

[37] A. S.-H. Liao and S. Wang, "Semiconductor injection lasers with a circular resonator," *Appl. Phys. Lett.*, vol. 36, no. 10, p. 801, 1980.

[38] T. Krauss, R. M. DeLaRue, I. Gontijo, P. J. R. Laybourn, and J. S. Roberts, "Strip-loaded semiconductor ring lasers employing multimode interference output couplers," *Appl. Phys. Lett.*, vol. 64, no. 21, p. 2788, 1994.

[39] T. F. Krauss, R. M. De La Rue, and P. J. R. Laybourn, "Impact of output coupler configuration on operating characteristics of semiconductor ring lasers," *J. Light. Technol.*, vol. 13, no. 7, pp. 1500–1507, Jul. 1995.

[40] T. F. Krauss, R. M. DeLaRue, P. J. R. Laybourn, B. Vogele, and C. R. Stanley, "Efficient semiconductor ring lasers made by a simple self-aligned fabrication process," *IEEE J. Sel. Top. Quantum Electron.*, vol. 1, no. 2, pp. 757–761, Jun. 1995.

[41] J. P. Hohimer, D. C. Craft, G. R. Hadley, G. A. Vawter, and M. E. Warren, "Single-frequency continuous-wave operation of ring resonator diode lasers," *Appl. Phys. Lett.*, vol. 59, no. 26, p. 3360, 1991.

[42] J. P. Hohimer, G. R. Hadley, and G. A. Vawter, "Semiconductor ring lasers with reflection output couplers," *Appl. Phys. Lett.*, vol. 63, no. 3, p. 278, 1993.

[43] J. P. Hohimer, G. A. Vawter, D. C. Craft, and G. R. Hadley, "Improving the performance of semiconductor ring lasers by controlled reflection feedback," *Appl. Phys. Lett.*, vol. 61, no. 9, p. 1013, 1992.

[44] M. Sorel, P. J. R. Laybourn, A. Scirè, S. Balle, G. Giuliani, R. Miglierina, and S. Donati, "Alternate oscillations in semiconductor ring lasers," *Opt. Lett.*, vol. 27, no. 22, pp. 1992–1994, Nov. 2002.

[45] M. Sorel, P. J. R. Laybourn, G. Giuliani, and S. Donati, "Unidirectional bistability in semiconductor waveguide ring lasers," *Appl. Phys. Lett.*, vol. 80, no. 17, p. 3051, 2002.

[46] M. Sorel, G. Giuliani, A. Scire, R. Miglierina, S. Donati, and P. J. R. Laybourn, "Operating regimes of gaas-algaas semiconductor ring lasers: experiment and model," *IEEE J. Quantum Electron.*, vol. 39, no. 10, pp. 1187–1195, Oct. 2003.

[47] M. T. Hill, H. J. S. Dorren, T. De Vries, X. J. M. Leijtens, J. H. Den Besten, B. Smalbrugge, Y.-S. Oei, H. Binsma, G.-D. Khoe, and M. K. Smit, "A fast low-

power optical memory based on coupled micro-ring lasers," *Nature*, vol. 432, no. 7014, pp. 206–209, Nov. 2004.

[48] A. Trita, G. Mezõsi, M. Sorel, and G. Giuliani, "All-Optical Toggle Flip-Flop Based on Monolithic Semiconductor Ring Laser," *IEEE Photonics Technol. Lett.*, vol. 26, no. 1, pp. 96–99, Jan. 2014.

[49] B. Li, S. Member, M. I. Memon, G. Mezosi, Z. Wang, M. Sorel, S. Yu, and A. All-optical, "Characterization of All-Optical Regeneration Potentials of a Bistable Semiconductor Ring Laser," *J. Light. Technol.*, vol. 27, no. 19, pp. 4233–4240, Oct. 2009.

[50] J. H. Den Besten, R. G. Broeke, M. Van Geemert, J. J. M. Binsma, F. Heinrichsdorff, T. Van Dongen, and T. De Vries, "A compact digitally tunable seven-channel ring laser," *IEEE Photonics Technol. Lett.*, vol. 14, no. 6, pp. 753–755, Jun. 2002.

[51] E. A. J. M. Bente, Y. Barbarin, J. H. den Besten, M. K. Smit, and J. J. M. Binsma, "Wavelength selection in an integrated multiwavelength ring laser," *IEEE J. Quantum Electron.*, vol. 40, no. 9, pp. 1208–1216, Sep. 2004.

[52] L. Bach, J. P. Reithmaier, a. Forchel, J. L. Gentner, and L. Goldstein, "Wavelength stabilized single-mode lasers by coupled micro-square resonators," *IEEE Photonics Technol. Lett.*, vol. 15, no. 3, pp. 377–379, Mar. 2003.

[53] L. Wu, Y. Wang, T. Yu, L. Wang, and J. J. He, "Wavelength switchable semiconductor laser based on half-wave coupled fabry-perot and rectangular ring resonators," *IEEE Photonics Technol. Lett.*, vol. 24, no. 12, pp. 991–993, Jun. 2012.

[54] L. Wu, Z. Hu, J.-J. Meng, and J.-J. He, "Widely tunable semiconductor laser based on double half-wave-coupled rectangular ring resonators," *Asia Commun. Photonics Conf. 2013*, p. AF1B.2, 2013.

[55] J. W. Wu, B. Nakarmi, T. Q. Hoai, and Y. H. Won, "Tunable two-color lasing emission based on fabry-perot laser diode combined with external cavity feedback," *IEEE Photonics J.*, vol. 5, no. 1, p. 1500108, 2013.

[56] L. Wu, Z. Hu, X. Liao, and J.-J. He, "Half-wave coupled ring-FP laser with 50-channel 100GHz-spaced wavelength tuning," *IEEE Photonics J.*, vol. 6, no. 4, p. 1501408, 2014.

[57] L. Wu, X. Liao, Z. Hu, and J.-J. He, "Double half-wave-coupled rectangular ring-FP laser with 35x100GHz wavelength tuning," *IEEE Photonics Technol. Lett.*, vol. 27, no. 10, pp. 1076–1079, May 2015.

[58] O. King, "Curved grating fabrication techniques for surface-emitting distributed feedback lasers," *J. Vac. Sci. Technol. B Microelectron. Nanom. Struct.*, vol. 10, no. 6, p. 2974, 1992.

[59] S. Kristjansson, N. Eriksson, A. Larsson, R. S. Penner, and M. Fallahi, "Observation of stable cylindrical modes in electrically pumped circular grating-coupled surface-emitting lasers," *Appl. Opt.*, vol. 39, no. 1651, pp. 1946–1953, Apr. 2000.

[60] M. Fallahi, M. Dion, F. Chatenoud, I. M. Templeton, and R. Barber, "High power emission from strained DQW circular-grating surface-emitting DBR lasers," *Electron. Lett.*, vol. 29, no. 24, p. 2117, 1993.

[61] M. Fallahi, N. Peyghambarian, K. Kasunic, M. Dion, and Z. Wasilewski, "Circular-grating surface-emitting DBR laser array for free-space applications," *Electron. Lett.*, vol. 32, no. 17, p. 1583, 1996.

[62] P. Modh, J. Backlund, J. Bengtsson, A. Larsson, N. Shimada, and T. Suhara, "Multifunctional gratings for surface-emitting lasers: design and implementation," *Appl. Opt.*, vol. 42, no. 24, p. 4847, Aug. 2003.

[63] K. Uenishi, M. Uemukai, and T. Suhara, "Rotation-symmetric multispot focusing phase-shifted grating coupler for integrated semiconductor laser," *Jpn. J. Appl. Phys.*, vol. 51, no. 5R, p. 058001, Apr. 2012.

[64] A. Yariv and M. Nakamura, "Periodic structures for integrated optics," *IEEE J. Quantum Electron.*, vol. 13, no. 4, pp. 233–253, Apr. 1977.

[65] H. Nishihara, M. Haruna, and T. Suhara, "Optical integrated circuits," Mcgraw-hill optical and electro-optical Engineering Series, 1985.

[66] T. Suhara, "Semiconductor laser fundamentals," Marcel Dekker Inc, 2004.

[67] N. Shimada, Y. Fukumoto, M. Uemukai, T. Suhara, H. Nishihara, and A. Larsson, "Selective disordering of InGaAs strained quantum well by rapid thermal annealing with SiO_2 caps of different thicknesses for photonic integration," *Jpn. J. Appl. Phys.*, vol. 39, no. Part 1, No. 10, pp. 5914–5915, Oct. 2000.

[68] M. Uemukai, M. Miyata, N. Shimada, T. Suhara, H. Nishihara, N. Eriksson, P. Modh, and A. Larsson, "Monolithically integrated master oscillator power amplifier with grating coupler for collimated output beam," *Jpn. J. Appl. Phys.*, vol. 39, no. Part 1, No. 3B, pp. 1503–1507, Mar. 2000.

[69] Y. Sun and X. Fan, "Optical ring resonators for biochemical and chemical sensing," *Anal. Bioanal. Chem.*, vol. 399, no. 1, pp. 205–211, Jan. 2011.

[70] M. Iqbal, M. A. Gleeson, B. Spaugh, F. Tybor, W. G. Gunn, M. Hochberg, T. Baehr-Jones, R. C. Bailey, and L. C. Gunn, "Label-free biosensor arrays based on

silicon ring resonators and high-speed optical scanning instrumentation," *IEEE J. Sel. Top. Quantum Electron.*, vol. 16, no. 3, pp. 654–661, May 2010.

[71] B. E. Little, S. T. Chu, H. A. Haus, J. Foresi, and J.-P. Laine, "Microring resonator channel dropping filters," *J. Light. Technol.*, vol. 15, no. 6, pp. 998–1005, Jun. 1997.

[72] C. J. Kaalund, "Critically coupled ring resonators for add-drop filtering," *Opt. Commun.*, vol. 237, no. 4–6, pp. 357–362, Jul. 2004.

[73] W. M. J. Green, R. K. Lee, G. A. DeRose, A. Scherer, and A. Yariv, "Hybrid InGaAsP-InP mach-zehnder racetrack resonator for thermooptic switching and coupling control," *Opt. Express*, vol. 13, no. 5, p. 1651-1659, Mar. 2005.

[74] T. Segawa, S. Matsuo, T. Kakitsuka, T. Sato, Y. Kondo, and R. Takahashi, "Semiconductor double-ring-resonator-coupled tunable laser for wavelength routing," *IEEE J. Quantum Electron.*, vol. 45, no. 7, pp. 892–899, Jul. 2009.

[75] J. K. Rakshit, J. N. Roy, and T. Chattopadhyay, "All-optical XOR/XNOR logic gate using micro-ring resonators," in *2012 5th International Conference on Computers and Devices for Communication (CODEC)*, pp. 1–4, 2012.

[76] A. Yariv, "Universal relations for coupling of optical power between microresonators and dielectric waveguides," *Electron. Lett.*, vol. 36, no. 4, p. 321, 2000.

[77] J. M. Choi, R. K. Lee, and A. Yariv, "Control of critical coupling in a ring resonator–fiber configuration: application to wavelength-selective switching, modulation, amplification, and oscillation," *Opt. Lett.*, vol. 26, no. 16, p. 1236-1238, Aug. 2001.

[78] Y. Suematsu, "Dynamic Single-Mode Lasers," *J. Light. Technol.*, vol. 32, no. 6, pp. 1144–1158, Mar. 2014.

[79] M. Uemukai, H. Miyamoto, Y. Yamada, Y. Sharma, and T. Suhara, "Integration of surface-emitting red distributed Bragg reflector laser and microfluidic structure for biomolecular sensing," *Jpn. J. Appl. Phys.*, vol. 45, no. 8B, pp. 6738–6741, Aug. 2006.

[80] M. Uemukai, H. Ishida, A. Ito, T. Suhara, H. Kitajima, A. Watanabe, and H. Kan, "Integrated AlGaAs wuantum-well ridge-structure two-wavelength distributed Bragg reflector laser for terahertz wave generation," *Jpn. J. Appl. Phys.*, vol. 51, p. 020205, Feb. 2012.

[81] S. O'Brien and E. P. O'Reilly, "Theory of improved spectral purity in index patterned Fabry-Pérot lasers," *Appl. Phys. Lett.*, vol. 86, no. 20, p. 201101, 2005.

[82] Y. Li, Y. Xi, X. Li, and W.-P. Huang, "Design and analysis of single mode fabry-perot lasers with high speed modulation capability," *Opt. Express*, vol. 19, no. 13, pp. 12131–12140, Jun. 2011.

[83] K. J. Ebeling and L. A. Coldren, "Analysis of multielement semiconductor lasers," *J. Appl. Phys.*, vol. 54, no. 6, p. 2962, 1983.

[84] J. Berger and D. Fekete, "Narrow single stabilized mode operation of coupled-stripe diode lasers," *Appl. Phys. Lett.*, vol. 47, no. 10, p. 1029, 1985.

[85] J. Jin, L. Wang, T. Yu, Y. Wang, and J.-J. He, "Widely wavelength switchable V-coupled-cavity semiconductor laser with ~40 dB side-mode suppression ratio," *Opt. Lett.*, vol. 36, no. 21, pp. 4230–4232, Nov. 2011.

[86] W.-H. Guo, Q. Lu, M. Nawrocka, A. Abdullaev, J. O'Callaghan, and J. F. Donegan, "Nine-channel wavelength tunable single mode laser array based on slots," *Opt. Express*, vol. 21, no. 8, pp. 10215–10221, Apr. 2013.

[87] S. Matsuo and T. Segawa, "Microring-Resonator-Based Widely Tunable Lasers," *IEEE J. Sel. Top. Quantum Electron.*, vol. 15, no. 3, pp. 545–554, May 2009.

[88] D. G. Kim, G.-Y. Oh, H. J. Kim, S. H. Kim, H. C. Ki, S.-T. Kim, H. J. Ko, T. U. Kim, M. H. Yang, H. J. Kim, J. C. Yi, N. Dagli, and Y.-W. Choi, "Bidirectional lasing characteristics of rectangular ring laser with three-guide coupler," *Jpn. J. Appl. Phys.*, vol. 47, no. 12, pp. 8815–8819, Dec. 2008.

[89] W. Coomans, L. Gelens, G. Van der Sande, G. Mezosi, M. Sorel, J. Danckaert, and G. Verschaffelt, "Semiconductor ring lasers coupled by a single waveguide," *Appl. Phys. Lett.*, vol. 100, no. 25, p. 251114, 2012.

[90] L. Gelens, S. Beri, G. Van der Sande, J. Danckaert, N. Calabretta, H. J. S. Dorren, R. Nötzel, E. A. J. M. Bente, and M. K. Smit, "Optical injection in semiconductor ring lasers: backfire dynamics," *Opt. Express*, vol. 16, no. 15, p. 10968-10974, Jul. 2008.

[91] N. J. Withers, H. Cao, G. A. Smolyakov, and M. Osiński, "Highly unidirectional Y-junction-coupled S-section quantum-dot ring lasers," *Appl. Phys. Lett.*, vol. 99, no. 23, p. 231103, 2011.

[92] D. G. Rabus and A. Shakouri, "A GaInAsP-InP double-ring resonator coupled laser," *IEEE Photonics Technol. Lett.*, vol. 17, no. 9, pp. 1770–1772, Sep. 2005.

[93] S. Fürst and M. Sorel, "Cavity-enhanced four-wave mixing in semiconductor ring lasers," *IEEE Photonics Technol. Lett.*, vol. 20, no. 5, pp. 366–368, Mar. 2008.

[94] S. Adachi, "Properties of group-IV, III–V and II–VI semiconductors," Wiley, Chichester, U. K., 2005, p. 120.

[95] M. Levinshtein, S. Rumyantsev, and M. Shur, "Handbook series on semiconductor parameters, " World Scientfic, Singapore, 1999, vol. 2, p. 42.

[96] S. Adachi, "Properties of semiconductor alloys: group-IV, III-V and II-VI semiconductors," Wiley, Chichester, U. K., 2009, p. 155.

[97] M. Uemukai and T. Suhara, "GaAsP tunable distributed Bragg reflector laser with ITO thin-film heater," 20th *Microoptics Conference (MOC'*15*)*, Fukuoka, Japan, Oct. 25-28, 2015.

[98] P. de Groot, "Use of a multimode short-external-cavity laser diode for absolute-distance interferometry," *Appl. Opt.*, vol. 32, no. 22, pp. 4193–4198, 1993.

[99] V. Ménoret, R. Geiger, G. Stern, N. Zahzam, B. Battelier, A. Bresson, A. Landragin, and P. Bouyer, "Dual-wavelength laser source for onboard atom interferometry," *Opt. Lett.*, vol. 36, no. 21, pp. 4128–4130, Nov. 2011.

[100] S. Osborne, P. Heinricht, N. Brandonisio, A. Amann, and S. O'Brien, "Wavelength switching dynamics of two-colour semiconductor lasers with optical injection and feedback," *Semicond. Sci. Technol.*, vol. 27, no. 9, p. 094001, 2012.

[101] M. Tani, P. Gu, M. Hyodo, K. Sakai, and T. Hidaka, "Generation of coherent terahertz radiation by photomixing of dual-mode lasers," *Opt. Quantum Electron.*, vol. 32, no. 4–5, pp. 503–520, 2000.

[102] S. Hoffmann, M. Hofmann, M. Kira, and S. W. Koch, "Two-colour diode lasers for generation of THz radiation," *Semicond. Sci. Technol.*, vol. 20, no. 7, pp. S205–S210, 2005.

[103] A. Klehr, J. Fricke, A. Knauer, G. Erbert, M. Walther, R. Wilk, M. Mikulics, and M. Koch, "High-power monolithic two-mode DFB laser diodes for the generation of THz radiation," *IEEE J. Sel. Top. Quantum Electron.*, vol. 14, no. 2, pp. 289–294, Mar. 2008.

[104] N. Kim, J. Shin, E. Sim, C. W. Lee, D.-S. Yee, M. Y. Jeon, Y. Jang, and K. H. Park, "Monolithic dual-mode distributed feedback semiconductor laser for tunable continuous-wave terahertz generation," *Opt. Express*, vol. 17, no. 16, pp. 13851–13859, 2009.

[105] M. Maiwald, J. Fricke, A. Ginolas, J. Pohl, B. Sumpf, G. Erbert, and G. Tränkle, "Dual-wavelength monolithic Y-branch distributed Bragg reflection diode laser at 671 nm suitable for shifted excitation Raman difference spectroscopy," *Laser Photon. Rev.*, vol. 7, no. 4, pp. L30–L33, Jul. 2013.

[106] C. Zhang, S. Liang, H. Zhu, and W. Wang, "Widely tunable dual-mode distributed feedback laser fabricated by selective area growth technology integrated with Ti heaters," *Opt. Lett.*, vol. 38, no. 16, pp. 3050–3053, Aug. 2013.

[107] I. Kim, C. Kim, G. Li, P. Likamwa, and J. Hong, "180-GHz clock recovery using a multisection gain-coupled distributed feedback laser," *IEEE Photonics Technol. Lett.*, vol. 17, no. 6, pp. 1295–1297, Jun. 2005.

[108] V. Zambon, M. Piché, and N. McCarthy, "Tunable dual-wavelength operation of an external cavity semiconductor laser," *Opt. Commun.*, vol. 264, no. 1, pp. 180–186, Aug. 2006.

[109] I. Park, C. Sydlo, I. Fischer, W. Elsäßer, and H. L. Hartnagel, "Generation and spectroscopic application of tunable continuous-wave terahertz radiation using a dual-mode semiconductor laser," *Meas. Sci. Technol.*, vol. 19, no. 6, p. 065305, 2008.

[110] C. S. Friedrich, C. Brenner, S. Hoffmann, A. Schmitz, I. C. Mayorga, A. Klehr, G. Erbert, and M. R. Hofmann, "New two-color laser concepts for THz generation," *IEEE J. Sel. Top. Quantum Electron.*, vol. 14, no. 2, pp. 270–276, Mar. 2008.

[111] S. A. Zolotovskaya, V. I. Smirnov, G. B. Venus, L. B. Glebov, and E. U. Rafailov, "Two-color output from InGaAs laser with multiplexed reflective Bragg mirror," *IEEE Photonics Technol. Lett.*, vol. 21, no. 15, pp. 1093–1095, Aug. 2009.

[112] O. P. Marshall, M. Khairuzzaman, H. E. Beere, D. A. Ritchie, and S. Chakraborty, "Broadband photonic control for dual-mode terahertz laser emission," *Appl. Phys. Lett.*, vol. 102, no. 18, p. 181106, 2013.

[113] S. Iio, M. Suehiro, T. Hirata, and T. Hidaka, "Two-longitudinal-mode laser diodes," *IEEE Photonics Technol. Lett.*, vol. 7, no. 9, pp. 959–961, Sep. 1995.

[114] Y. Matsui, M. D. Pelusi, S. Arahira, and Y. Ogawa, "Beat frequency generation up to 3.4 THz from simultaneous two-mode lasing operation of sampled-grating DBR laser," *Electron. Lett.*, vol. 35, no. 6, p. 472, 1999.

[115] J. Carroll, J. Whiteaway, and D. Plumb, "Distributed feeback semiconductor lasers," The institute of electrical engineers, London, U. K., 1998, p. 313.

List of Publications and Presentations

1. Journal Papers

[1] **A. K. Saha**, M. Uemukai and T. Suhara, "InGaAs circular-grating-coupled surface emitting laser with focusing function fabricated by electron-beam writing with circular scanning, " Optical Review, vol. 21, no. 3, pp.206-209, June 2014.

[2] **A. K. Saha**, M. Uemukai and T. Suhara, "Single-mode operation of GaAsP ring / Fabry-Perot composite cavity semiconductor lasers," Jpn. J. Appl. Phys., vol. 54, 060302, 2015.

[3] **A. K. Saha** and T. Suhara, "Two-wavelength lasing of ring / Fabry-Perot composite cavity semiconductor laser with two separate electrodes," Jpn. J. Appl. Phys., vol. 54, 070307, 2015.

2. Conference Presentations

[1] **A. K. Saha**, T. Sumitani, M. Uemukai and T. Suhara, "Design and Fabrication of InGaAs Quantum Well Circular-Grating-Coupled Surface Emitting Laser," The 60th Japan Society of Applied Physics (JSAP) Spring Meeting, 29a-B4-9 (2013-03).

[2] **A. K. Saha**, T. Sumitani, M. Uemukai and T. Suhara, "Lasing Characteristic of InGaAs Circular-Grating-Coupled Surface Emitting Laser with Focusing Function," The 61th Japan Society of Applied Physics (JSAP) Spring Meeting, 18p-F9-13 (2014-03).

[3] **A. K. Saha**, M. Uemukai and T. Suhara, "Single-Mode Operation of GaAsP Ring/Fabry-Perot Composite Cavity Semiconductor Lasers," Institute of Electronics, Information and Communication Engineers (IEICE) Technical Report, vol. 114, no. 432, LQE2014-176, pp. 237-240, January 2015.

[4] **A. K. Saha** and T. Suhara, "Demonstration of Two-Wavelength Lasing in a GaAsP Ring/Fabry-Perot Composite Cavity Semiconductor Laser", *accepted for oral presentation in* 2015 International Conference on Solid State Devices and Materials (SSDM 2015), (Sapporo, Hokkaido, Japan).

Appendix

A1. Electron beam writing of circular patterns

The EB writing machine ELS3700S installed in our laboratory has a unique feature called Special Pattern Generator (SPG). In order to enable writing patterns for integrated optics by ELS3700 with high accuracy and high efficiency (high speed), hardware functions for high speed writing are installed to reduce the software dependence. A block diagram of the SPG is shown in figure A1.1.

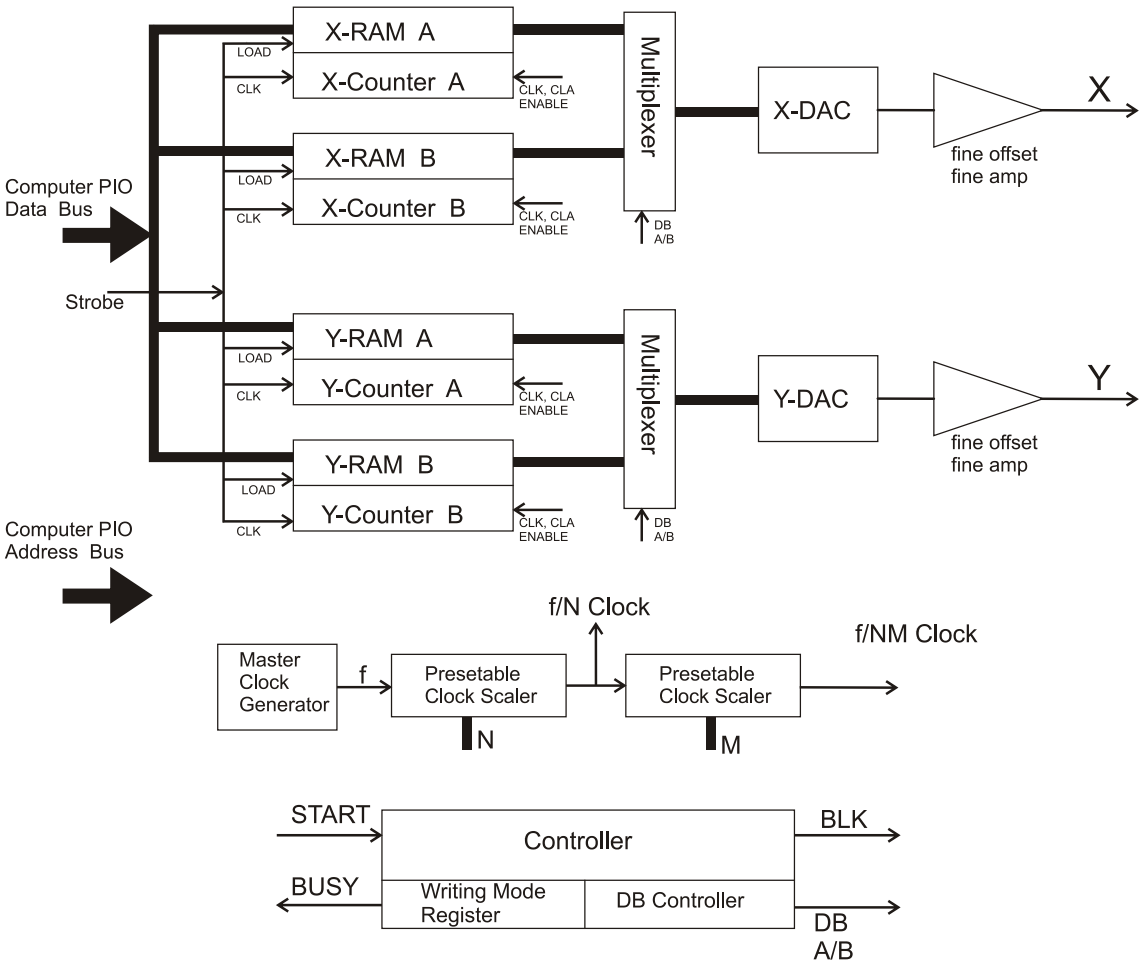

Figure A1.1 Block diagram of the Special Pattern Generator.

SPG has two sets (A and B) of RAM (16 bit $\times 2^{16}$ address) for storing X data and two sets (A and B) of RAM (16 bit $\times 2^{16}$ address) for storing Y data. Both A and B alternately perform acquisition of data from computer PIO and providing the data to Digital to Analog Converter (DAC) for EB writing. This is designated as Double Buffer (DB) scheme. RAMs are associated with 16 bit Address Counter (AC). The combination of AC, RAM and DAC works as a digital arbitrary waveform generator.

SPG has a clock generator, consisting of a master oscillator (frequency f) and two presetable scalers (1/N scaler and 1/M scaler), which provides clock signals of frequencies f/N and f/NM. The f/N clock signal and f/NM clock signal can be connected to X-AC and Y-AC or to Y-AC and X-AC. It is also possible to inhibit the clock for either X-AC or Y-AC. System is designed so that the data from the computer PIO can be loaded in RAM as rapidly as possible. The controller prepares for EB writing by setting the selected writing modes and N, M according to the commands from the computer. The controller also has functions of DB state control and blanking (BLK) control.

SPG can be operated in three writing modes such as: arbitrarily curved line mode, horizontal line mode and vertical line mode. For writing the circular patterns, arbitrarily curved line mode was used. Both of the X and Y blocks work as arbitrary function generators. Operating sequences of this mode is as follows:

1. f/N clock signal is connected as clocks for X-AC and Y-AC.
2. N is preset to determine the scanning speed.
3. Data for one curved line are transferred from the computer to X-RAM and Y-RAM.
4. AC is cleared.
5. The start signal given by the computer turns BUSY to 1, turns BLK to off and AC is enabled. Then writing of the curved line starts. When the address reaches the value corresponding to the number of the data transferred, BLK turns on, AC is disabled and busy is turned to 0. Then writing of the curve is completed.
6. In parallel with the sequence 5, the data for the next curved line are loaded in another RAM.

7. Sequences 3–5 are repeated to write the whole pattern.

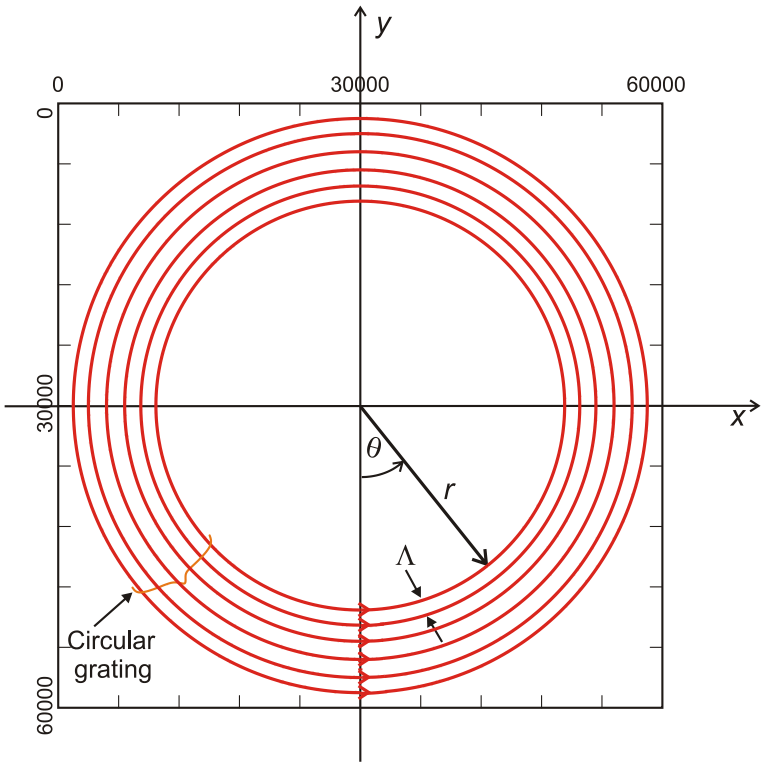

Figure A1.2 Schematic of circular scanning of e-beam for writing the circular grating patterns.

For EB writing under the control of SPG, the field size can be divided into 60000×60000 pixels. The X and Y data for writing a circle of radius r can be calculated by the following equations:

$$X_i = \left[\{r_{max} + r\sin\theta_i\}/s_p\right]_{int}, \quad \text{(A1.1)}$$

$$Y_i = \left[\{r_{max} + r\cos\theta_i\}/s_p\right]_{int}. \quad \text{(A1.2)}$$

Here, $r_{max}$is the maximum radius of a circle in nm that can be defined within the EB writing field size, $i = 0, 1, \ldots n$ is an integer, $n = n_{max}r/r_{max}$ represents the total number of data points require to define the circle of a radius r, $\theta_i = 2\pi i/n$ is the

angular position of the *i*-th point on the circle, $s_p = 100\times10^6$ /(m×60000) is the length of each pixel in nm and m is the magnification.

To fabricate 500μm diameter CGCSELs, magnification was set to 200 to have a writing field size of 500μm×500μm. Size of each of the dots were 8.33 nm at this magnification. Data for a circle of radius *r* were prepared with constant arc lengths of 26 nm. Circular disk like patterns were written by multiple circular scanning of e-beam (diameter 100 nm) with radial steps of 100 nm. For writing the grating patterns, beam current was set at 40 pA so that the beam diameter was 40 nm. Each of the grating patterns were written by a single and constant speed circular scanning of e-beam. Scan speed was predetermined by test writing for obtaining the desired linewidth with. Writing of the entire grating patterns were completed by multiple circular scanning with radial steps determined by the periods of the grating as shown in the figure A1.2. A total of about 350 circles were written for the DBR and GC. For fabricating the gratings with an accurate period, calibration of the EB writing system was done every time by using a calibration mark written with same field size.

A2. Relation between the temperature coefficients of refractive index and bandgap energy

The Kramers-Kronig relations are [1]

$$\mathrm{Re}\{\chi(\omega)\} = \frac{1}{\pi} P \int_{-\infty}^{\infty} \frac{\mathrm{Im}\{\chi(\omega')\}}{\omega' - \omega} d\omega', \tag{A2.1}$$

$$\mathrm{Im}\{\chi(\omega)\} = -\frac{1}{\pi} P \int_{-\infty}^{\infty} \frac{\mathrm{Re}\{\chi(\omega')\}}{\omega' - \omega} d\omega', \tag{A2.2}$$

where $\chi(\omega)$ is the complex dielectric susceptibility which is a function of the angular frequency ω and P denotes the Cauchy principal value. Definition of the Cauchy principal value is given by the right hand side of the Eq. (A2.3).

$$P \int_{-\infty}^{\infty} \frac{\chi(\omega')}{\omega' - \omega} d\omega' = \lim_{\rho \to 0} \left[\int_{-\infty}^{\omega - \rho} \frac{\chi(\omega')}{\omega' - \omega} d\omega' + \int_{\omega + \rho}^{\infty} \frac{\chi(\omega')}{\omega' - \omega} d\omega' \right]. \tag{A2.3}$$

Here, ρ is an infinitely small distance from the pole at $\omega' = \omega$ on the real axis. The Kramers-Kronig relation shows that the real and imaginary parts of $\chi(\omega)$ are not independent to each other but are correlated by integral transformations. Since $\mathrm{Re}\{\chi(\omega)\}$ is even function of ω and $\mathrm{Im}\{\chi(\omega)\}$ is an odd function of ω, the Eq. (A2.1) can be rewritten as

$$\begin{aligned} \mathrm{Re}\{\chi(\omega)\} &= \frac{1}{\pi} P \int_{-\infty}^{\infty} \frac{\mathrm{Im}\{\chi(\omega')\}}{\omega' - \omega} d\omega', \\ &= \frac{2}{\pi} P \int_{0}^{\infty} \frac{\omega' \, \mathrm{Im}\{\chi(\omega')\}}{\omega'^2 - \omega^2} d\omega'. \end{aligned} \tag{A2.4}$$

The complex refractive index is related with the dielectric susceptibility by the following relations:

$$\tilde{n}^2 = \tilde{\varepsilon} = 1 + \chi, \tag{A2.5}$$

$$\left(\frac{n\omega}{c} + \frac{i\alpha}{2}\right)^2 = \left(\frac{\omega}{c}\right)^2 \tilde{\varepsilon} = \left(\frac{\omega}{c}\right)^2 (1 + \chi). \tag{A2.6}$$

Here, n is the real part of the complex refractive index, α is the power attenuation coefficient, c is the free space light velocity. For $\alpha \ll \frac{\omega}{c} = k_0 = \frac{2\pi}{\lambda}$ we can write

$$\begin{cases} n^2 = 1 + \mathrm{Re}\{\chi\}, \\ n\alpha = \left(\frac{\omega}{c}\right) \mathrm{Im}\{\chi\}. \end{cases} \tag{A2.7}$$

Using the Eqs. (A2.6) and (A2.7) we can write the frequency dependence of the refractive index as

$$n^2(\omega) = 1 + \mathrm{Re}\{\chi(\omega)\} = 1 + \frac{2c}{\pi} P \int_0^{\infty} \frac{n(\omega')\alpha(\omega')}{\omega'^2 - \omega^2} d\omega'. \tag{A2.8}$$

From the expression of frequency dependent absorption factor [1] for direct transition type semiconductors without carrier injection we can write

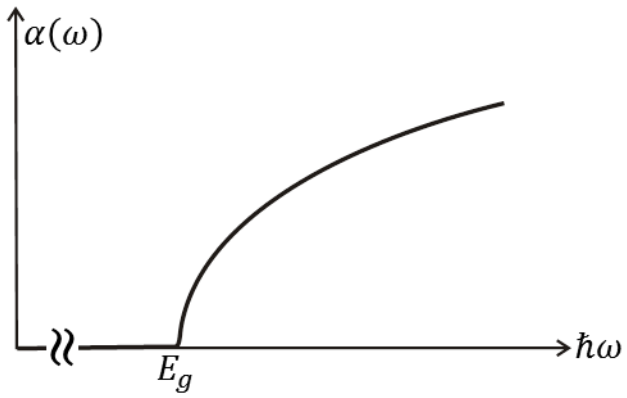

Figure A2.1 Absorption spectrum without carrier injection.

$$n(\omega')\alpha(\omega') \cong \begin{cases} 0 & ;\hbar\omega < E_g, \\ A\sqrt{\hbar\omega' - E_g} & ;\hbar\omega > E_g. \end{cases} \quad \text{(A2.9)}$$

Here, A is the proportionality constant and E_g is the bandgap energy. Substituting the Eq. (A2.9) into Eq. (A2.8) for $\omega < E_g/\hbar$ we obtain

$$n^2(\omega) \cong 1 + \frac{2cA}{\pi}\int_{\frac{E_g}{\hbar}}^{\infty} \frac{\sqrt{\hbar\omega' - E_g}}{\omega'^2 - \omega^2}\, d\omega',$$

$$\cong 1 + \frac{2cA\hbar}{\pi}\int_0^{\infty} \frac{\sqrt{x}}{\left(x + E_g\right)^2 - \hbar^2\omega^2}\, dx. \quad \text{(A2.10)}$$

Result of the integration part at the right hand side of Eq. (A2.10) can be obtained by doing integration by substitution as

$$\int_0^{\infty} \frac{\sqrt{x}}{\left(x + E_g\right)^2 - \hbar^2\omega^2}\, dx = \int_0^{\infty} \frac{2y^2}{\left(y^2 + E_g\right)^2 - \hbar^2\omega^2}\, dy,$$

$$= \frac{1}{\hbar\omega}\int_0^{\infty} \left\{\frac{E_g + \hbar\omega}{y^2 + E_g + \hbar\omega} - \frac{E_g - \hbar\omega}{y^2 + E_g - \hbar\omega}\right\} dy,$$

$$= \frac{1}{\hbar\omega}\left[\int_0^{\frac{\pi}{2}} \frac{\sec^2\theta}{\tan^2\theta + 1}\sqrt{E_g + \hbar\omega}\, d\theta - \int_0^{\frac{\pi}{2}} \frac{\sec^2\theta}{\tan^2\theta + 1}\sqrt{E_g - \hbar\omega}\, d\theta\right],$$

$$= \frac{\pi}{\sqrt{E_g + \hbar\omega} + \sqrt{E_g - \hbar\omega}}. \quad \text{(A2.11)}$$

In the above calculation, $\sqrt{x} = y$ and $y = \sqrt{E_g \pm \hbar\omega}\,\tan\theta$ were used. Using the Eq. (A2.11) in Eq. (A2.10) we obtain

$$n^2(\omega) \cong 1 + 2c\hbar A \frac{1}{\sqrt{E_g + \hbar\omega} + \sqrt{E_g - \hbar\omega}}. \qquad \text{(A2.12)}$$

Taking the derivative of Eq. (A2.12) with respect to temperature *T* and eliminating *A* we obtain the relation between the temperature coefficients of refractive index and the bandgap energy as

$$\frac{1}{n}\frac{dn}{dT} \cong -\frac{1}{4}\frac{1 - \frac{1}{n^2}}{\sqrt{1 - \left(\frac{\hbar\omega}{E_g}\right)^2}}\frac{1}{E_g}\frac{dE_g}{dT}. \qquad \text{(A2.13)}$$

For $\hbar^2\omega^2 \ll E_g^2$, and $n^2 \gg 1$, Eq. (A2.13) reduces to

$$\frac{1}{n}\frac{dn}{dT} \cong -\frac{1}{4}\frac{1}{E_g}\frac{dE_g}{dT}. \qquad \text{(A2.14)}$$

Reference

[1] T. Suhara, "Semiconductor laser fundamentals," Marcel Dekker Inc, 2004.

A3. Conformal mapping of ring waveguide

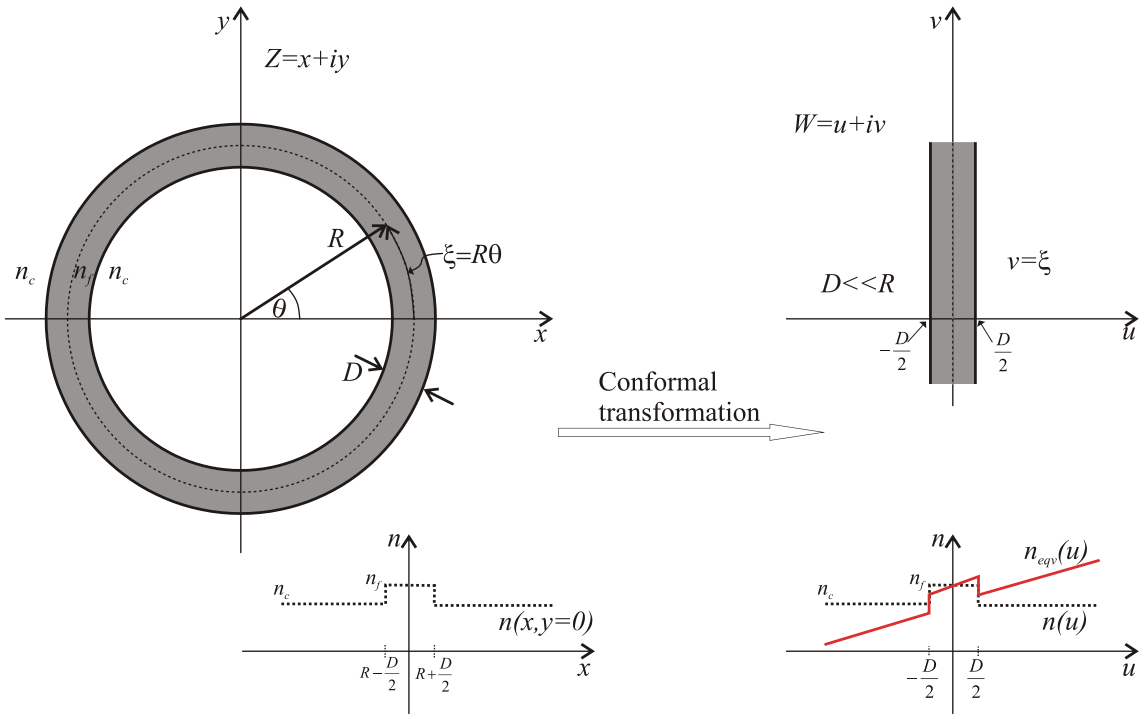

(a) (b)

Figure A3.1 (a) Two-dimensional view of the cylindrical waveguide with radial step index distribution (b) Conformal transformation that converts the ring waveguide into a straight waveguide with a modified lateral refractive index profile.

Figure A3.l(a) shows the cross sectional view of a cylindrical waveguide with a radius *R* and a constant width *D*. Step discontinuity in refractive indices at radii *R*-*D*/2 and *R*+*D*/2 are shown in the lower part of figure. A3.1(a). Wave propagation in this waveguide along the direction perpendicular to the Z plane is described by the solution of two-dimentional wave equation as:

$$\left[\frac{\partial^2}{\partial x^2}+\frac{\partial^2}{\partial y^2}+k^2n^2(x,y)\right]E(x,y)=0. \qquad \text{(A3.1)}$$

Conformal mapping [1],[2] allows for curved waveguides to be represented by corresponding straight waveguides with a modified lateral refractive index distribution. The ring waveguide on *Z*-plane (*x,y* plane) can be converted into equivalent straight waveguide on *W*-plane (*u,v* plane) . The objective of the transformation is to select an *f(Z)* that converts curved boundaries in the (*x,y*) plane to straight ones in the (*u, v*) plane. Using the values and reference planes as shown in figure A3.1(a), this can be accomplished by selecting

$$W = f(Z) = R \ln \frac{Z}{R} \tag{A3.2}$$

and

$$Z = R\, \mathrm{e}^{\frac{W}{R}}. \tag{A3.3}$$

Relations between the *Z*-plane and *W*-plane coordinates are, $x = R\, \mathrm{e}^{\frac{u}{R}} \cos\frac{v}{R}$, $y = R\, \mathrm{e}^{\frac{u}{R}} \sin\frac{v}{R}$ and $u = R\, \ln\sqrt{\frac{x^2+y^2}{R^2}}$, $v = R \tan^{-1}\frac{y}{x} = R\theta = \xi$. Figure A3.1(b) shows the equivalent straight waveguide obtained by using the above conformal transformation. The straight boundaries at $u=-D/2$ and $u=D/2$ are equivalent to the inner and outer boundaries of the ring waveguide. Using the Cauche-Riemann relation [3] ($\frac{\partial u}{\partial x} = \frac{\partial v}{\partial y}$, $\frac{\partial u}{\partial y} = -\frac{\partial v}{\partial x}$ and $\frac{\partial x}{\partial u} = \frac{\partial y}{\partial v}$, $\frac{\partial x}{\partial v} = -\frac{\partial y}{\partial u}$), the $\left(\frac{\partial^2}{\partial x^2} + \frac{\partial^2}{\partial y^2}\right)$ (in *x,y* coordinate system) can be converted (into *u,v* coordinate system) as

$$\frac{\partial^2}{\partial x^2} + \frac{\partial^2}{\partial y^2} = \begin{vmatrix} \frac{\partial u}{\partial x} & \frac{\partial u}{\partial y} \\ \frac{\partial v}{\partial x} & \frac{\partial v}{\partial y} \end{vmatrix} \left(\frac{\partial^2}{\partial u^2} + \frac{\partial^2}{\partial v^2}\right) = \left\{\left(\frac{\partial u}{\partial x}\right)^2 + \left(\frac{\partial u}{\partial y}\right)^2\right\}\left(\frac{\partial^2}{\partial u^2} + \frac{\partial^2}{\partial v^2}\right)$$

$$= \mathrm{e}^{-2\frac{u}{R}}\left(\frac{\partial^2}{\partial u^2} + \frac{\partial^2}{\partial v^2}\right). \tag{A3.4}$$

Cauche-Riemann relation was used to preserve the local angles of ring waveguide and equivalent straight waveguide. Using the Eq. (A3.4), Eq. (A3.1) can be written as

$$\left[\mathrm{e}^{-2\frac{u}{R}}\left(\frac{\partial^2}{\partial u^2}+\frac{\partial^2}{\partial v^2}\right)+k^2n^2(u)\right]E(u,v)=0,$$

$$\left[\frac{\partial^2}{\partial u^2}+\frac{\partial^2}{\partial v^2}+\mathrm{e}^{2\frac{u}{R}}\,k^2n^2(u)\right]E(u,v)=0,$$

$$\left[\frac{\partial^2}{\partial u^2}+\frac{\partial^2}{\partial v^2}+k^2n_{eqv}^2(u)\right]E(u,v)=0\,. \qquad \text{(A3.5)}$$

Here, $n_{eqv}(u)=\mathrm{e}^{\frac{u}{R}}\,n(u)\approx\left(1+\frac{u}{R}\right)n(u)$ is the equivalent refrcactive index distribution of the converted straight waveguide. The approximation is valid only if *R>>D* so that in the vicinity of the waveguide, *R>>u*. Refractive index profile of the equivalent straight waveguide is shown in the lower part of figure A3.1(b).

References

[1] M. Heiblum and J. Harris, "Analysis of curved optical waveguides by conformal transformation," *IEEE J. Quantum Electron.*, vol. 11, no. 2, pp. 75–83, Feb. 1975.

[2] L. A. Coldren, S. W. Corzine, and M. L. Mašanović, "Diode lasers and photonic integrated circuits," (Wiley, New Jersey, 2012) p. 421.

[3] K. F. Riley, M. P. Hobson, and S. J. Bence, "Mathematical methods for physics and engineering," (Cambridge University Press, New York, 2006) p. 827.

Acknowledgements

I would like to express my deepest gratitude to my supervisor, Professor Toshiaki Suhara for his warm encouragement, continuous support, thoughtful guidance and constant inspiration. I am very much impressed by his great personality and supportive character. He spent many patient hours to teach me the fundamentals and advanced theory of semiconductor lasers. Besides introducing me the area of integrated semiconductor lasers, he also taught me the way to unravel complex physical pictures by using some intuitive ideas. Working under his supervision throughout the entire period of my study (masters and PhD) at Osaka University has a great impact on my life and future career.

I would also like to express my gratitude to Dr. Masahiro Uemukai, Assistant Professor of Osaka University for his constructive comments and important support throughout this work. He taught me how to use the advanced micro-fabrication facilities for the fabrication of semiconductor lasers, how to use different measurement instrument for characterization of the semiconductor lasers. Much of this work would not have been possible without his guidance.

I would like to extend my gratitude to the members of my dissertation committee, Professor Masahiko Kondow, Professor Heiji Watanabe and Professor Nobuya Mori for their valuable advices, continuous encouragements, careful reading and corrections that have improved the quality of the thesis.

I would also like to extend my gratitude to all of the distinguished Professors of Quantum Engineering Design Course (QEDC), Osaka University for accepting me as a student of this program.

I am very grateful to Ms. Yuka Yoshizaki and Ms. Keiko Sugita, secretaries of the Suhara Laboratory and Ms. Sayako Sakai, secretary of the Kasai Laboratory for their kind help and friendly assistant to prepare the important official documents many times during my study at Osaka university. I am thankful to all of my laboratory members for their continuous support and fruitful discussions regarding my research and daily life in Japan.

I acknowledge the Ministry of Education, Culture, Sports, Science and Technology (MEXT) in Japan for the financial support.

The last, but not the least, I am grateful to my parents for their love, support and constant blessing. Finally, I would like to extend my love and gratitude to my wife, Protiva Rani Saha for her patience, encouragement and moral support.